Design of Biaxial Accelerometers for Rigid-Body Pose-and-Twist Estimation

Ting Zou

Department of Mechanical Engineering
McGill University
Montréal, Canada

August 2013

A thesis submitted to McGill University
in partial fulfillment of the requirements for the degree of
Doctor of Philosophy

2013/08/15

Abstract

Pose and twist estimation is a ubiquitous problem in science and engineering: from astro- and aeronautics to biomechanics; from navigation systems to the latest video games. Current technology relies mainly upon accelerometer strapdowns, which call for precise estimation algorithms. Along these lines, the main objective of this dissertation is the development of innovative accelerometer strapdowns suitable for estimating rigid-body pose and twist accurately and reliably. The design philosophy is based on two interdependent concepts: an original concept of biaxial accelerometers, introduced in a previous dissertation and termed Simplicial Biaxial Accelerometers (SBA), and isotropic accelerometer strapdowns. The goal of the former is to sense accelerations along arbitrary directions in a plane. An improved SBA design is proposed and realized by means of MEMS (Microelectromechanical System) fabrication technology. By means of finite element analysis (FEA), the accelerometer sensitivity was found to be highly acceptable. The analysis results show that the SBA is isotropically sensitive to accelerations along arbitrary directions in the plane, while the cross-axis sensitivity is reduced, as desired. Isotropy mainly concerns a novel accelerometer strapdown made of the proposed SBAs. By virtue of its inherent geometric isotropy, the tetrahedral SBA strapdown is selected, but other isotropic polyhedra, such as the other four Platonic solids and Buckyballs, can be equally used. Performance and accuracy of the strapdown in estimating the pose and the twist of a rigid-body moving in space are illustrated with representative simulation examples. Moreover, the isotropic nature of the strapdown enables the decoupling of the point tangential acceleration from its centripetal counterpart in the acceleration field. Consequently, "coupling"—a major hurdle in pose and twist estimation—is avoided, thereby streamlining the estimation process.

Résumé

L'estimation de la pose et du torseur cinématique des corps rigides est un problème qui se retrouve partout en science et en ingénierie, aussi bien en aérospatiale, aéronautique ou biomécanique que dans les systèmes de navigation ou les jeux vidéos. La technologie acutelle repose principalement sur les assemblages d'accéléromètres qui exigent des algorithmes d'estimation précis. Le principal objectif de cette thèse est donc de développer des accéléromètres innovateures capables d'estimer, avec exactitude et fiabilité, la situation et le torseur cinématique en question. La conception de ces accéléromètres s'appuie sur deux idées originales interdépendantes: la biaxialité des accéléromètres, présentés antérieurement dans une thèse et appelés accéléromètres simpliciaux biaxiaux (ASB), et l'isotropie de leurs assemblages. L'objectif des ABS est d'estimer l'accélération dans des directions arbitraires sur un plan donné. La conception des ASB a été améliorée par l'auteure, et la technologie des SMEM (systèmes micro électromécaniques) a été utilisée pour leur fabrication. L'analyse numérique par éléments finis qui a servi à quantifier la sensibilité a été qualifiée de hautement acceptable. Les résultats montrent une sensiblité isotropique aux accélérations dans des directions arbitraires sur leur plan et une réduction de la sensibilité transversale, comme souhaité. L'isotropie porte principalement sur un nouvel assemblage d'accéléromètres fabriqué à partir des ASB. Les assemblages d'ASB en tétrahèdre ont été choisis en vertu de leur isotropie, mais il est aussi possible d'utiliser d'autres polyèdres isotropiques comme les quatre autres solides de Platon ou les Buckyballs. Des simulations illustrent la performance et la précision des assemblages dans l'estimation de la situation et du torseur cinḿatique d'un corps rigide en mouvement dans l'espace. En outre, l'isotropie de l'assemblage permet de découpler l'accélération tangentielle ponctuelle de son homologue centripète dans le champ d'accélération. Cela permet d'éliminer le problème du "couplage", et donc de simplifier ladite estimation.

Acknowledgements

I would like to express my most sincerely gratitude to my supervisor, Prof. Jorge Angeles, for introducing me to such an exciting realm of research. His invaluable support, generous effort, patience and outstanding ingenious scientific thoughts helped and encouraged me throughout my Ph.D. study. I would also like to thank Prof. Paul J. Zsombor-Murray. Without his excellent research advice, I would have confronted more obstacles during my study. Furthermore, I am grateful to Profs. Jozsef Kövecses, Srikar Vengallatore and Meyer Nahon, for serving on my Ph.D. Committee and for their helpful comments. Special thanks go to Prof. Vengallatore, whose professional expertise helped me significantly in the MEMS realization of biaxial accelerometers. My sincere gratitude goes to Prof. James R. Forbes, for his professional advice in the final stages of this project. Let me express my thanks to Dr. Matthieu Nannini, Mr. Jun Li and Mr. Donald Berry, of the McGill Nanotools MicroFab Laboratory, for their patience, advice and support on the microfabrication of the Simplicial Biaxial Accelerometer. My gratitude also goes to the *Natural Sciences and Engineering Research Council* and the *Fonds de recherche du Québec–Nature et technologies* for their financial support of my research. I am indebted to my colleague, Dr. Xiaoqing Ma, of the *Robotic Mechanical Systems Laboratory* (RMSL), whose kindness and team spirit bring me excellent memories of working here. Moreover, I would like to express my warm feelings to Mr. Jing Wu, who is deserved to be mentioned for supplying tremendous energy and encouragement to my studies. In addition, my special thoughts go to Ms. Wang Pei and Mr. Wu Yirui. Last but not least, let me thank my parents, Zou Kecheng and Liu Lanyuan, who are at the root of every effort that went in this work.

List of Abbreviations

- Aero- and astronautics (AA)
- ANSYS Parametric Design Language (APDL)
- Computer aided design (CAD)
- Cross-product matrix (CPM)
- Displacement-voltage matrix (DVM)
- Finite element analysis (FEA)
- Finite element method (FEM)
- Gyroscope-free strapdown (GF strapdown)
- Inertial measurement unit (IMU)
- Initial-value problem (IVP)
- Load-voltage matrix (LVM)
- Mean absolute percentage error (MAPE)
- Mircoelectromechanical systems (MEMS)
- Perpendicularity property (PP)
- Pesudo-rigid-body (PRB)
- Small-amplitude displacement (SAD)
- Signal-to-noise ratio (SNR)
- Simplicial uniaxial accelerometer (SUA)
- Simplicial biaxial accelerometer (SBA)
- Simplicial triaxial accelerometer (STA)

Contents

List of Figures

List of Tables

Chapter 1

Introduction

1.1 Rigid-body Pose and Twist Estimation

Rigid-body pose and twist estimation is a ubiquitous problem in engineering. Pose encompasses the position of a landmark point of a rigid-body and the body attitude, usually given by a rotation matrix that relates the current attitude with a reference one, twist encompassing the velocity of the same point and the body angular velocity. In principle, twist can be estimated from information on the acceleration of the landmark point and the body angular acceleration, upon integration of the acceleration information. Pose, in turn, can be estimated upon integration of the twist [1].

The problem arises in aero- and astronautics (AA), as well as in rehabilitation, robot assisted surgery, and in virtual environments, to name just a sample of application domains. However, current methods estimating the angular acceleration and angular velocity are not always accurate due to the inherent numerical errors which, in turn, hinder their development and application. Hence, there is a pressing need for more accurate methods for rigid-body pose and twist estimation.

1.2 Accelerometer Working Principle

Rigid-body pose and twist estimation is mainly based on the working principle of accelerometers—the mass-spring-dashpot system. A typical illustration of the system is shown in Fig. 1.1, in which the mass—often referred to as the *proof-mass*—can translate along one direction, termed the *sensitive axis*, with the help of a viscoelastic suspension.

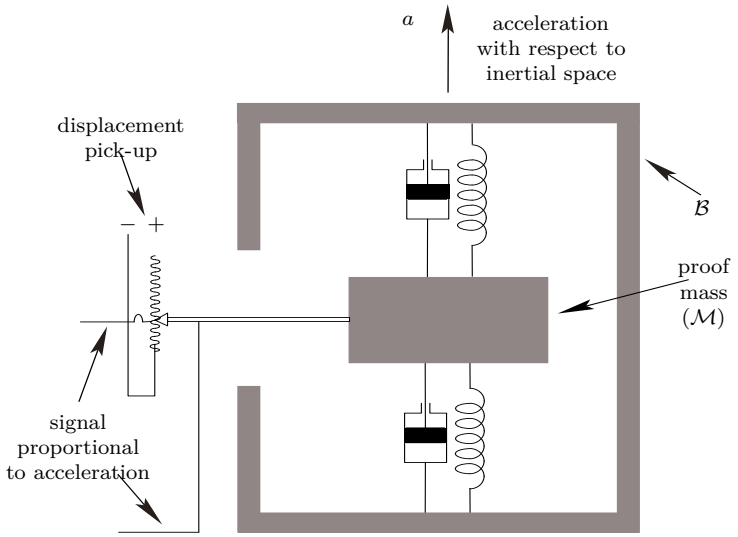

Fig. 1.1 Working principle of an accelerometer

Under working conditions, the accelerometer is rigidly mounted on a moving body $\mathcal{B}$ whose acceleration is to be measured; the resulting displacement of the proof-mass can yield a signal that obeys a linear algebraic relation with the acceleration.

1.3 Accelerometer Strapdown

An accelerometer strapdown is employed to yield information of the complete acceleration field of a rigid-body moving in space, i.e., its translational acceleration, angular acceleration and angular velocity, as only one single accelerometer, uni- or multiaxial, is not sufficient. The accelerometer strapdown is an array of accelerometers on the surface of a rigid-body [2]. The Platonic solids, with their intrinsic geometric symmetries, provide an ideal conceptual design for accelerometer strapdowns [3, 4].

1.4 Project Description and Objectives

This dissertation aims to develop a strapdown of multi-axial accelerometers with piezoresistive sensing technology. By attaching accelerometers to a rigid-body so as to form a feasible accelerometer strapdown [5], the rigid-body acceleration field is determined. Furthermore, estimation of rigid-body twist-rate, twist and pose will be given due attention.

The objectives of the thesis follow:

- To develop a methodology for the structural design of robust biaxial accelerometers, integrating robust sensing hardware with robust software.
- To validate the methodology with the fabrication of the accelerometers by means of MEMS technology, to be arrayed in a strapdown thereof.
- To derive robust and innovative pose-and-twist estimation algorithms from point-acceleration measurements.
- To validate the strapdown in estimating acceleration through numerical investigation.

1.5 Contributions

To the knowledge of the author, the main contributions proposed in this dissertation, as listed below, are original:

- An improved SBA design, with notched ΠΠ legs, that can yield high frequency ratios, over a previous design; meanwhile, the out-of-plane stiffness is significantly high compared with its in-plane counterparts.
- Optimum design of Lamé-notched flexure hinges in the ΠΠ leg, to minimize stress concentrations.
- The means of converting the proof-mass displacement into a strain signal.
- A piezoresistive sensing system leading to an electronic measurement circuit embedded in the SBA mechanical structure, to provide acceleration signals.
- Microfabrication of the SBA structure as well as the complete measurement circuit by means of MEMS technique, which brought about challenges that called for an additional research effort.
- The innovative design of an isotropic accelerometer strapdown, composed of the proposed SBAs, to be attached onto the rigid-body under measurement for estimation of the acceleration field.

- A robust estimation algorithm associated with the isotropic SBA strapdown, which is capable of decoupling the tangential component of point acceleration from its centripetal counterpart, thus leading to an innovative estimation algorithm.
- The isotropic strapdown that obviates the updating *second moment matrix* **J** that converts a set of biaxial point acceleration into rigid body acceleration.
- An algorithm based on the extended Kalman filter, with the introduction of system noise, to increase accuracy of the angular velocity estimation.
- A provisional patent application, on the proposed isotropic SBA strapdowns and associated algorithms for rigid-body pose and twist estimation [6].

1.6 Thesis Organization

An outline of the dissertation follows:

Chapter 2 summarizes the literature review on topics of compliant mechanisms, macro- and micro-fabrication techniques of compliant mechanisms, stiffness analysis and state of the art of accelerometer strapdowns.

Chapter 3 focuses on the study of compliant mechanisms and their application in accelerometers. Four types of flexure hinges are analyzed in terms of FEA under loading; the one with the minimum stress concentration is chosen for the accelerometer design. Based on compliant mechanisms, the idea of SBA and a novel SBA design are developed. The design objective is an instrument that exhibits isotropic low translational stiffness in one plane and high stiffness in the other four directions of the rigid-body motion space. In order to investigate the sensitivity to accelerations, different loading cases are applied onto the SBA, and the corresponding responses are generated. Embedded in the SBA structure, the electronic measurement circuit capable of generating an electronic signal to provide acceleration information is built. The performance and accuracy of the measurement circuit in estimating acceleration is verified by means of structural analysis in ANSYS.

In Chapter 4, a novel approach to the stiffness analysis in the context of parallel kinematics mechanisms is applied to the SBA. A survey of the existing approaches is provided. A recent approach for the structural design and analysis considering serial and parallel chains of compliant mechanisms is extended to the SBA stiffness analysis. The Lagrangian

formulation of the underlying mathematical model is also included. Both approaches are validated by means of a stiffness analysis of the system FE model in ANSYS. The second part of this chapter is concerned with the decoupling of the stiffness matrix, thereby allowing for the analysis of the translational and rotational stiffnesses independently.

Chapter 5 is devoted to the microfabrication of the SBA model through MEMS technology, which is conducted in the MIAM[1] Nanotool Microfab Laboratory. The microfabrication process is conducted on the $4''$ single crystal silicon wafer on five masks, using the CAD file for the refined MEMS masks. Three half-Wheatstone bridges are embedded in the MEMS prototype to form a measurement circuit, which is designed to be capable of yielding the acceleration information by means of the output voltage signals. This chapter serves to investigate the MEMS manufacturability of the SBA and pave the way for the testing of SBA strapdowns in future work.

In Chapter 6, the design of isotropic SBA strapdowns is proposed. Motivation is provided for constructing a strapdown whose estimation algorithm is more precise and simpler than existing alternatives. Insight is provided on the motivation behind isotropic SBA strapdowns. Performance and accuracy of the estimation algorithm are verified by two representative examples: a rotating rigid disk and a free-rotating rigid brick. In order to showcase the accuracy of the isotropic SBA strapdown, a non-isotropic SBA strapdown is also employed for the estimation of the acceleration field. Simulation results are illustrated and compared for both types of strapdowns. With the purpose of reducing measurement errors and improving precision, different integration methods are employed to obtain the angular velocity.

Finally, Chapter 7 includes conclusions and recommendations for future work.

[1]McGill Institute for Advanced Materials.

Chapter 2

Literature Review

2.1 Multi-axial Accelerometers

In the early stages of accelerometer technology, these instruments were mainly used for single-axis acceleration measurements in various domains: airplane catapults; aircraft shock absorbers; and vibration diagnosis for turbines [7]. In the 1960s and 1970s, with the advent of piezoelectricity, the field effect transistor (FET), and the charge amplifier, accelerometer development entered the next stage [8, 9]. These technologies distinguish themselves by their robustness in expanding the frequency bandwidth of sensors, which would directly lead to the introduction of accelerometers in shock-detection applications [10].

The advent of MEMS in the 1980s can be regarded as a watershed in accelerometer development. Thanks to MEMS technology, the sensing subsystem and its associated circuitry could be embedded in accelerometers, thus expanding the applications significantly. Since then, accelerometers have become more attractive in the fields of automotive crash detection, unmanned vehicles, automotive airbag systems, camera stabilization, etc [11]. In recent years, the popularity of GPS-aided navigation systems and video-game controllers set a new paradigm proving the successful applications of accelerometers in human-machine interactions. In summary, accelerometers find extensive applications in the automotive and industrial realms, covering several aspects, as listed below [12]:

- *Single-axis acceleration measurement*: mainly adopted in inertial navigation, airbag crash sensing, gait analysis, etc. Accelerometers can be used as components in GPS-aided navigation systems, which can provide continuous data between GPS updates

and during periods when the GPS signal is unavailable due to interference.

- *Vibration measurement*: single-axis accelerometers are adopted in seismic activity and shock monitoring, as well as vibration monitoring in aircraft turbines and underground pipes [7].

- *Inclinometers*: accelerometers for tilt measurement, which can also be integrated into a multitude of products, such as game controllers, virtual reality input devices, 3D computer mice, cameras, and personal navigation systems [13].

Of particular interest to this thesis is a class of accelerometers dubbed *Simplicial*. For this reason, its development is recalled below.

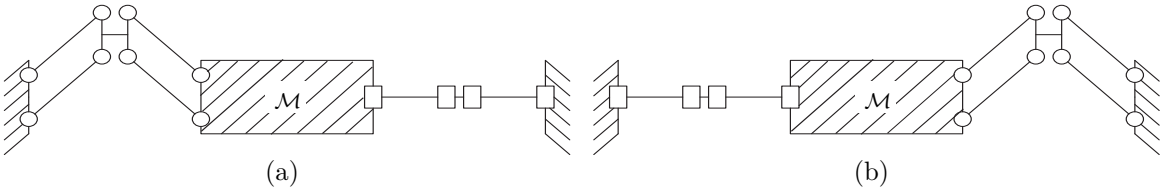

Fig. 2.1 Layout of 1D simplicial accelerometer: (a) front view; (b) top view

Based upon the concepts of *Parallel-Kinematics Machines*, novel architectures for multiaxial accelerometers were proposed by Cardou and Angeles [14][1], in which the proof-mass was suspended by $n+1$ legs ($n = 1, 2, 3$), where n is the number of acceleration components measurable by the accelerometer. Having one extra leg provides redundancy in the measurement, thereby offering robustness against measurement error. Not only this; the extra leg also provides an enhanced stiffness in the non-sensitive directions. Compared to serial architectures, parallel architectures offer superior properties in increasing the off-axis stiffness of the structure [16].

The SUA, shown in Fig. 2.1, is intended to measure point-acceleration along one direction, which is realized by employing two opposing $\Pi\Pi\Pi$ legs lying in orthogonal planes to constrain the proof-mass ($\mathcal{M}$) to translate in a direction parallel to the line of intersection of the two planes. The Π joint is a parallelogram linkage, as described in [17]. By means of

[1]The term *simplicial* is borrowed from mathematical programming, whereby a simplex is defined as a polyhedron in a n-dimensional space with a minimum number of vertices, namely, $n+1$—a polyhedron with a larger number of vertices is termed a complex. Hence, in n-dimensional space, for $n = 1, 2, 3$, the simplex is a line segment, a triangle and a tetrahedron, respectively [15].

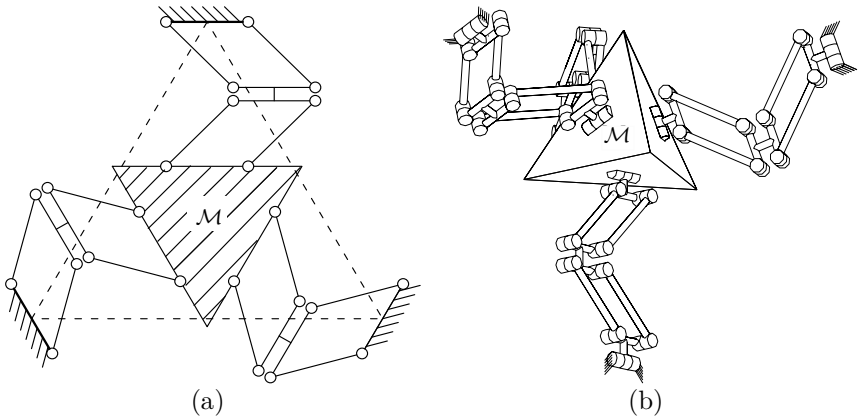

Fig. 2.2 Layout of 2D and 3D simplicial accelerometers: (a) SBA; (b) STA

a group-theoretic approach, it can be found that a ΠΠ linkage is a $\mathcal{T}_2$-generator, $\mathcal{T}_2$ being the planar-translation subgroup of $\mathcal{SE}(3)$, the group of rigid-body displacements, characterized by translations along two distinct directions. The SUA is designed to allow for only motion along the line of intersection of the two planes of the Π joints, which is named the *sensitive axis*, while exhibiting high stiffness in other directions.

The SBA, as illustrated in Fig. 2.2(a), is a planar parallel mechanism realized by laying out the three ΠΠ legs in a common plane at 120° from one another [5]. The SBA allows arbitrary translations parallel to the said plane, while providing a high stiffness along the direction perpendicular to the plane. One significant common feature of the simplicial class of accelerometer, in principle, lies in the equal dimensions of the triangle and tetrahedron, for the SBA and the STA, respectively, playing the note of the proof-mass. This feature will lead to equal sensitivity along the two or, correspondingly, three directions of interest, thus making the architecture *isotropic*.

Finally, the parallel mechanism designed to provide pure translations of its moving platform in space is recalled, the STA. This architecture is realized by suspending a rigid regular tetrahedral proof-mass via four RΠΠΠR legs, where R stands for revolute, as shown in Fig. 2.2(b). Each RΠΠΠR leg contains two revolute joints, with one of its ends attached rigidly to the tetrahedron and another end to the body under probing.

2.2 Compliant Mechanisms

2.2.1 Definition

One significant realization of accelerometer design is based on compliant mechanisms, which comprise at least one region that is highly deformable (flexible or compliant), as compared to the other regions of their monolithic structure [18]. In these structures, flexure hinges are commonly employed to produce a desired motion, rather than conventional mechanisms made up of rigid links coupled by lower and higher kinematic pairs [19]. Flexure-based compliant mechanisms are employed in a wide range of applications, especially in microscale devices, such as micro-positioning systems, microsensors, tilt mirrors, and microfluidic devices.

2.2.2 Characteristics

Compliant mechanisms have been studied extensively in the literature [20, 21, 22, 23]. Unlike their conventional articulated counterparts, which employ lower pairs such as pins and sliders, compliant mechanisms are jointless and have many desirable features: no assembly needed, no backlash, compactness, low cost and wear-resistance. The jointless feature brings some challenges as well, for example, a limited range of motion and undetermined axis of rotation, due to the complex deformation of flexure hinges [24]. The latter are designed to be compliant only about one axis, and stiff about all other directions of motion [25]. Within limited ranges, flexure hinges are often employed to provide ultra-precise motions. The advantages of flexure hinges are summarized below:

- Displacements are smooth and continuous.
- Manufacture is simple and inexpensive.
- No assembly and no maintenance are needed.
- No friction loses.
- For small distortions, a linear relationship between applied force and displacement is ensured and stays unchanged within manufacturing tolerance.

Flexure hinges also entail disadvantages, namely [26],

- For most materials, significantly high stress may cause hysteresis in the stress-strain characteristics.
- Limited range of rotations.
- Sensitive to temperature variations, that is to say, their dimensions may change due to thermal expansion.

Moreover, in practice, the complex deformation of the flexure hinge may produce undesired parasitic motion along the other axes [27]. Hence, a study on how to minimize the parasitic motions caused by flexure hinges is mandatory in accelerometer design. Due to the inherent nature of providing redundancy, the simplicial architectures become optimal realizations of accelerometers to reduce parasitic motions.

2.2.3 Material and Fabrication Techniques

Based on the design and analysis work, compliant mechanisms are required to be manufabricable. Depending on the scale of mechanisms—macro or micro—material and fabrication techniques vary widely. Macroscale compliant mechanisms are commonly fabricated on metallic materials, by means of diverse fabrication techniques: from the classical drilling and milling, to more complex ones, e.g., electron beam machining, wire electrodischarge machining (EDM), etc [18]. Among all existing macroscale fabrication techniques, rapid prototyping is promising. Rapid prototyping technology has experienced intensive development with the inception of rapid, high fidelity and well customized fabrication devices, such as 3D printers. This technology also brings possibility and convenience for rapid fabrication of compliant mechanisms, using plastic materials [28]. Micro compliant mechanisms, on the other hand, are commonly fabricated on a flat silicon wafer, by means of MEMS fabrication techniques, which will be introduced in Sec. 2.3.2.

2.3 MEMS Fabrication

2.3.1 MEMS Technology

MEMS technology broke new ground in the 1980s, as it set a new trend in mechanical system design: MEMS can be produced at the nanometric scale; their responses being

analyzed by means of the embedded microelectronic system [29, 30]. Thanks to microfabrication technology, MEMS can carry bores, cantilevers, cavities, membranes, etc., i.e., virtually all the features of conventional mechanical systems.

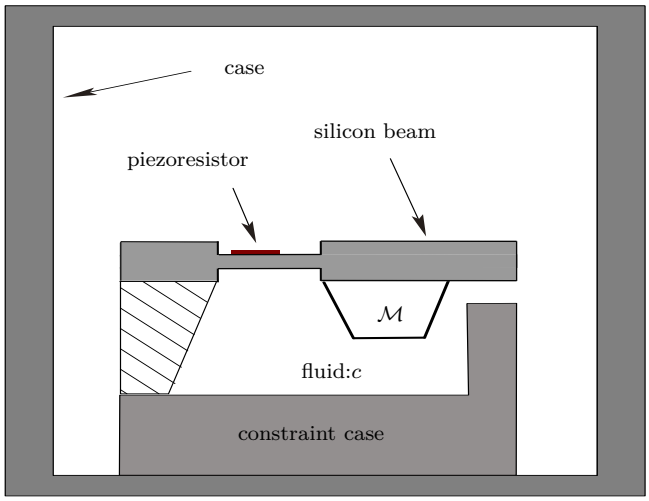

Fig. 2.3 Schematic configuration of a microaccelerometer

Figure 2.3 illustrates a typical example of a microaccelerometer system, in which $\mathcal{M}$ is the proof-mass. In microaccelerometers, the viscoelastic suspension is commonly realized by means of compliant hinges; the entrapped air or fluid adds to the damping provided by the material.

2.3.2 MEMS Fabrication Process

By means of photolithographic techniques, the patterns on the photomasks are transferred to the silicon surface. Generally, several other materials, that would supplement the functional tasks of the microsystem, are either grown or deposited on the silicon substrate. These materials include silicon dioxide (serving as sacrifice layer), silicon nitride (insulating layer), and metal films, such as aluminum, copper, gold, titanium or platinum (circuit connections). After deposition of the aforementioned thin films, selective etches can then be implemented to form the desired flexure mechanism [18, 25].

In this dissertation, our focus is the MEMS design and realization of one class of multi-axial accelerometers: Simplicial Biaxial Accelerometers (SBA). The most significant feature of multi-axial accelerometers is that they are capable of estimating multi-axial acceleration components of the rigid-body under probing. Because of its planar nature, the SBA

distinguishes itself from the other two classes of multi-axial accelerometers discussed in Section 1.3: the SUA and the STA. Their planar nature allows the microfabrication of the SBA, with their sensitive direction in their plane. This relatively simple fabrication process also eases the commercial applications of biaxial accelerometers; some products of MEMS biaxial accelerometers are available on the market [31].

In this dissertation, we are interested in the MEMS fabrication of the SBA with the objectives listed below:

- Low translational stiffness in the plane and high out-of-plane translational stiffness.
- Isotropic stiffness in the plane, i.e., the same stiffness in arbitrary directions of the SBA plane.
- Placement of the measurement circuits on either its top surface or its side walls, to construct a complete sensing system under piezoresistive principles.

2.3.3 MEMS Sensing

Table 2.1 Comparison among characteristics of sensing technologies

Specifications	Piezoelectric	Piezoresistive	Capacitive
Output impedance	High	Low	High
DC response	No DC response	Can measure down to DC, *e.g.* throughout long-duration events such as those associated with automobile braking	Can measure down to DC
Power consumption	Self-generating	Require an external power source	Require a standard voltage supply or battery
Temperature range	Large	Small	Very large
Sensitivity	Medium	Medium	High
Offset drift	Offset drift with impact	Offset drift with temperature	None
Complexity of circuitry	Medium	Low	High
Application ranges	Vibration measurements, *i.e.*, higher frequency	low-frequency applications	Wide bandwidth, low-frequency applications
Cross-axis sensitivity	Mainly determined by accelerometer mechanical design		
Advantages	Relatively small size, large bandwidth, high resonant frequency, good linearity	Simplicity of design, fabrication process and processing circuitry; compactness	High sensitivity, low power consumption, broad bandwidth, good linearity and stability
Disadvantages	No DC-response, high leakage	Temperature sensitivity	Relatively high cost, electromagnetic interference

Based upon the validated SBA model, we may turn to the sensing system in the SBA. According to Maluf [12], all accelerometers share a basic structure, consisting of a proof-mass mounted on a moving body by means of a viscoelastic suspension. However, they differ

in the sensing of the relative position of the proof-mass, as the mass translates relative to the accelerometer frame under the effect of a rigid-body acceleration. Measurement techniques for the estimation of proof-mass displacements have been reported, including measurement methods based on piezoelectricity, piezoresistivity, capacitance, metallo-resistivity, optical sensing mechanisms based on diffraction-gratings, and optical microencoders. Piezoelectricity is mainly used for vibration measurements, i.e., for high-frequency signals; capacitance and piezoresistivity are widely used physical principles for low-frequency applications. Metallo-resistivity, mainly adopted for high-frequency applications, is characterized by low temperature drift, low noise and high precision. Advantages of optical detection techniques compared to capacitive or piezoresistive technologies include high sensitivity. A summary of characteristics of different sensing technologies is given in Table 2.1. With reference to Allen [32], piezoresistivity is significant in MEMS sensors for the following reasons:

- Piezoresisitive effect in silicon is an order of magnitude higher than in metals.
- Optimal transmission of strain without creep is realized by means of the integration of the piezoresistive material and MEMS devices.
- Good matching of piezoresistors in the Wheatstone bridge circuit is possible by means of MEMS fabrication.

2.4 Stiffness Analysis of Compliant Mechanisms

2.4.1 Methodologies

The performance of compliant mechanisms is sensitive to their stiffness [33, 34, 35]. Generally speaking, two approaches can be adopted to determine the stiffness matrix: the energy approach based on the Lagrange formalism and FEA. However, the presence of hinges in compliant mechanisms can make the parametric calculation of kinetic and potential energies extremely difficult. Furthermore, following the Lagrangian approach, the direct relationship between stiffness and free-form components can be cumbersome to establish [34]. Therefore, FEA is more often employed in determining the stiffness matrix. However, FEA is often time-demanding, depends on the meshing technique, and is capable of analyzing the mechanism only after all specific dimensions are defined [36].

Another difficulty in connection with stiffness analysis lies in the complex assembly of the mechanism. In micro-compliant mechanisms, the assembly is always extremely complicated and can consist of both serial and parallel chains of flexure hinges and rigid links [37]. In this sense, research works are seldom found on the full modeling of micro-compliant mechanisms, the most widely employed modeling technique being based on simplified models. The interested reader may refer to [37, 38, 39] for a detailed review of current simplification methods. Among these, the effective pseudo-rigid-body (PRB) method is frequently used [23, 40]. Within this approach, all the flexure hinges are replaced by *single-degree-of-freedom* revolute joints along with a torsional spring, while modeling the remaining parts as rigid bodies. However, the PRB is only capable of exhibiting stiffness in the principal direction, while leaving the stiffness in other directions undetermined [41]. To overcome this shortcoming, the lumped-parameter model can be adopted to determine the stiffness of the mechanism [42]: the mechanism is assumed to move in both translation and rotation, the flexure hinges being replaced by multi-dof joints. By doing this, the stiffness of the flexure hinge along all six-dof directions can be obtained. Hence, the lumped-parameter model can be extended to analyze compliant mechanisms with ditto, in the presence of serial and parallel chains [34, 35].

2.4.2 Decoupling of the Cartesian Stiffness Matrix

The 6×6 Cartesian stiffness matrix of a class of multibody systems contains the 3×3 rotational, translational and coupled stiffness blocks of the system [43]. For compliant-mechanism design, the Cartesian stiffness matrix can be obtained in terms of FEA [44]. A means to predict the stiffness of the mounting of a rigid body on an elastic suspension relies on the entries of the stiffness matrix [45]. Another means rely on the eigenvalues and eigenvectors of the same matrix, which convey more information than the individual entries, as the former are frame-invariant [46]. However, spurious coupling of translational and rotational stiffness may occur, as first pointed out in [47]. Coupling prevents an independent analysis of the translational and rotational stiffnesses of the system. Moreover, the Cartesian stiffness matrix has entries with different physical units, thereby calling for a generalized eigenvalue analysis [48]. The decoupling of the Cartesian stiffness matrix was discussed by Selig [49] and Angeles [50]. In some typical applications, such as accelerometer design, the structure is desired to exhibit compliance along the sensitive axes and high

stiffness along the remaining axes of the rigid-body motion space. Due to this feature, *screw theory* is often employed to help investigate the motions of compliant mechanisms [49]. Contemporary works on screw theory are available in the literature [51, 52, 53, 54, 55, 56, 57].

2.5 Accelerometer Strapdowns

2.5.1 State of the Art of Inertial Measurement Units

A conventional strapdown consists of three accelerometers to measure point acceleration and three gyroscopes to measure the three components of angular velocity [58]. These sensor systems may be used to infer the complete rigid-body acceleration field, i.e., the twist—velocity and angular velocity—and its time-rate of change. Gyroscopes can provide direct measurements of angular velocity, which obviates the need of integration of the angular acceleration [59, 60, 61, 62, 63, 64]. However, gyroscopes exhibit some drawbacks, such as complicated fabrication, high cost and power consumption as well as high sensitivity to impact [65]. Moreover, a relatively low-cost gyroscope lacks the accuracy required for precise measurement. In view of the fabrication cost, a micromachined accelerometer with high precision is more attractive. Hence, the *gyroscope-free strapdown (GF strapdown)*, which was first proposed by Dinapoli [66], has become a novel trend in the field of navigation systems [67, 68, 69].

2.5.2 Strapdown Applications

The applications of the accelerometer strapdowns are found in many fields: automotive industry, aero- and astronautics, biomechanics and navigation systems, etc. [8, 70, 71]. For example, the advent of the da Vinci Surgery System is a textbook example of the application of the accelerometer strapdown in the development of robotic surgery, as illustrated in Fig. 2.4. In 2000, the da Vinci surgery system became the first robotic system approved by the FDA[2] for general laparoscopic surgery. The da Vinci surgical system employs joint kinematics to calculate the position and velocity of the tool tip internally. With accelerometer strapdowns mounted to the patient-side manipulators, an accurate surgical operation is ensured, even at the millimetric scale. The operating arms are made as thin

[2]U.S. Food and Drug Administration.

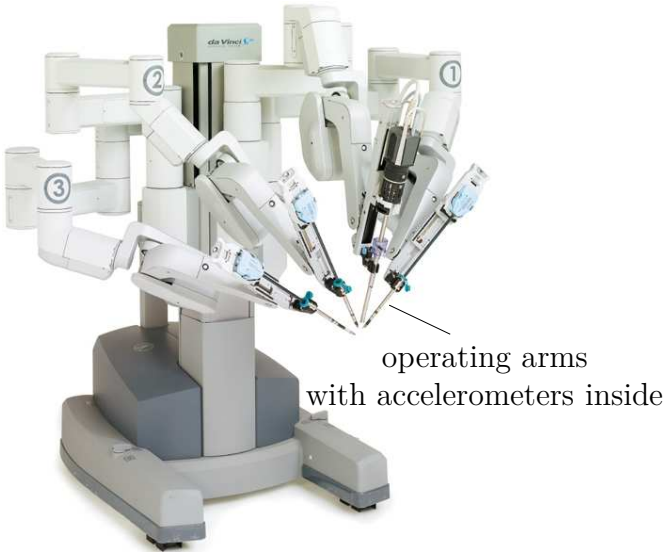

Fig. 2.4 Da Vinci Surgery System

as 10 mm in diameter, which is advantageous to reduce contact between surgical device and exposed tissue, thus moving a big step forward to reducing the risk of infection. The FDA approved the da Vinci Surgery System in both adult and pediatric procedures in areas such as: urological surgery, general laparoscopic surgery as well as thoracoscopically-assisted carditomy procedures, etc.

Fig. 2.5 Accelerometer strapdown in the Boeing 787 Dreamliner

In the astro- and aeronautical realm, accelerometer strapdowns became compulsory in aircraft design for the detection of rotation, acceleration and pose in space [7]. For exam-

ple, the new Boeing 787 Dreamliner, illustrated in Fig. 2.5, has a sophisticated system of accelerometer strapdowns at its nose. The accelerometer strapdowns are meant to play an important role in providing not only a safer flight—through their robustness in detecting the acceleration and monitoring turbine engine vibration—but also a much more comfortable flight experience. For instance, in the presence of strong turbulence, the airplane drops several meters, which gives the passengers the sense that the airplane is falling. For the purpose of counteracting the effects of turbulence, the Boeing 787 Dreamliner adds an accelerometer system to its nose. Therefore, if a sudden drop is detected by the accelerometers, they will simultaneously tell the wing flaps to adjust quickly. By doing so, a 3 m drop for an older aircraft is reduced to just 1 m for the Boeing 787, thus offering a much smoother flight experience to the passengers.

Accelerometer strapdowns are also widely employed in astronautics. The breathtaking rendez-vous of the space shuttle Discovery with the International Space Station is a paradigm of a successful application of accelerometer strapdowns. Each of Discovery's wings has stapdown systems of 66 accelerometers to detect impacts and gauge their strength and location. These systems bear a rich network of sensors to help engineers and astronauts gain a better control of the working conditions in the space shuttle.

2.5.3 Isotropic Accelerometer Strapdowns based upon the Platonic Solids

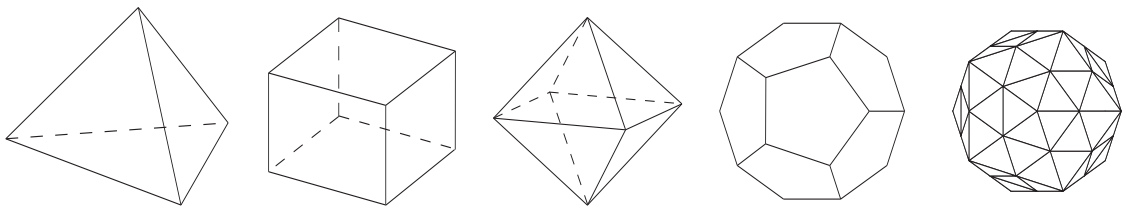

Fig. 2.6 Platonic solids: (a) tetrahedron; (b) cube; (c) octahedron; (d) dodecahedron; and (e) icosahedron

The Platonic solids are deemed attractive for the design of SBA strapdowns due to their geometric isotropy. These are a class of solids whose faces are all identical regular polygons. It was first proven by Theaetetus in 360 BCE that there exist precisely five Platonic solids:

the tetrahedron (four equilateral triangular faces), the cube (six square faces), the octahedron (eight equilateral triangular faces), the dodecahedron (twelve pentagonal faces) and the icosahedron (twenty equilateral triangular faces), which were further explicitly demonstrated in Book XIII of Eulid's *Elements*. Theaetetus' proof[3] on the precise number of Platonic solids can be found in [72]. Their aesthetic symmetries aside, the characteristics of the Platonic solids in view of their group symmetries have also been studied [73, 74]. These five Platonic solids are shown in Fig. 2.6, with a summary of their corresponding geometric features listed in Table 2.2[4].

Table 2.2 Properties of Platonic solids

Solid	Faces	Vertices	Edges	Dual polyhedron
tetrahedron	4	4	6	tetrahedron
cube	6	8	12	octahedron
octahedron	8	6	12	cube
dodecahedron	12	20	30	icosahedron
icosahedron	20	12	30	dodecahedron

It is noteworthy that tetrahedron- and cube layouts are more commonly employed than the other three Platonic solids, mainly due to their structural simplicity and concomitant lower cost. As a consequence, the accelerometer strapdowns based upon the first two Platonic solids are adopted in this thesis. Details of the isotropic SBA strapdowns in estimating rigid-body pose and twist are included in Chap. 6.

2.5.4 Pose-and-Twist Estimation Algorithms

The GF strapdown is intended to provide measurements of the acceleration field of a rigid-body moving in space, nine scalar quantities in total [66]. Theoretically, a minimum of six accelerometers are required in a GF strapdown to provide a full estimation of the acceleration field, since angular velocity can be integrated out of angular acceleration [75]. However, within this layout, the value of angular acceleration depends upon the a priori knowledge of angular velocity, which is derived from integration of the angular accelera-

[3] Theaetetus proved that there are precisely five regular convex polyhedra.

[4] According to the duality principle, each regular polyhedron has its dual polyhedron in which faces and vertices possess complementary locations. The *dual polyhedron* can be constructed by: (1) placing a point in the centre of each face of the original polyhedron; (2) connecting each new point with the new points of its neighboring faces; and (3) eliminating the original polyhedron [72].

tion in the former step. As a result, the estimation error grows quickly. To address this issue, a six-accelerometer cube-type GF strapdown was proposed, in which the angular acceleration is estimated independently [75, 76, 77, 78]. Besides, other types of strapdowns have been proposed, such as the six-accelerometer layout with a feedback compensation system [75, 77], and the nine-axis accelerometer strapdown [79, 78, 80]. However, current accelerometer strapdowns suffer from some shortcomings. For example, for most current strapdowns, accelerometers, usually uniaxial, are required to be located individually on the rigid-body under probing, with individual orientations [78, 81, 82]. Therefore, the user has to determine the attachment locations of all the accelerometers on the rigid-body as well as their orientations, to build the strapdown; this calls for the test of several different layouts of diverse accelerometer locations and orientations, to find at least one layout able to yield the acceleration field of the rigid-body under probing. For example, the patent in [83] concentrates on the application of accelerometer assembly mounting on a helmet for crash test, which needs a total number of sensing axes greater than or equal to twelve. In this design, the user has to figure out the way to locate at least twelve accelerometers as well as their orientations, for the purpose of realizing effective measurements. Not only this; the sign-ambiguity problem also arises, which comes from the quadratic nature of the angular velocity in the centripetal-acceleration component. Since the tangential- and centripetal-components of the acceleration field are not decoupled by current strapdowns, sign-ambiguity always hinders pose-and-twist estimation. One approach to address this predicament is to increase the number of accelerometers, in order to provide redundant measurements. The reader is referred to [84, 85] for details on the proposed solutions. However, an increase of the number of accelerometers not only increases the financial cost, but also is incapable, by itself, of directly decoupling the tangential and centripetal components of the acceleration field. The aforementioned shortcomings of current strapdowns, on the other hand, leave ample room for improvement, which is what this dissertation intends to do.

Chapter 3

Design of Simplicial Biaxial Accelerometers

3.1 Overview

The concept of Simplicial-Biaxial-Accelerometer was first proposed by Cardou [5]. Due to its planar nature, the SBA is amenable to microfabrication. Figure 3.1 illustrates the SBA design as proposed by Cardou [5] at the *Robotic Mechanical System Laboratory*, McGill University. The proof-mass at the centre moves by virtue of the motion of the rigid-body under probing. Three sets of Π-joints with a pair of constant cross-section flexible beams are built to connect the proof-mass to the frame of the SBA, which is rigidly attached to the object under probing. An electronic measurement system composed of electrodes embedded and fixed rigidly on the beam is intended to yield the acceleration information of the rigid-body based on the following principle: the electrodes undergo the same deformation as the flexible beams, caused by the motion of the proof-mass, thus leading to the capacitance variations between them. The capacitance variations are sensed by the electronic measurement system so that a corresponding output voltage is produced. With this approach, the output voltage is a result of the motion of the proof-mass. Afterwards, several estimation algorithms can be applied to obtain the acceleration of the proof-mass, the acceleration of the rigid-body to be measured being obtained accordingly.

We have conducted a static analysis in ANSYS on the SBA shown in Fig. 3.1, and found that this architecture readily comes across interference between the proof-mass and

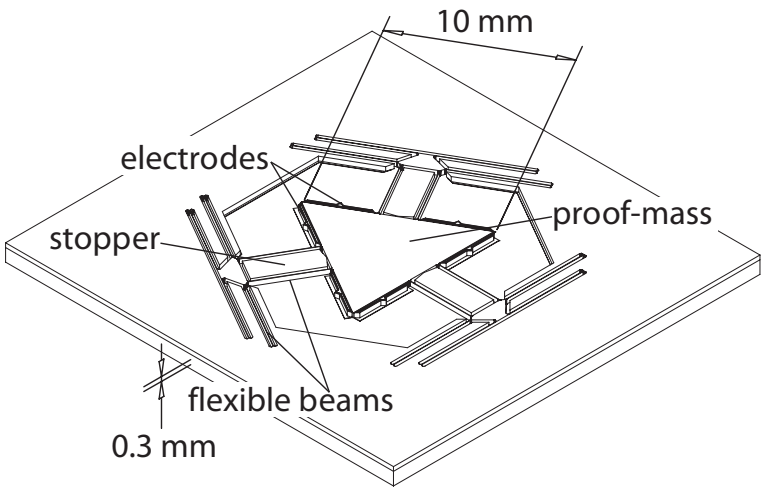

Fig. 3.1 SBA architecture proposed by P. Cardou

the fixed frame. The problem may be inevitable due to the inherent high compliance of the structure. The experimental tests of the MEMS model of the structure also illustrated that out-of-plane motions are likely to occur. To overcome this problem, a novel SBA design is proposed and dimensioned in Section 3.4. Its modal analysis is conducted in ANSYS, with static and harmonic loadings applied to the proof-mass in order to investigate the capability and sensitivity of the SBA in acceleration estimation under different loading conditions. After validation of the SBA design, a piezoresistive sensing system is built to yield acceleration information. A numerical experiment is conducted in ANSYS, for the purpose of validating the agreement of the sensor output with the forced response of the proof-mass, thus shedding light on the feasibility and precision of the sensing system of the SBA.

3.2 Conceptual Design

3.2.1 Compliant Mechanisms and Design of Flexure Hinges

Compliant mechanisms are widely used in the design of MEMS-based accelerometers. According to Howell [23], a compliant mechanism comprises at least one localized region that is highly deformable (compliant) when compared to the balance of the structure.

The general realization of flexure hinges depends on the cross-section profile; some of the common shapes are illustrated in Fig. 3.2. Based on flexure hinges, the realization of

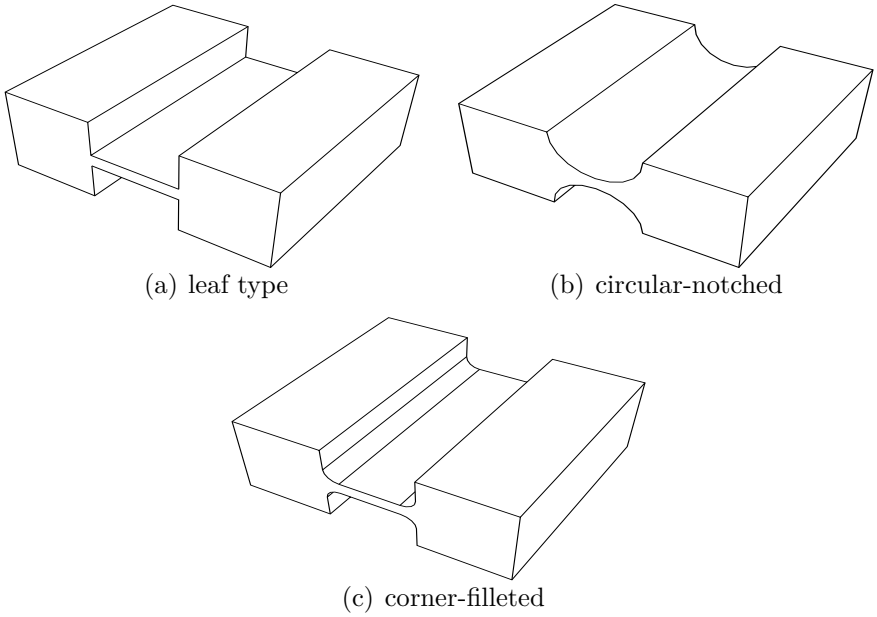

(a) leaf type (b) circular-notched

(c) corner-filleted

Fig. 3.2 General realization of flexure hinges

compliant Π-joints is shown in Fig. 3.3. One possibility is by means of one pair of long beams with constant cross-section; another by means of four notched hinges, as illustrated in Figs. 3.3 (a) and (b), respectively. Compared with its long-beam counterpart, the notched Π-joint has the desirable feature of high stiffness ratios between the sensitive direction and the other directions. However, this type of realization also exhibits the inherent demerit of a limited range of motion.

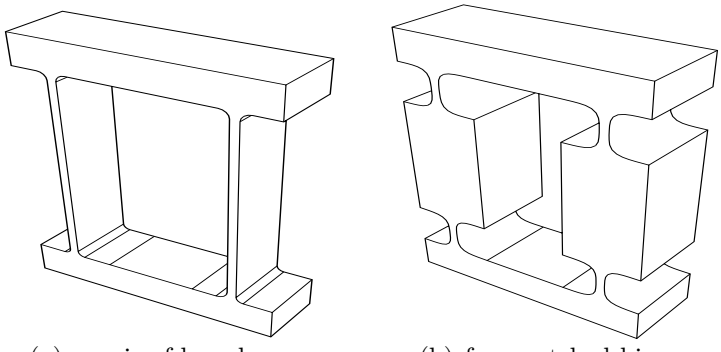

(a) a pair of long beams (b) four notched hinges

Fig. 3.3 Pictorials of two compliant realizations of the Π-joint

3.2.2 Lamé-notched Flexure Hinge

According to Lobontiu [86], current types of flexure hinges, including the leaf-type, circular-filleted and circular-notched hinges, are prone to high stress concentration. In order to address this deficiency, the Lamé-notched hinge was proposed [44, 47], which is defined as [87]

$$\left|\frac{x}{a}\right|^{\eta} + \left|\frac{y}{b}\right|^{\eta} = 1 \qquad \eta = 1, 2, ... \tag{3.1}$$

where a and b are one-half of the side lengths of the circumscribing rectangle.

3.2.3 Lamé Curves

Figure 3.4 illustrates Lamé curves. Even-order Lamé curves are analytic everywhere. For $\eta = 2$, the curve becomes an ellipse; for $\eta \to \infty$, the curve approaches a rectangle. An important shortcoming intrinsic to compliant mechanisms is that high stress concentration may lead to fatigue failure, while curvature discontinuities of the structure profile generate stress concentration. We recall the concept of G^2-continuity, which denotes position, tangent and curvature continuity over a given geometric curve [87]. G^2-continuity thus becomes a significant criterion in analyzing the level of stress concentration in a flexure hinge. Figure 3.5(a) illustrates the profile of the circular-filleted hinge, where R is the radius. From its curvature distribution $\kappa(s)$ in terms of s in Fig. 3.5(b), we observe that the profile leads to G^2-discontinuity at points A and B, because of the curvature discontinuities at the two blending points with a straight segment. On the other hand, the curvature of the 4th-order Lamé-notched hinge behaves continuously over the notch profile, as illustrated in Fig. 3.6(b). The notch shape thus provides G^2-continuity, thereby reducing the stress concentration. A key property of Lamé curves helps to explain this property: their curvature vanishes at the intersections with the coordinate axes when $\eta > 2$, hence, G^2-continuity can be satisfied when Lamé curves are employed as the fillets of a straight beam.

Hinges designed with the form of a Lamé curve offer G^2-continuity along the notch surface, as opposed to their circular counterparts. An illustration of a Lamé-notched hinge is shown in Fig. 3.7, in which one end of the flexure hinge is clamped, and a vertical load F is applied at the free end, along the y-direction. The flexibility parameter υ—read

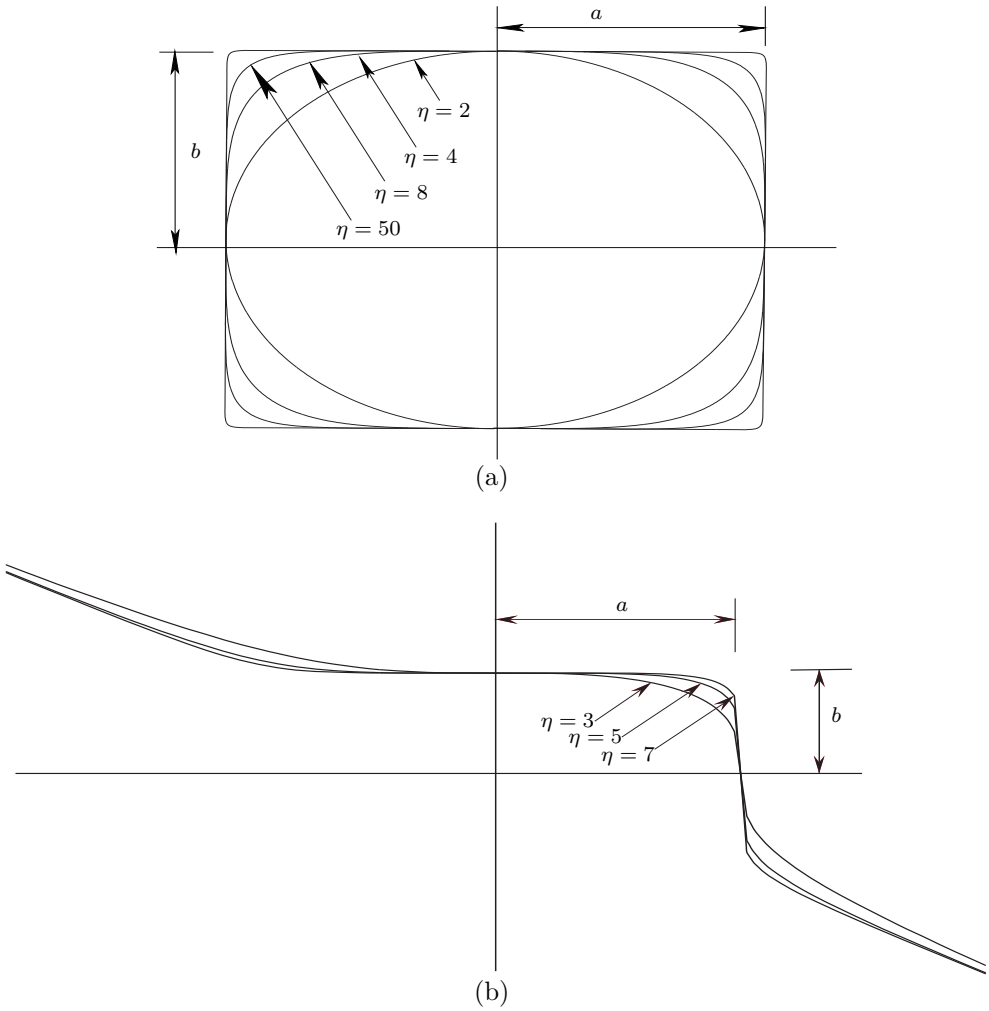

Fig. 3.4 Lamé curves with variable η: (a) Even-order; (b) Odd-order.

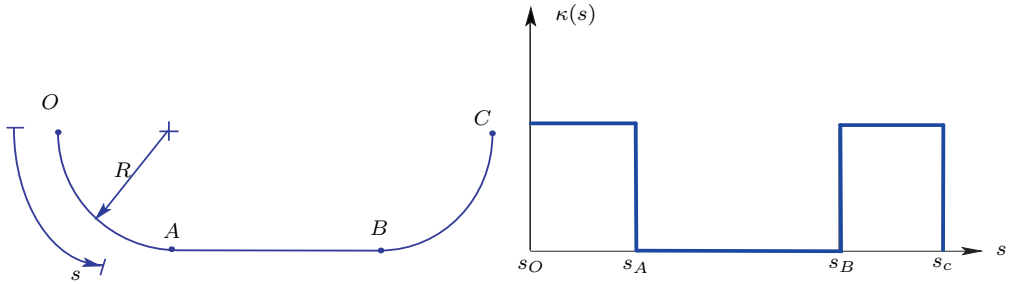

(a) hinge profile (b) curvature distribution

Fig. 3.5 Circular-fillted flexible hinges

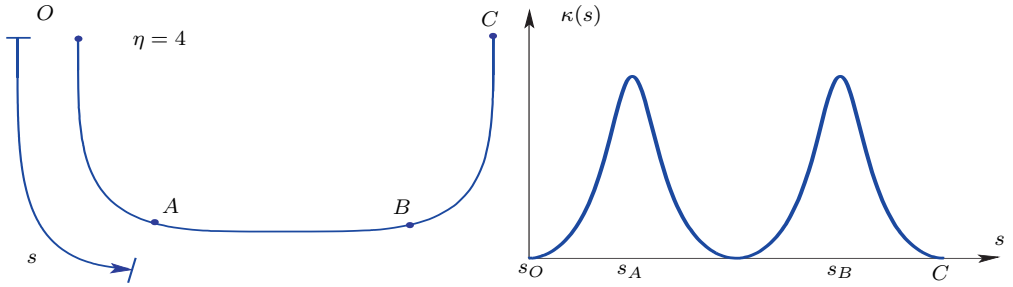

(a) 4th-order hinge profile (b) curvature distribution

Fig. 3.6 Lamé-notched hinges

"upsilon"—is given in terms of the nominal stress as:

$$\bar{\sigma}_{\text{nom}} = \frac{6M}{wt_m^2} = \frac{6Fl}{wt_m^2}, \quad \upsilon = \frac{u_{\max} E w t_m^2}{Fl^2} \tag{3.2}$$

where l, w and t_m are the length, the depth and the minimum thickness of the hinge, while $u_{\max}$ is the maximum deflection of the hinge along the y-direction in response to the applied load F.

3.2.4 FEA of Lamé-notched Hinge

The stress concentration factor is defined as the ratio of the maximum von Mises stress σ_{vM}, which occurs within the limit of the elastic range, to the *nominal stress* $\bar{\sigma}_{nom}$ [88], i.e., $K_t = \sigma_{vM}/\bar{\sigma}_{nom}$.

In order to illustrate the stress distribution under loading, four types of flexure hinges are investigated under FEA, as shown in Fig. 3.8. The structural optimization of the Lamé-notched hinge is developed using the ANSYS Parametric Design Language (APDL).

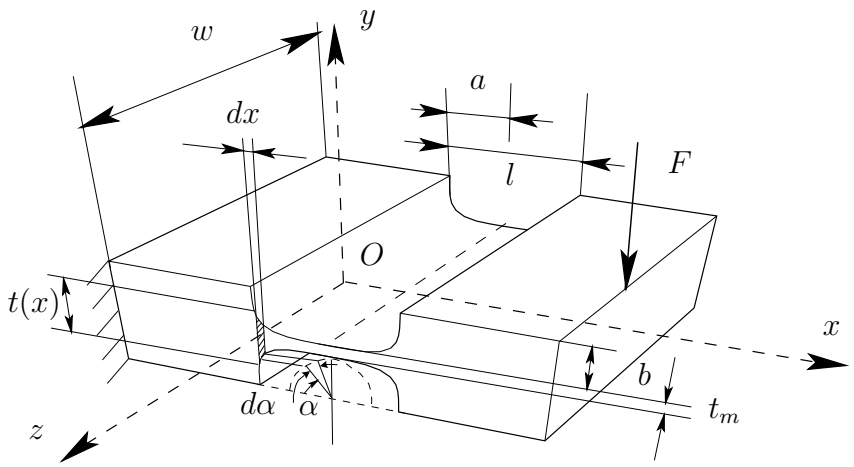

Fig. 3.7 Geometry of a Lamé-notched flexure hinge

The first-order optimization method is employed. At each iteration, the design variables are changed, with the new FE model generated accordingly. Also, a tolerance of 10^{-6} is imposed on the objective function. The optimum results are $a = 105\,\mu$m and $b = 70\,\mu$m. Stress concentration levels of four types of flexure hinges under the same boundary conditions are compared, while showcasing the advantages of the Lamé-notched hinge in reducing stress concentration. A comparison of the stress concentration factor K_t and the flexibility parameter υ is provided in Table 3.1. Some conclusions follow:

- The leaf-type hinge is the most bending-compliant, but induces the maximum stress concentration.
- The circular-notched hinge causes lower stress, but shows lower flexibility.
- The values of K_t and υ of the circular-filleted hinge lie between those of the leaf and circular-notched hinges[1]. This is reasonable because the leaf type and circular-notched hinges are two typical cases of circular-filleted hinges, the former with $r = 0$ (r is the fillet radius), the latter with $r = l/2$ (l is the hinge length).
- The Lamé-notched hinge bears the lowest stress concentration and shows a higher bending-compliance than the circular hinge.

[1]A set of FEA was conducted to investigate the effect of fillet radius on K_t and υ. The value of fillet radius is chosen 20 μm.

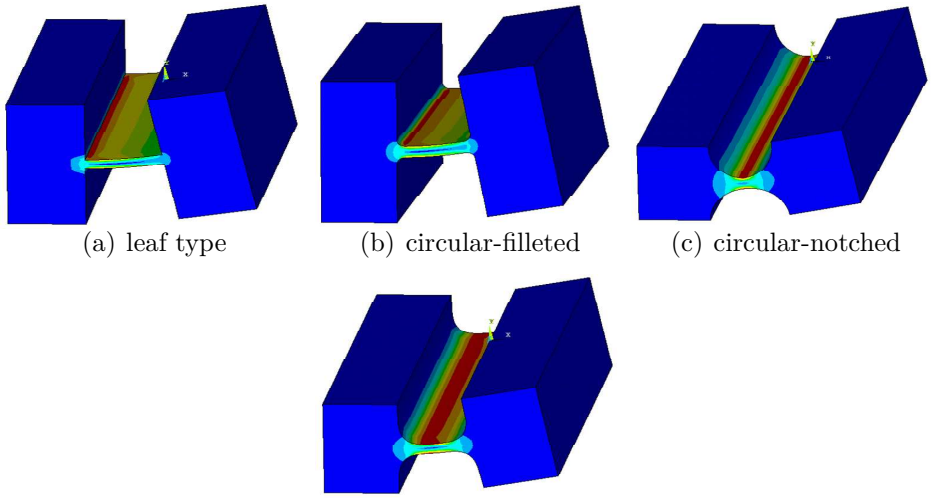

(a) leaf type (b) circular-filleted (c) circular-notched

(d) Lamé-notched

Fig. 3.8 FE results of von Mises stress distribution for flexure hinges

Table 3.1 Comparison results for K_t and υ of different flexure hinges

	Hinge Types			
	Leaf type	Circular-filleted	Circular-notched	Lamé-notched
K_t	2.0645	1.9119	1.3190	1.3077
υ	169.0436	152.4052	53.5299	93.3921

3.3 Stiffness Analysis of the Lamé-notched Flexure Hinge

As illustrated in Fig. 3.7, the 4th-order Lamé-notched hinge is fixed at one end, and subjected to three-dimensional loading at the free end. The 6 degree-of-freedom (dof) of the free end comprise three translations, u_x, u_y, u_z, and three rotations, θ_x, θ_y, θ_z, with respect to the reference coordinate frame $Oxyz$.

The 6×6 compliance matrix of the Lamé-notched hinge takes the form [18]:

$$\mathbf{C}_h = \begin{bmatrix} C_{\theta_x M_x} & 0 & 0 & 0 & 0 & 0 \\ 0 & C_{\theta_y M_y} & 0 & 0 & 0 & C_{\theta_y F_z} \\ 0 & 0 & C_{\theta_z M_z} & 0 & C_{\theta_z F_y} & 0 \\ 0 & 0 & 0 & C_{u_x F_x} & 0 & 0 \\ 0 & 0 & C_{u_y M_z} & 0 & C_{u_y F_y} & 0 \\ 0 & C_{u_z M_y} & 0 & 0 & 0 & C_{u_z F_z} \end{bmatrix} \tag{3.3}$$

where $C_{u_y M_z} = C_{\theta_z F_y}$ and $C_{u_z M_y} = C_{\theta_y F_z}$.

Castigliano's second theorem is adopted to determine the compliance entries appearing in eq. (3.3). This theorem is an effective approach to calculating the deformation of an elastic body under external loading and supporting conditions. Within this theorem, the local translational or rotational deformation can be regarded as the partial derivative of the total strain energy of the elastic body with respect to the external force or moment acting in the corresponding location or direction, as expressed below:

$$u = \frac{\partial U}{\partial F} \tag{3.4}$$

where U is the strain energy stored in the body, F is the applied force or moment, and u is the corresponding deformation.

With reference to Fig. 3.7, the thickness of the flexure hinge $t(x)$ is a function of x, namely,

$$t\left(x\right) = 2\left(b + \frac{t_m}{2}\right) - 2b\left[1 - \frac{(a-x)^4}{a^4}\right]^{\frac{1}{4}} \tag{3.5}$$

The strain energy due to the bending moment M_z is

$$U_{\mathrm{b},z} = \int_0^l \frac{M_z^2}{2EI_z} dx \tag{3.6}$$

where E is the Young modulus and I_z the area second moment about the x-axis, which is given by $I_z(x) = wt^3(x)/12$.

According to eq. (3.4), the bending angular displacement θ_z is obtained as

$$\theta_z = \frac{\partial U_{\mathrm{b},z}}{\partial M_z} = \frac{M_z}{E}\int_0^l \frac{1}{I_z} dx = \frac{12M_z}{Ew}\int_0^l \frac{1}{t(x)^3} dx \tag{3.7}$$

Substituting eq. (3.5) into eq. (3.7) leads to

$$\theta_z = \frac{12M_z}{Ew} g(x) \tag{3.8}$$

where

$$g(x) = \int_0^{2a} \frac{1}{[2b + t_m - 2b\left(1 - (a-x)^4/a^4\right)^{\frac{1}{4}}]^3} dx \tag{3.9}$$

For numerical convenience, x of eq. (3.8) is expressed below in polar coordinates. Let $x = a - a\cos\alpha$, $\alpha \in [0, \pi]$; therefore, $dx = a\sin\alpha d\alpha$, θ_z then becoming

$$\theta_z = \frac{12M_z a}{Ew}\int_0^\pi \frac{\sin\alpha}{[2b + t_m - 2b(1-\cos^4\alpha)^{\frac{1}{4}}]^3}d\alpha \tag{3.10}$$

Further, let $\xi = b/t_m$, so that $b = \xi t_m$. Substituting this relation into eq. (3.10) yields

$$\begin{aligned}\theta_z &= \frac{12M_z a}{Ewt_m^3}\int_0^\pi \frac{\sin\alpha}{[2\xi + 1 - 2\xi(1-\cos^4\alpha)^{\frac{1}{4}}]^3}d\alpha \\ &= \frac{12M_z a}{Ewt_m^3}f(\xi)\end{aligned} \tag{3.11}$$

Hence, the in-plane bending compliance $C_{\theta_z M_z}$ is given by:

$$C_{\theta_z M_z} = \frac{12a}{Ewt_m^3}\int_0^\pi \frac{\sin\alpha}{[2\xi + 1 - 2\xi(1-\cos^4\alpha)^{\frac{1}{4}}]^3}d\alpha = \frac{12a}{Ewt_m^3}f(\xi) \tag{3.12}$$

For a given $\xi = b/t_m$, the integral $f(\xi)$ is evaluated by means of Romberg's numerical quadrature [89].

Expressions of the other compliance entries in eq. (3.3) are obtained likewise:

$$\begin{aligned}
C_{u_x F_x} &= \frac{a}{Ewt_m}\int_0^\pi \frac{\sin\alpha}{2\xi + 1 - 2\xi(1-\cos^4\alpha)^{\frac{1}{4}}}d\alpha \\
C_{u_y F_y} &= \frac{12a^3}{Ewt_m^3}\int_0^\pi \frac{(1-\cos\alpha)^2\sin\alpha}{[2\xi + 1 - 2\xi(1-\cos^4\alpha)^{\frac{1}{4}}]^3}d\alpha \\
C_{u_z F_z} &= \frac{12a^3}{Ew^3 t_m}\int_0^\pi \frac{(1-\cos\alpha)^2\sin\alpha}{2\xi + 1 - 2\xi(1-\cos^4\alpha)^{\frac{1}{4}}}d\alpha \\
C_{\theta_y M_y} &= \frac{12}{w^2}C_{u_x F_x} \\
C_{u_y M_z} &= \frac{12a^2}{Ewt_m^3}\int_0^\pi \frac{(1-\cos\alpha)\sin\alpha}{[2\xi + 1 - 2\xi(1-\cos^4\alpha)^{\frac{1}{4}}]^3}d\alpha \\
C_{u_z M_y} &= \frac{12a^2}{Ew^3 t_m}\int_0^\pi \frac{(1-\cos\alpha)\sin\alpha}{2\xi + 1 - 2\xi(1-\cos^4\alpha)^{\frac{1}{4}}}d\alpha
\end{aligned} \tag{3.13}$$

Further, a torsion load M_x is applied at the opposite, free end, as illustrated in Fig. 3.9. An approximate expression for the torsional stiffness of the notched hinge can be obtained by dividing the hinge into infinitesimal vertical slabs. Hence, the corresponding torsional

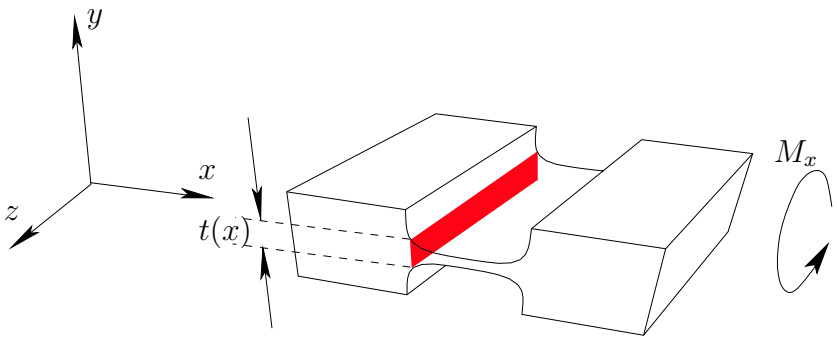

Fig. 3.9 CAD model of a Lamé-notched flexure hinge

angle θ_x due to pure torsional moment is given by

$$\theta_x = \int_0^{2a} \frac{M_x}{GI_x(x)} dx \tag{3.14}$$

where G is the shear modulus, and $I_x(x)$ is the torsional moment of inertia for the infinitesimal strip at position x.

Using Roark's formulas [90], $I_x(x)$ is expressed as

$$I_x(x) = wt^3(x)\left[\frac{1}{3} - 0.21\frac{t(x)}{w}\left(1 - \frac{t^4(x)}{12w^4}\right)\right] \tag{3.15}$$

Based on the polar coordinates introduced in Fig. 3.7, eq. (3.5) becomes

$$t\left(\alpha\right) = 2b + t_m - 2b\left(1 - \cos^4\alpha\right)^{\frac{1}{4}} \tag{3.16}$$

Likewise, eq. (3.15) can be expressed as

$$I_x(\alpha) = wt^3(\alpha)\left[\frac{1}{3} - 0.21\frac{t(\alpha)}{w}\left(1 - \frac{t^4(\alpha)}{12w^4}\right)\right] \tag{3.17}$$

Following a similar procedure, eq. (3.14) is expressed as

$$\theta_x = \frac{M_x a}{G}\int_0^{\pi} \frac{\sin\alpha}{I_x(\alpha)} d\alpha \tag{3.18}$$

Further, substituting ξ into eq. (3.16) yields

$$t(\alpha) = t_m \left[2\xi + 1 - 2\xi \left(1 - \cos^4 \alpha\right)^{\frac{1}{4}}\right] = t_m h(\xi) \tag{3.19}$$

Upon substituting the relation obtained in eq. (3.19) into eq. (3.17) produces

$$I_x(\alpha) = w t_m^3 h^3(\xi) \left[\frac{1}{3} - 0.21 \frac{t_m h(\xi)}{w} \left(1 - \frac{t^4 h^4(\xi)}{12 w^4}\right)\right] \tag{3.20}$$

Hence, eq. (3.18) can be written as

$$\theta_x = \frac{M_x a}{G w t^3} \int_0^{\pi} \frac{\sin \alpha}{h^3(\xi) \left[\frac{1}{3} - 0.21 \frac{t_m h(\xi)}{w} \left(1 - \frac{t_m^4 h^4(\xi)}{12 w^4}\right)\right]} d\alpha$$

Letting $n = t_m/w$, eq. (3.3) becomes

$$\theta_x = \frac{M_x a}{G w t^3} \int_0^{\pi} \frac{\sin \alpha}{h^3(\xi) \left[\frac{1}{3} - 0.21 n h(\xi) \left(1 - \frac{n^4 h^4(\xi)}{12}\right)\right]} d\alpha = \frac{M_x a}{G w t_m^3} z(\xi, n) \tag{3.21}$$

Therefore, the torsional compliance of the Lamé-notched hinge is

$$C_{\theta_x M_x} = \frac{\theta_x}{M_x} = \frac{a z(\xi, n)}{G w t_m^3} \tag{3.22}$$

As a result, the compliance matrix of the flexure hinge is obtained in block-form as

$$\mathbf{C}_h = \begin{bmatrix} \mathbf{C}_{rr} & \mathbf{C}_{rt} \\ \mathbf{C}_{rt}^T & \mathbf{C}_{tt} \end{bmatrix} \tag{3.23}$$

where

$$\mathbf{C}_{rr} = \begin{bmatrix} 277.63 & 0 & 0 \\ 0 & 24.144 & 0 \\ 0 & 0 & 999.49 \end{bmatrix} \text{ (Nm)}^{-1}, \ \mathbf{C}_{\text{rt}} = \begin{bmatrix} 0 & 0 & 0 \\ 0 & 0 & -0.3491 \times 10^{-2} \\ 0 & 0.1411 & 0 \end{bmatrix} \text{ N}^{-1} \tag{3.24}$$

$$\mathbf{C}_{tt} = \begin{bmatrix} 0.1759 \times 10^{-6} & 0 & 0 \\ 0 & 0.2263 \times 10^{-6} & 0 \\ 0 & 0 & 0.1239 \times 10^{-5} \end{bmatrix} \text{ m/N} \tag{3.25}$$

Finally, the stiffness matrix is obtained as the inverse of the compliance matrix, namely,

$$\mathbf{K}_h = \mathbf{C}_h^{-1} \tag{3.26}$$

Since the motion of accelerometers is highly dependent on the flexure hinges, the stiffness analysis of the flexure hinges is significant for the study of the accelerometer stiffness. However, flexure hinges are rarely found to be directly applied to accelerometers to realize compliant motions. Instead, the Π-joint, a mechanism with a combination of rigid links and flexure hinge, is proposed to realize compliant motions for the SBA.

3.4 SBA Structural Design

In order to address the drawback of the SBA design proposed by Cardou [5], the Π joint was improved in the realization of the SBA design discussed in this dissertation. As illustrated in Fig 3.10, instead of a pair of long beams, the notched Π-joints are used here, as shown in Fig. 3.3(b), to provide compliance along the sensitive direction. In the SBA, the rigid proof-mass is connected by three ΠΠ-limbs, with an angular separation of 120° in the plane. The notched Π-joint is realized by means of the Lamé-notched flexure hinge (minimum thickness $t_m = 20\ \mu\,\text{m}$, length $l = 210\ \mu\,\text{m}$), with single-crystal silicon. The model parameter values and material properties of the silicon are listed in Tables 3.2 and 3.3, respectively. These dimensions were obtained by trials and errors, based upon the micromachinability of the device, in order to meet design objectives.

As a design objective, the proof-mass is to be sensitive to applied accelerations along arbitrary directions in the plane and to exhibit high out-of-plane stiffness. Compared to the translations, the inevitable rotations of the proof-mass are expected to be slight by virtue of the structure stiffness. Besides, the flexure hinges are capable of providing compliant motions to the proof-mass under loading; by the same token, the hinges are not prone to cracking at their minimum-thickness region within the allowable range of displacements of the proof-mass.

The incentive of the SBA design is driven by its advantages over some other designs of

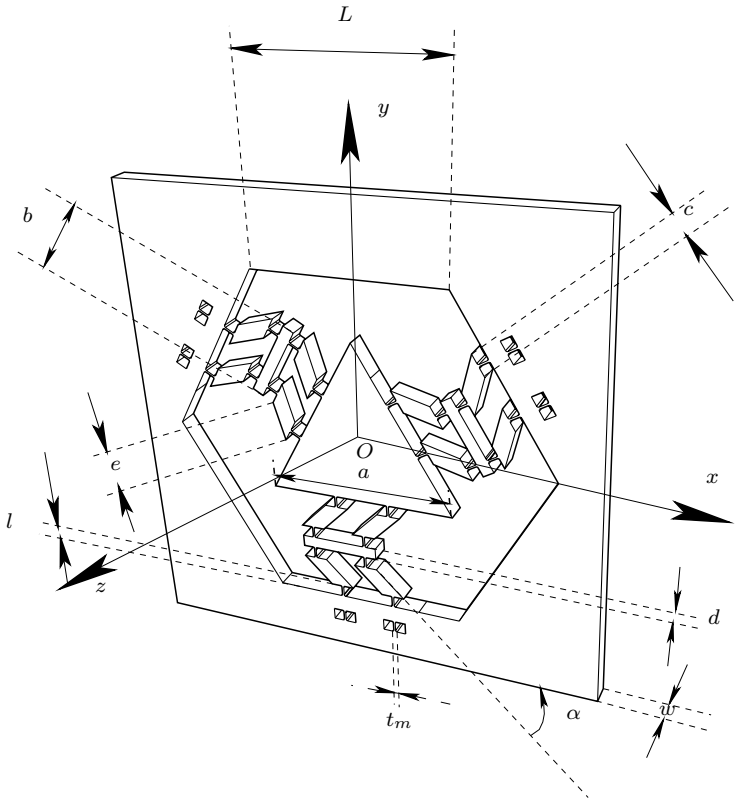

Fig. 3.10 SBA design with its dimensions

biaxial accelerometers, due to its structure. First, due to the $n+1$ leg provided by simplicial architectures, the SBA provides redundancy in the sensing signals, thereby offering robustness against measurement errors. Also, the isotropic nature of the SBA offers the same sensitivity for accelerations along any directions in the plane. Moreover, the employment of Lamé-notched hinges plays a significant role in reducing stress concentration.

Table 3.2 Dimensions of the SBA

a (μm)	b (μm)	c (μm)	d (μm)	e (μm)	l (μm)	L (μm)	t_m (μm)	α (rad)	w (μm)
3333	1400	200	210	700	210	3466	20	$\pi/4$	300

3.5 Structural Analysis

The validation procedure comprises two parts, modal analysis and forced response under various loading conditions. By means of modal analysis, we expect to obtain the

Table 3.3 Mechanical properties of silicon

Density	Stiffness Coefficients (10^3 MPa)			Young's Modulus (10^3 MPa)			Poisson Ratio
(kg/μ m^3)	C_{11}	C_{12}	C_{13}	[100]	[110]	[111]	
2.33×10^{-15}	165.7	63.9	79.6	129.5	168.0	186.5	0.222

natural frequencies, based on which the frequency ratio and frequency limit of acceleration measurements can be determined. Afterwards, the forced response under different loading conditions provides information on acceleration limit and isotropic behavior in estimating accelerations in the x-y plane. The numerical structural validation is conducted in ANSYS.

3.5.1 Damping Effects

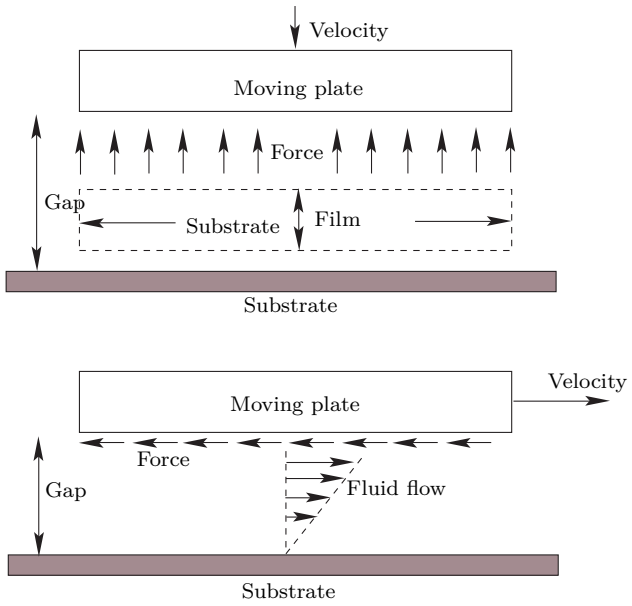

Fig. 3.11 Squeeze film and slide film damping

As illustrated in Fig. 3.11, two major types of damping occur in the micro scale SBA: squeeze-film damping and slide-film damping. According to [91], the squeeze-film damping occurs when a plate moves perpendicular to a stationary surface, i.e., squeeze-film damping takes place along the out-of-plane direction of the proof-mass. Slide-film damping arises as a plate moves parallel to a stationary surface. Consequently, slide-film damping occurs for the proof-mass motions in the plane of the SBA. It is noteworthy that no pressure variations occur in the gap between the proof-mass and the stationary surface of the package under

slide-film damping.

The damping analysis is based on the assumption of Couette air flow [92], in which the plate motion abruptly forms a fully-established linear velocity profile in the flow. Within the framework of [93], the Burgdorfer effective viscosity model for slide damping is defined as:

$$\mu_e = \frac{\mu}{1 + 6K_n} \tag{3.27}$$

where μ is the absolute air viscosity, while K_n is the dimensionless Knudsen constant [94].

Therefore, the slide-film damping coefficient C_p is derived as:

$$C_p = \frac{\mu_e A_{pm}}{g} \tag{3.28}$$

in which A_{pm} is the area of the proof-mass, and g is the gap between the proof-mass and the stationary surface. C_p has units of N.s/m.

Unlike the slide-film damping, the squeeze-film damping decreases if a gap between the proof-mass and the stationary surface arises. According to [93], the squeeze-film damping coefficient is approximated as:

$$C_s = \frac{\mu_a \alpha_p L_p w_p^3}{g^3} \tag{3.29}$$

with unit of N.s/m. In eq. (3.29), α_p is a constant parameter depending on the w_p/L_p ratio, L_p is the effective plate length and w_p the effective plate width.

Consequently, the damping matrix $\mathbf{C}$ takes the form

$$\mathbf{C} = \mathrm{diag}\left([C_p \quad C_p \quad C_s \quad 0 \quad 0 \quad 0]\right) = [\mathrm{diag}\left([2.88 \quad 2.88 \quad 8.12 \quad 0 \quad 0 \quad 0]\right)] \times 10^{-5} \text{ N.s/m} \tag{3.30}$$

3.5.2 Modal Analysis

The FE model of the SBA is shown in Fig. 3.12, in which each node has six dof. The four outside sidewalls of the SBA frame are fixed. Through modal analysis, the first six natural frequencies are listed in Table 3.4. The almost identical values of f_1 and f_2 meet the design objective of equal sensitivity for translations in the x- and y-directions. Moreover, the value of f_3 is about 2.2 times higher than that of f_1 and f_2, which means translations along the the z-direction are more constrained than those in the x-y plane. The high

frequency ratio between the rotational frequencies f_4, f_5 and f_6 and those associated with the x- and y-translations, of about 5.0, also shows an acceptable structural behavior, as required by the SBA design. The modal analysis results are also validated by the first six mode shapes, as illustrated in Fig. 3.13. Figures 3.13(a)–(c) pertain to translations along the x-, y- and z-directions, respectively. At higher frequencies, rotations appear, as shown in Figs. 3.13(d)–(f).

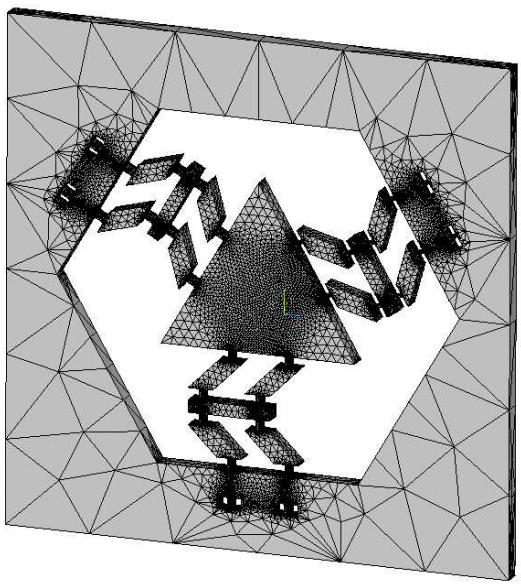

Fig. 3.12 FE model of the SBA (4-node tetrahedron element type, 53,471 nodes)

Table 3.4 Natural frequencies of the SBA through modal analysis in ANSYS

i	1	2	3	4	5	6
f_i (Hz)	5858.3	5859.1	12890	29006	29036	33051
Mode shape[2]	T_1	T_2	T_3	R_1	R_2	R_3

3.5.3 Harmonic Response

For the purpose of evaluating the dynamic performance of the SBA model, a unit loading that varies harmonically with time is applied on the SBA to study the corresponding displacement response. Consequently, the cyclic loading $a = A\sin(\omega\, t)$ m/s^2 is applied on

[2] T_i $(i = 1, 2, 3)$ denotes translation along the i-axis; R_i $(i = 1, 2, 3)$ denotes rotation about the i-axis.

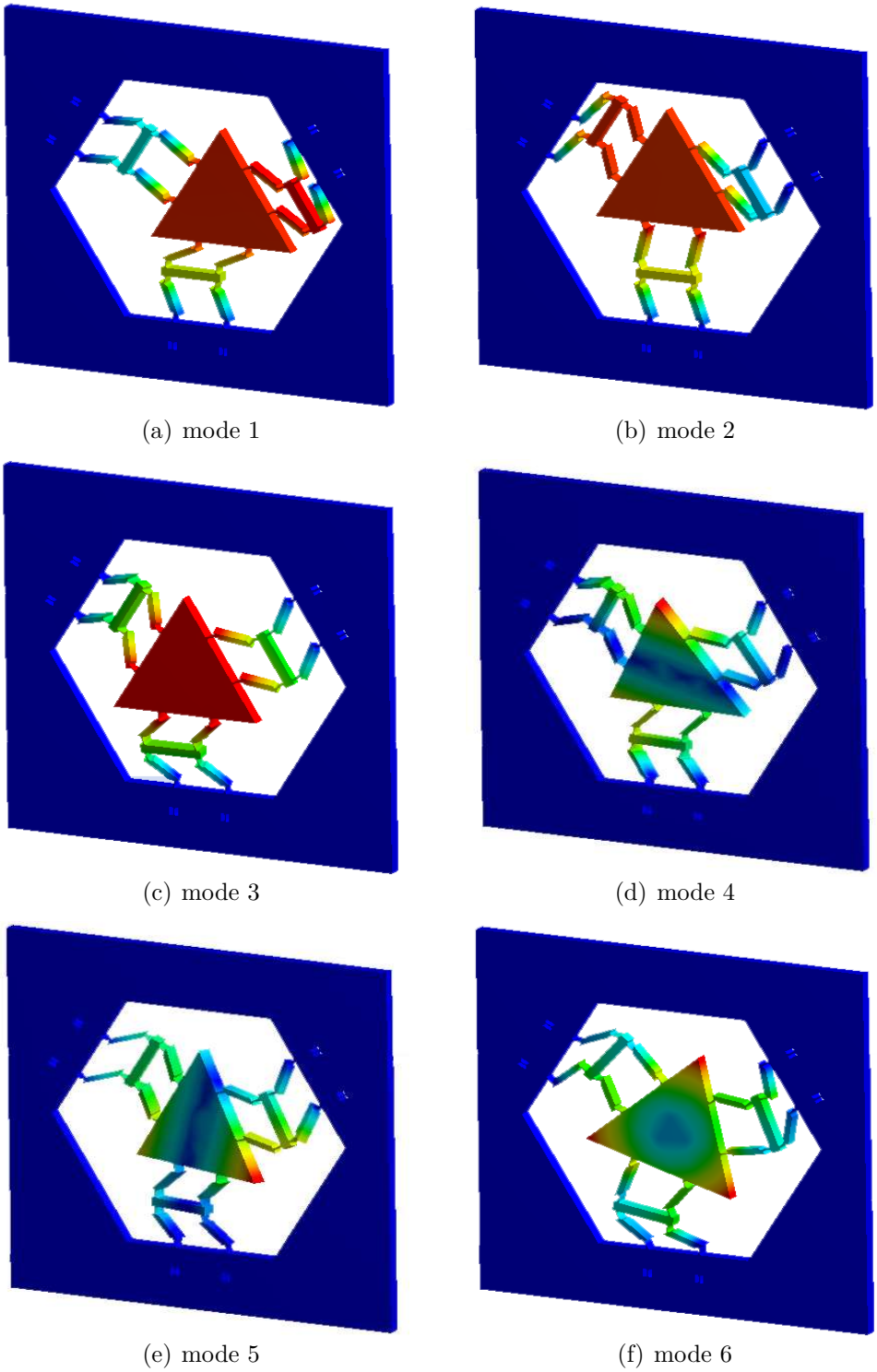

(a) mode 1 (b) mode 2

(c) mode 3 (d) mode 4

(e) mode 5 (f) mode 6

Fig. 3.13 Mode shapes of the SBA

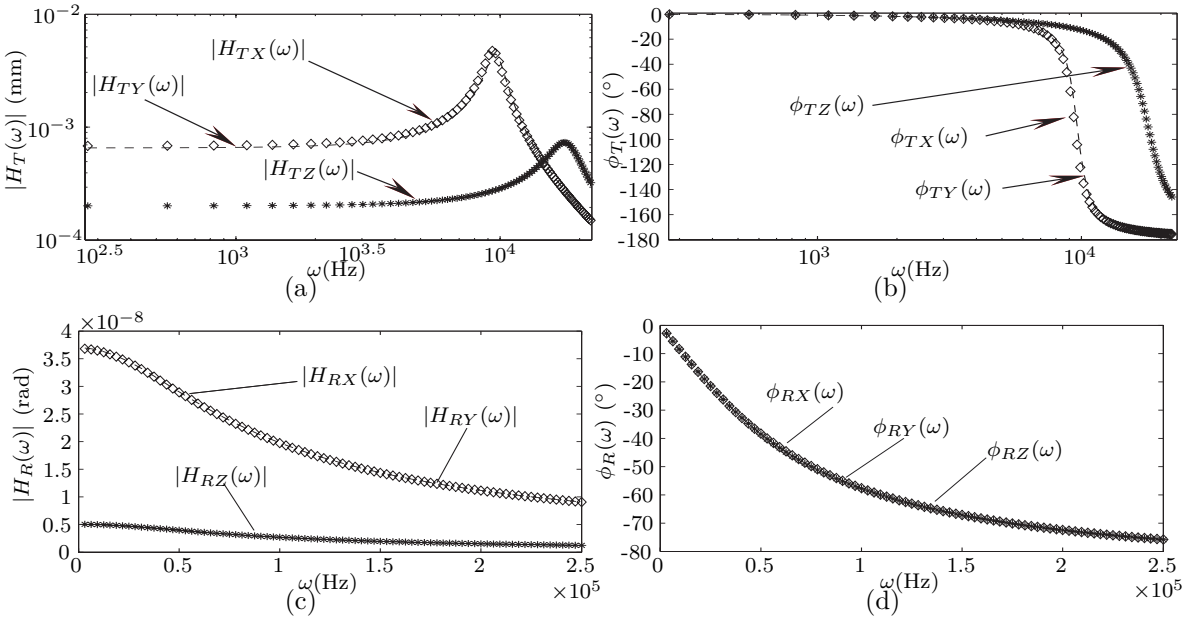

Fig. 3.14 Frequency response of the SBA:(a) translational magnitude; (b) translational phase angle; (c) rotational magnitude and (d) rotational phase angle

the proof-mass along the x-, y-, and z-axes, respectively, in ANSYS, the results being summarized in the Bode plots of Fig. 3.14. The amplitude responses of the proof-mass shown in Fig. 3.14(a) clearly illustrate that peaks appear at the critical natural frequencies along the x-, y-, and z-directions. An apparent planar isotropy of the proof-mass—$|H_{TX}(\omega)|$ and $|H_{TY}(\omega)|$—is observed. In the meantime, the out-of-plane sensitivity to accelerations is significantly lower. With reference to Carlson [95], bandwidth is the difference between upper and lower cutoff frequencies. From the plot, a bandwidth of 159 Hz is observed. With reference to the rotational amplitude responses, Fig. 3.14(c), and their phase angle counterparts Fig. 3.14(d), we conclude that within a wide range of frequencies, the rotational responses exhibit an amplitude five orders of magnitude lower than those of the in-plane translations, which tallies with the design objectives: rotations of the SBA are to be negligible.

3.5.4 Transient Analysis

The transient analysis of the SBA is conducted in ANSYS, for the purpose of obtaining the response under loading in the time domain. For the input loading, a pulse signal

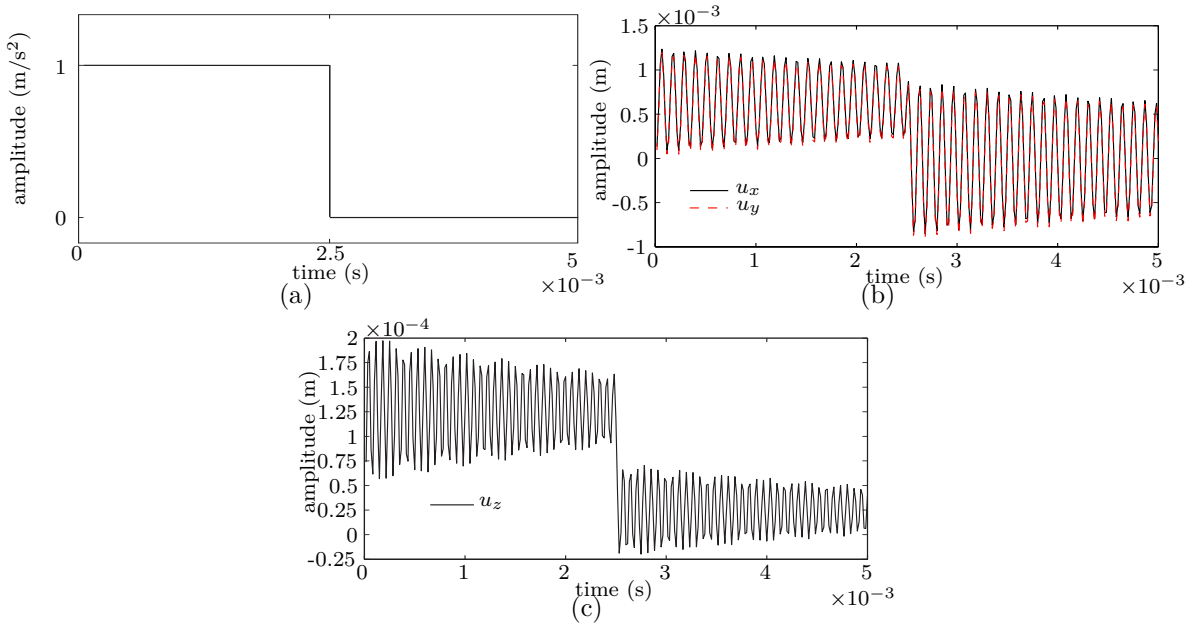

Fig. 3.15 Transient analysis of the SBA: (a) input acceleration signal; (b) output response of SBA proof-mass in its plane u_x, u_y; (c) output response of the SBA proof-mass out of its plane, u_z

of acceleration is applied on the SBA, along the x-, y-, and z-directions, respectively, as illustrated in Fig. 3.15(a). The duration of the pulse is set to 2.5×10^{-3} s, which is 15 times the period of the first and second critical frequency of 5858.3 Hz (f_X, f_Y) and 32 times that of the third critical natural frequency of 12580 Hz (f_Z). The corresponding output responses of the central node of the proof-mass are obtained by means of the Transient Analysis module in ANSYS. Figure 3.15(b) illustrates the responses along the x- and y-directions in the time domain, i.e., the responses in the plane of the SBA. An average amplitude 7.5×10^{-4} m is observed, which coincides with the first peak amplitude in the harmonic analysis. In addition, an acceptable isotropy behavior of the SBA along the x- and y- directions is observed. In comparison with the output response in the plane, the response along the z-direction is significantly small—Fig. 3.15(c)—in good agreement with the design objective of a high out-of-plane stiffness.

3.6 Piezoresistive Sensing System

3.6.1 Piezoresistive Sensing Principle

Selecting and developing a sensing method based on the comparison of different sensing technologies is an important task in this dissertation. Three main criteria are employed: sensitivity, cost and MEMS manufacturability. Among existing sensing technologies, piezoresistive sensing is attractive because it relies on a compact mechanism that requires neither complex processing circuitry nor a bulky external apparatus, besides exhibiting low susceptibility to electromagnetic interference. Moreover, simplicity for design, fabrication process and processing circuitry also feature the intrinsic advantages of piezoresistive sensing. At the same time, however, piezoresistive sensing technology suffers from low sensitivity to temperature variations. In addition, researches are seldom found to implant piezoresistive sensing technology in the design of biaxial accelerometers, which makes this alternative *terra incognita* in our context. This room for improvement helps us narrow down our search, to focus on a novel piezoresistive sensing technology for the SBA.

The piezoresistive effect is also known for the phenomenon that the resistance of a material changes under applied stresses. This effect results from both geometric changes and the change in resistivity, as[96]

$$\Delta R/R = (1 + 2\nu)\epsilon + \frac{\Delta\rho}{\rho} \tag{3.31}$$

where ν is the Poisson ratio, ϵ is the strain along the piezoresistor, while R and ρ are resistance and resistivity in the unstressed material. For semiconductor gauges, such as silicon and germanium, the changes in resistivity $\Delta\rho/\rho$ are dominant when compared with the dimensional changes in eq. (3.31). Hence, we will assume $\Delta R/R = \Delta\rho/\rho$.

The piezoresistive effect is described by a fourth-rank tensor that relates the change in resistivity to the stress [97]. For crystals with cubic symmetry, such as silicon, the

piezoresistance tensor is given, in matrix form by

$$\frac{1}{\rho}\begin{bmatrix}\Delta\rho_1\\ \Delta\rho_2\\ \Delta\rho_3\\ \Delta\rho_4\\ \Delta\rho_5\\ \Delta\rho_6\end{bmatrix} = \begin{bmatrix}\pi_{11} & \pi_{12} & \pi_{12} & 0 & 0 & 0\\ \pi_{12} & \pi_{11} & \pi_{12} & 0 & 0 & 0\\ \pi_{12} & \pi_{12} & \pi_{11} & 0 & 0 & 0\\ 0 & 0 & 0 & \pi_{44} & 0 & 0\\ 0 & 0 & 0 & 0 & \pi_{44} & 0\\ 0 & 0 & 0 & 0 & 0 & \pi_{44}\end{bmatrix}\begin{bmatrix}\sigma_1\\ \sigma_2\\ \sigma_3\\ \sigma_4\\ \sigma_5\\ \sigma_6\end{bmatrix} \tag{3.32}$$

Note that the piezoresistance coefficients depend on crystal orientation, impurity concentration and temperature [98].

The relation between the electric field and the current density is, in turn,

$$\begin{bmatrix}\varepsilon_1\\ \varepsilon_2\\ \varepsilon_3\end{bmatrix} = \begin{bmatrix}\rho+\Delta\rho_1 & \Delta\rho_6 & \Delta\rho_5\\ \Delta\rho_6 & \rho+\Delta\rho_2 & \Delta\rho_4\\ \Delta\rho_5 & \Delta\rho_4 & \rho+\Delta\rho_3\end{bmatrix}\begin{bmatrix}j_1\\ j_2\\ j_3\end{bmatrix} \tag{3.33}$$

where ε_i and j_i, $(i = 1, 2, 3)$ are the electric field and current density components along three mutually orthogonal directions, respectively.

For the piezoresistive analysis, it is necessary to learn how to transform the piezoresistive equations from one coordinate frame to another. Hence, the general expression for the longitudinal and transverse piezoresistance coefficients for a gauge in an arbitrary crystal direction is given by [99]:

$$\begin{aligned}\pi_l &= \pi_{11} - 2(\pi_{11} - \pi_{12} - \pi_{44})(l_1^2m_1^2 + l_1^2n_1^2 + m_1^2n_1^2)\\ \pi_t &= \pi_{12} + (\pi_{11} - \pi_{12} - \pi_{44})(l_1^2l_2^2 + m_1^2m_2^2 + n_1^2n_2^2)\end{aligned} \tag{3.34}$$

where (l_1, m_1, n_1) is the set of direction cosines between the longitudinal orientation and the crystal axis, (l_2, m_2, n_2) being its transverse counterpart. The resistance change is described by

$$\frac{\Delta R}{R} = \pi_l\sigma_l + \pi_t\sigma_t \tag{3.35}$$

where σ_l and σ_t are the longitudinal and transverse stress components.

3.6.2 Location of Piezoresistors

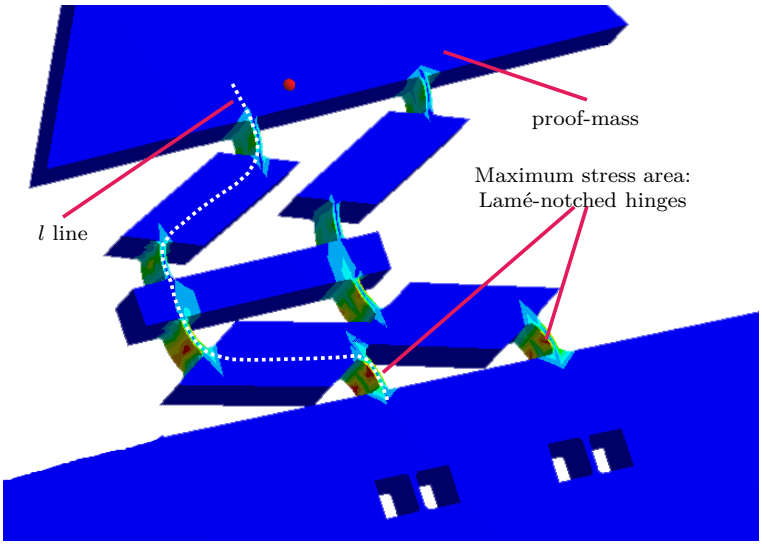

Fig. 3.16 Stress field of one limb of the SBA

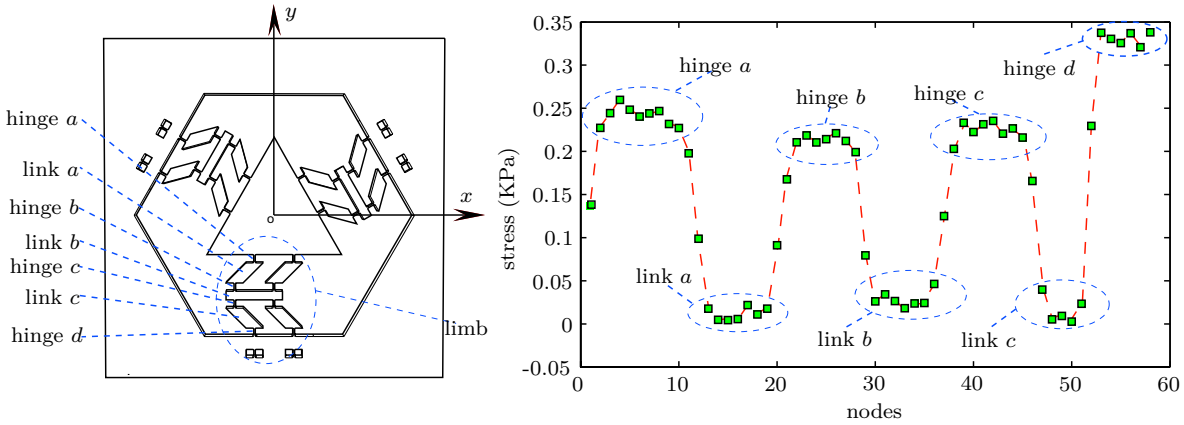

Fig. 3.17 Stress values of different areas of one limb of the SBA

Within the framework of micro system design [100], the piezoresistors are sensitive to the stress applied on it: the higher the stress it takes, the higher the voltage it will output. This phenomenon serves as the beacon for the significant criteria of locating piezoresistors in accelerometers: the piezoresistors should be attached rigidly to areas with relatively high stress values. Therefore, a stress analysis is conducted on the FE model of the SBA under ANSYS. Figure 3.16 illustrates the stress field of the SBA under an arbitrary acceleration

in the plane. It is clearly shown that the stress on the hinges is much higher than that on other regions, and the maximum stress areas appear at hinge d. This analysis is further validated through the study illustrated in Fig. 3.17. With reference to Fig. 3.16, we divide one limb of the SBA into seven parts, comprising the Lamé-notched hinges and the rigid links. Afterwards, based on the FEA of the SBA under acceleration along arbitrary planar directions, the stress values of nodes on line l for each area are plotted in Fig. 3.17. In the figure, stresses in the "hinge d" area, which is the bottom Lamé-notched hinge, are maximum, this area being ideal to locate the piezoresistors. Consequently, the piezoresistors are attached rigidly to the Lamé-notched hinges in the "hinge d" area; by doing so, the piezoresistors will show the highest sensitivity to the applied accelerations.

3.6.3 Measurement Circuit

It is assumed that the piezoresistors are located on the SBA surface with submicrometric thickness. These resistors are p-type silicon, assuming a doping concentration under 10^{17} cm^{-3}. The piezoresistance coefficients for p-type silicon are listed in Table. 3.5.

Table 3.5 Piezoresistance coefficients for p-type silicon (at room temperature)

Resistivity (Ω-cm)	Piezoresistance (10^{-11}Pa^{-1})		
	π_{11}	π_{12}	π_{44}
7.8	6.6	−1.1	138.1

Two approaches to locate the piezoresistors are considered: a) on the top surface of the notched hinge, near the edge, and b) on the vertical sidewall of the hinge, covering 1/3 of the top area. For case a), the resistor has a 120-μm length and 4-μm width; for case b), the resistor is designed so as to have dimensions of 120 × 100 μm, since a larger space is available in this layout.

As shown in Fig. 3.18(a), three measurement circuits are employed to provide voltage signals to detect the loading in an arbitrary direction in the Oxy plane. Each of the three circuits consists of four resistors connected via a half-Wheatstone bridge, as shown in Fig. 3.18(b). Taking bridge I as an example, resistors R_1 and R_2 are employed as two active Wheatstone-bridge elements, which are subject to opposite stress conditions. Furthermore, the two extra notched hinges formed on the accelerometer frame have the same structure as the two other hinges, which helps shape the two fixed bridge elements

R_3 and R_4. Figure 3.18(a) illustrates the circuit connection for bridge I for the top-surface implantation case, with the bridge drive voltage $V_s = 5V$. The connections for the other two bridges and for the vertical sidewall layout are equivalent to bridge I. It is noted that the four resistors forming a Wheatstone bridge have the same geometry, in order to provide zero-offset output voltage. At the same time, primary temperature compensation is also achieved.

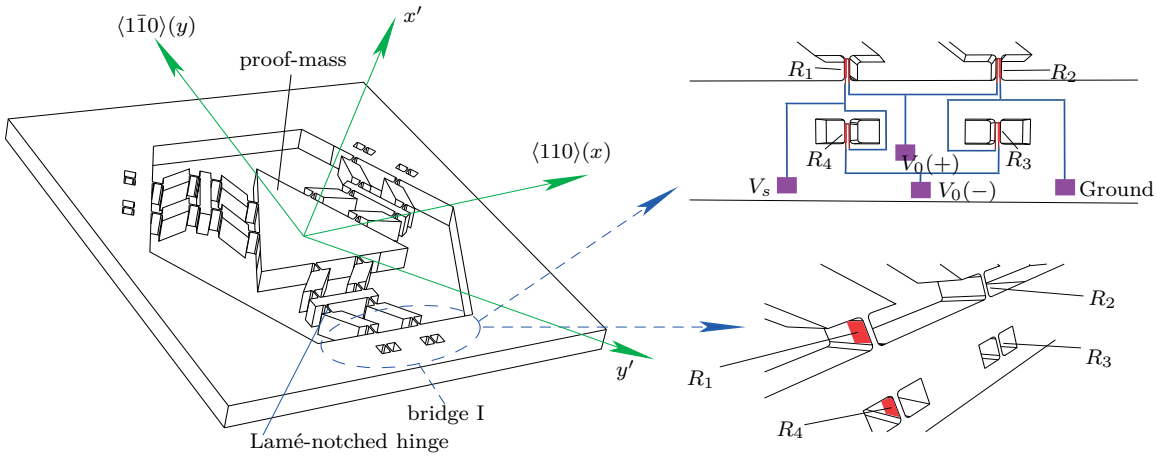

(a) measurement circuit

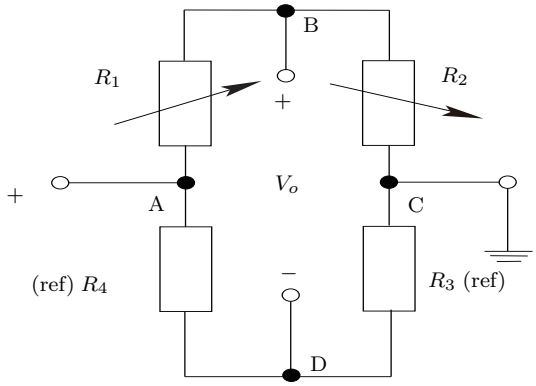

(b) half-Wheatstone bridge

Fig. 3.18 SBA geometry and sensing system

Assuming that all four resistors have identical resistance R in the absence of loading, we can write

$$R_1 = (1 + \alpha_1)R, \quad R_2 = (1 - \alpha_2)R, \quad R_3 = R_4 = R \tag{3.36}$$

where α_1 and α_2 are change rates of R_1 and R_2.

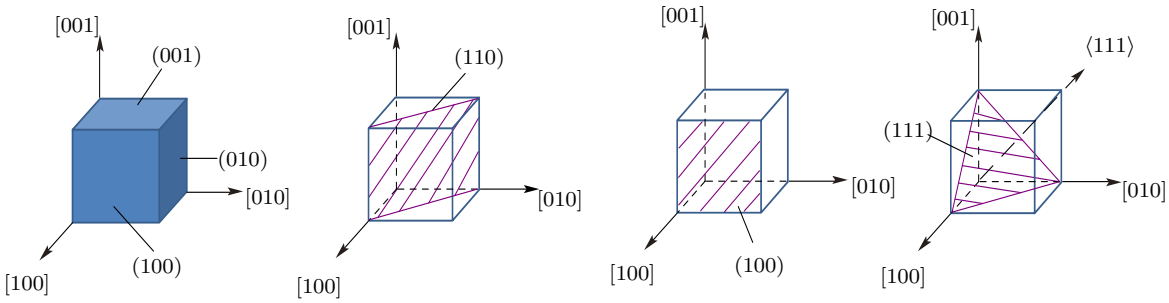

Fig. 3.19 Commonly employed crystal planes of silicon: (100), (110) and (111) planes

Hence, the resulting relation between the input and output voltages becomes

$$\frac{V_o}{V_s} = \frac{R_1}{R_1 + R_2} - \frac{R_4}{R_3 + R_4} = \frac{R_1 - R_2}{2(R_1 + R_2)} = \frac{\alpha_1 + \alpha_2}{2(2 + \alpha_1 - \alpha_2)} \tag{3.37}$$

As known in the art [100], α_1 and α_2 are typically small, and differ from each other by only 10%, the input-output ratio of the half-bridge being one-half of that of the full bridge, without a large nonlinearity. Under the assumption that R_1 and R_2 are subject to the same strain value with opposite signs, the voltage ratio becomes $V_o/V_s = \Delta R/2R$.

Figure 3.19 illustrates the crystal planes of silicon, where [ijk] denotes a vector normal to a plane described by (ijk), ⟨ijk⟩ representing all directions equivalent to [ijk]. The SBA structure starts from the n-type (100) single crystal silicon wafer. For bridge I, the resistors are oriented along the $\langle 1\bar{1}0 \rangle$ direction, which gives the maximum value for π_l, denoting the longitudinal piezoresistance coefficient of a gauge in an arbitrary crystal direction, as defined in eq. (3.34). The x'- and y'-axes, shown in Fig. 3.18(a), denote the crystal axes of symmetry of the wafer. The resistors in the two other bridges are aligned along the length direction of their corresponding hinges. Then, according to the same eq. (3.34), the piezoresistance coefficients for the resistors of the three Wheatstone bridges can be calculated, as listed in Table. 3.6, considering the two distinct layouts of resistor location.

3.6.4 Noise Analysis

Two types of noise are studied in the SBA: electronic-thermal and mechanical.

Due to piezoresitors in the Wheatstone bridge system in the SBA, two typical sources exist for the electronic-thermal noise: Johnson noise and flicker noise [101]. According to

Table 3.6 Piezoresistance coefficients for top and sidewall implanted resistors

Resistor location	Category	Bridge I	Bridge II	Bridge III
Top surface	(l_1, m_1, n_1)	$(-\sqrt{2}/2, \sqrt{2}/2, 0)$	$(\cos 15°, \cos 75°, 0)$	$(\cos 105°, \cos 195°, 0)$
	(l_2, m_2, n_2)	$(\sqrt{2}/2, \sqrt{2}/2, 0)$	$(\cos 75°, \cos 165°, 0)$	$(\cos 15°, \cos 105°, 0)$
	π_l (10^{-11}Pa^{-1})	71.8	22.9	22.9
	π_t (10^{-11}Pa^{-1})	-66.3	-17.4	-17.4
Sidewall	(l_1, m_1, n_1)	$(-\sqrt{2}/2, \sqrt{2}/2, 0)$	$(\cos 15°, \cos 75°, 0)$	$(\cos 105°, \cos 195°, 0)$
	(l_2, m_2, n_2)	$(0, 0, 1)$	$(0, 0, 1)$	$(0, 0, 1)$
	π_l (10^{-11}Pa^{-1})	71.8	22.9	22.9
	π_t (10^{-11}Pa^{-1})	-1.1	-1.1	-1.1

Barlian et al. [102], noise depends on the geometry of the piezoresistive sensors, temperature, sensor bandwidth and doping concentration.

Johnson noise, which is also known as thermal noise, is the electronic noise of the charge carrier due to thermal agitation under applied voltage. As its power spectral density (PSD) stays constant over the frequency spectrum, Johnson noise is often assumed to be white noise [103]. The Johnson noise for each piezoresistor is defined as:

$$V_j = \sqrt{4k_B TBR}\ \text{V} \tag{3.38}$$

where $k_B = 1.38 \times 10^{-23}$ J/K is the Boltzmann constant, T being the absolute temperature, B is the bandwidth, and R the resistance of the piezoresistors.

The flicker noise is relevant to the fabrication process, in which parameters such as implant dose and energy play a role in controlling it [104]. According to Tuck [105], the flicker noise comes from conductivity fluctuation in the resistor. The flicker noise is defined as:

$$V_{1/f} = V_b \sqrt{\frac{\alpha}{Nf}}\ \text{V} \tag{3.39}$$

where V_b, N and f are the bias voltage, carrier number in the piezoresistor volume and frequency, respectively, while α is an empirical non-dimensional number ranging from 10^{-7} to 10^{-3}, and is attributed to lattice quality.

As illustrated in eq. (3.39), the frequency appears in the denominator, which means that the PSD of flicker noise is inversely proportional to frequency.

Hence, the total electronic-thermal noise is obtained as

$$V_e = \sqrt{V_j^2 + V_{1/f}^2} \text{ V} \tag{3.40}$$

With reference to [102], mechanical noise is due to the mechanical resistance of the sensor seismic system, as well as the thermal-mechanical noise of the moving parts. Mechanical noise can be obtained as a function of the resonant frequency ω, mass m of the the proof-mass, damping C and absolute temperature T, as:

$$V_m = \frac{1}{g}\sqrt{\frac{4k_B T\omega}{mC}} \text{ V} \tag{3.41}$$

Mechanical noise can be minimized by increasing the mass of the proof-mass, or decreasing the resonant frequency. According to Tuck [105], mechanical noise plays a dominant role over electronic-thermal noise only at frequencies above 10 kHz.

Figure 3.20 illustrates the Johnson noise and flicker noise vs. frequency. It can be concluded that the Johnson noise $V_j = 301$ nv remains constant over the frequency spectrum. On the other hand, the flicker noise is non-negligible only at low frequencies.

The SBA is designed to have a dynamic range of 30 g, which denotes a full signal of ± 30 g, i.e., a total of 60 g. The signal-to-noise ratio (SNR) of the SBA can be either obtained from measurement data, or estimated in terms of noise and dynamic range, as:

$$\text{SNR} = 20\log_{10}\left(\frac{1}{V_e}\frac{6g}{2\sqrt{2}}\right) \text{ db} \tag{3.42}$$

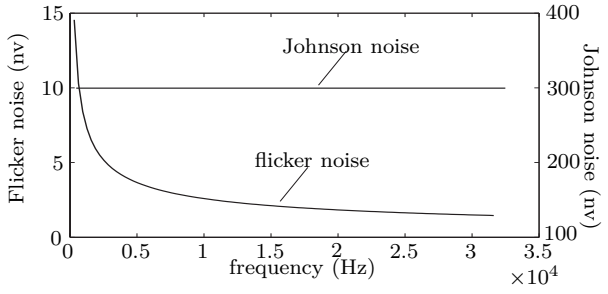

Fig. 3.20 Noise with respect to frequency spectrum

3.7 Sensing System Validation

3.7.1 Load-voltage Matrix

For simple rectangular cantilevers, closed-form expressions for the stress occurring at the point of interest in terms of structure parameters are readily derived, from which the resistance changes can be obtained, as described in [100, 106]. However, for more complex architectures, finite element modeling has been found to be an effective tool. Moreover, the piezoresistive analysis, which belongs to coupled-field analysis, is implemented by static analysis, the element type PLANE223 (2D, eight-node coupled-field element) being adopted to simulate the piezoresistors. In each static analysis, the four piezoresistors are connected via a half-Wheatstone bridge, as illustrated in Fig. 3.18(b).

Compared with conventional piezoresistive accelerometers, the SBA model provides redundancy on signal detection, i.e., three voltage measurements are generated from an arbitrary in-plane acceleration signal, which can be decomposed into the x- and y-directions. Furthermore, in order to discern the magnitude and direction of the applied loading from the three voltage measurements directly, a load-voltage matrix (LVM) is derived. The procedure for obtaining this matrix is explained below:

1. Apply three different in-plane loading cases: $F_x = 1\text{N}$; $F_y = 1\text{N}$; and $M_z = 1\,\text{N}\,\text{mm}$, with the force acting at the centre of mass of the proof-mass, and all other load components set to zero for each case.

2. Conduct a FEA for each loading case and obtain the three output voltages from the three Wheatstone bridges, namely,

$$\begin{aligned} \mathbf{v}_x &= \begin{bmatrix} v_{x_1} & v_{x_2} & v_{x_3} \end{bmatrix}^T, \quad \mathbf{v}_y = \begin{bmatrix} v_{y_1} & v_{y_2} & v_{y_3} \end{bmatrix}^T, \\ \mathbf{v}_z &= \begin{bmatrix} v_{z_1} & v_{z_2} & v_{z_3} \end{bmatrix}^T \end{aligned} \tag{3.43}$$

   where v_{x_i}, v_{y_i}, and v_{z_i} $(i = 1, 2, 3)$ denote the ith readout of the measurement circuit under the unit loads defined in item 1.

3. Then, the LVM relating the applied loading with the readout is defined as

$$\mathbf{V} = \begin{bmatrix} \mathbf{v}_x & \mathbf{v}_y & \mathbf{v}_z \end{bmatrix} \tag{3.44}$$

Hence, for a general load

$$\mathbf{w} = \begin{bmatrix} F_x & F_y & M_z \end{bmatrix}^T \tag{3.45}$$

it yields

$$\mathbf{v} = \mathbf{V}\mathbf{w} \tag{3.46}$$

where $\mathbf{v}$ denotes the three-dimensional array of readouts of the three measurement circuits.

4. In the meantime, a "small"-amplitude displacement $\mathbf{s}$ is also produced under $\mathbf{w}$:

$$\mathbf{s} = \begin{bmatrix} u_x & u_y & \theta_z \end{bmatrix}^T \tag{3.47}$$

with u_x and u_y denoting "small" translational displacements along the x and y directions, θ_z a "small" angular displacement[2] about the z axis. Then, based on the LVM $\mathbf{V}$ defined in eq. (3.44), the displacement-voltage matrix (DVM) $\mathbf{R}$ can be also obtained, which is defined as

$$\mathbf{v} = \mathbf{R}\mathbf{s} \tag{3.48}$$

Upon expressing $\mathbf{w}$ as $\mathbf{w} = \mathbf{K}\mathbf{s}$ in eq. (3.46), where $\mathbf{K}$ denotes the 3×3 in-plane system stiffness matrix obtained with ANSYS, the DVM is readily obtained as

$$\mathbf{R} = \mathbf{V}\mathbf{K} \tag{3.49}$$

3.7.2 Piezoresistive Analysis

A set of simulation runs in ANSYS is conducted to obtain the output voltage of bridge I, considering the values of the applied accelerations a_x continuously increasing. The simulation results are illustrated in Fig. 3.21, for the cases of piezoresistive sensors attached to the sidewall and top of the flexure hinges.

Figure 3.21 illustrates that for both cases, the output voltage obeys a linear relation with the applied loading. The line slope denotes the sensitivity of the sensors. Negligible offset is found in output voltage for both sensor attachments. The rms errors for these two linear fits are 0.0672% and 0.0436%, respectively. From Fig. 3.21, we can conclude that the sidewall sensor system is more sensitive to applied accelerations than its top

[2]This means $|\theta_z|$ has the maximum value in radius for which $\sin\theta_z \approx \theta_z$, i.e., $\theta_z \leqslant 3^\circ$.

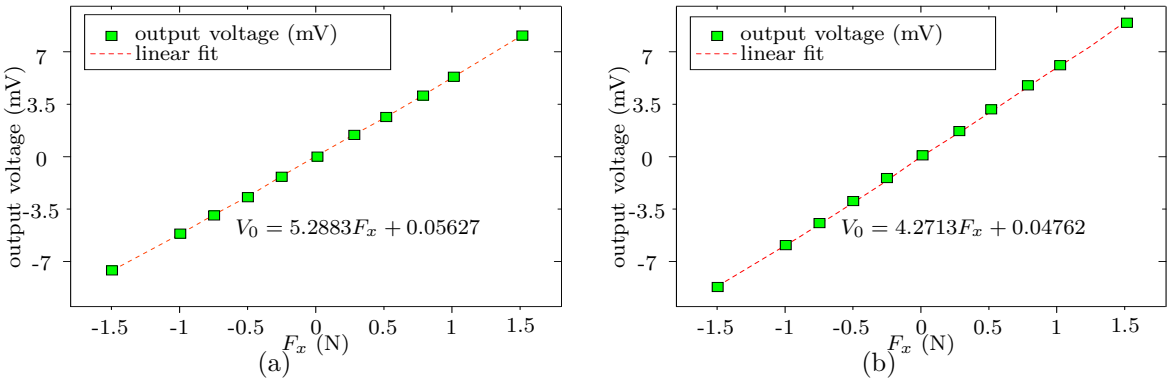

Fig. 3.21 Sensitivity of the SBA attached with the flexure hinge at: (a) sidewall; (b) top.

counterpart. However, the sensitivity differences between them are slight; in comparison with its sidewall counterpart, the top sensor system only loses a negligible sensitivity to applied accelerations.

Further, simulation tests are implemented to find the mapping matrices that relate the three output measurements with the displacement, and the voltage measurements with the applied loading. With reference to Fig. 3.10, the in-plane stiffness matrix for the whole system, as reported by ANSYS, is

$$\mathbf{K} = \begin{bmatrix} 5.58 & 7.48 \times 10^{-4} & 4.43 \times 10^{-4} \\ 7.48 \times 10^{-4} & 5.58 & 0 \\ 0 & 4.43 \times 10^{-4} & 2.77 \end{bmatrix} \tag{3.50}$$

whose 2×2 upper-left block has units of N/mm, its 2×1 and 1×2 off-diagonal blocks units of N, and its $(3,3)$ entry units of N mm.

For the piezoresistors located on the top surface,

$$\begin{aligned} \mathbf{V} &= \begin{bmatrix} 4.2713 & 6.1605 & -1.0367 \times 10^{-4} \\ -7.5018 & 0.6158 & -1.0367 \times 10^{-4} \\ 3.2051 & -6.8005 & -1.0367 \times 10^{-4} \end{bmatrix}, \\ \mathbf{R} &= \begin{bmatrix} 23.8385 & 34.3788 & 0.0016 \\ -41.8596 & 3.4306 & -0.0036 \\ 17.8794 & -37.9444 & 0.0011 \end{bmatrix} \end{aligned} \tag{3.51}$$

Table 3.7 Validation of mapping matrices

	$\mathbf{v}'$ (mv)	MAPE
Top	$\begin{bmatrix}-2.366720786 & 15.53745777 & -13.28043391\end{bmatrix}^T$	0.0057
Sidewall	$\begin{bmatrix}-2.757804278 & 18.391174 & -15.98428694\end{bmatrix}^T$	0.0082
	$\mathbf{v}$ (mv)	MAPE
Top	$\begin{bmatrix}-2.382075813 & 15.61936948 & -13.21070759\end{bmatrix}^T$	0.0057
Sidewall	$\begin{bmatrix}-2.766997431 & 18.56065200 & -16.17500793\end{bmatrix}^T$	0.0082

The 3×2 left-hand block of $\mathbf{V}$ has units of mV/N, its third column units of mV/(N mm), while the 3×2 left-hand block of $\mathbf{R}$ has units of mV/mm, its third column units of mV.

For piezoresistors located on the vertical sidewall surface,

$$\begin{aligned}\mathbf{V} &= \begin{bmatrix} 5.2883 & 7.8096 & -4.0716\times10^{-5} \\ -8.9407 & 0.6792 & -4.0716\times10^{-5} \\ 4.0492 & -8.0765 & -4.0716\times10^{-5}\end{bmatrix}, \\ \mathbf{R} &= \begin{bmatrix} 29.5146 & 43.5815 & 0.0022 \\ -49.8886 & 3.7832 & -0.0041 \\ 22.5885 & -45.0638 & 0.0017\end{bmatrix}\end{aligned} \tag{3.52}$$

The above matrices have the same units as their counterparts in eq. (3.51). In order to verify the above mapping matrices, the output voltage $\mathbf{v}$ under both top and sidewall cases is evaluated according to $\mathbf{v} = \mathbf{V}\mathbf{w}$, where $\mathbf{w} = \begin{bmatrix} -2 & 1 & 0 \end{bmatrix}^T$ N is one applied in-plane loading. In addition, the voltage readout $\mathbf{v}'$ from FEA, which is considered as the exact value here, is also recorded in Table 3.7 for comparison purposes. In the table, the mean absolute percentage error (MAPE) is used to compare $\mathbf{v}$ and $\mathbf{v}'$, which is given by

$$\text{MAPE} = \frac{1}{n}\sum_{i=1}^{n}\left|\frac{v_i' - v_i}{v_i'}\right| \tag{3.53}$$

where $n = 3$, while v_i and v_i' denote the ith entry of $\mathbf{v}$ and $\mathbf{v}'$, respectively.

3.8 Summary

In this chapter, an innovative design of biaxial accelerometers has been proposed, that is based on the architecture of a three-limb planar parallel robot whose moving platform is constrained to move under pure translation. With the use of our proposed Lamé-notched hinges, the SBA architecture relies on a combination of what is known as Π-joints. A serial array of two Π-joints with Lamé-notched hinges was devised and employed to connect the proof-mass with the supporting structure. This kind of notch was introduced in order to minimize the stress concentration and provide good compliance for the proof-mass along the sensitive axes. The accelerometer bandwidth was obtained by means of harmonic analysis, which also showed that the SBA provides the same high sensitivity to applied accelerations in any direction of its plane and exhibits low sensitivity to out-of-plane accelerations. The electronic measurement system was designed based on the foregoing structural validation. Two approaches were proposed for locating the piezoresistors, on the top surface and on the vertical sidewall of the flexure hinges. Piezoresistive analysis was conducted on the FE model of the SBA with simulation results illustrating that both approaches are effective in detecting the output voltage signal under applied accelerations. Besides, the mapping matrices that generate the acceleration signal from applied accelerations were derived for the electronic layouts.

Chapter 4

Stiffness Analysis of the SBA

4.1 Overview

In this chapter, the stiffness analysis of the SBA is conducted. The first section focuses on the stiffness analysis in terms of the energy approach based on the Lagrange's formulation. In the second section, the stiffness analysis by means of the structural approach, which considers the assembly of serial and parallel chains of flexure hinges and rigid links, is included. Based on the lumped-parameter model, the 6×6 system stiffness and mass matrices are obtained. The resultant eigenfrequencies and eigenmodes are compared with their counterparts obtained by ANSYS. The third section includes the decoupling of the Cartesian stiffness matrix, based on screw theory. The stiffness matrix is decoupled by means of a similarity transformation defined over the space of "small-amplitude" screw displacements. A case study on the decoupling of the SBA stiffness matrix is conducted to validate the stiffness decoupling method. Finally, conclusions regarding the stiffness analysis for compliant mechanisms are offered.

4.2 Accelerometer Design Process

The general process of accelerometer design is illustrated in Fig. 4.1. It is noteworthy that through the whole process, stiffness analysis plays a significant role in validating the design objectives. Otherwise, either the dimensions or materials, or both, will be revised in order to meet the stiffness criteria.

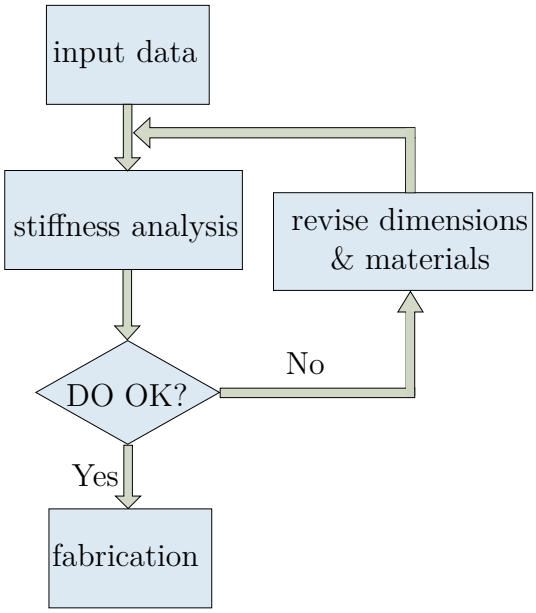

Fig. 4.1 Accelerometer design flowchart, where DO = Design Objectives

4.3 Screw Theory

The main objective of accelerometer design is to provide high compliance along the sensitive axes, and high stiffness along all other directions [107]. With the aid of screw theory, we analyze the stiffness matrix via the associated generalized eigenvalue problem.

In screw theory, the general spatial motion of the rigid body is represented by a rotation of the body about a line, called the *screw axis*, and a concomitant translation parallel to that axis [108, 109], as illustrated in Fig. 4.2(a). Furthermore, a scalar quantity p denotes the *pitch*, which couples the rotation with the translation.

A *unit screw* $\hat{\mathbf{s}}$ is represented as a six-dimensional array, namely,

$$\hat{\mathbf{s}} = \begin{bmatrix} \mathbf{e} \\ \boldsymbol{\mu} \end{bmatrix} = \begin{bmatrix} \mathbf{e} \\ \mathbf{r} \times \mathbf{e} + p\mathbf{e} \end{bmatrix} \tag{4.1}$$

where $\mathbf{e}$ is the unit vector parallel to the direction of the screw axis $\mathcal{L}$, while $\boldsymbol{\mu}$ denotes translation of the screw nut under a unit rotation of the latter. Moreover, $\mathbf{r}$ is the position vector pointing from a point R on the screw axis $\mathcal{L}$ to the origin O. Without loss of generality, R can be assumed to be the point of $\mathcal{L}$ closest to O, as depicted in Fig. 4.2(b).

It is noteworthy that a pure rotation is characterized by a zero pitch, while an infinite pitch characterizes a pure translation.

As illustrated in Fig. 4.2(a), a rigid body is displaced from Pose I to Pose II around the screw axis $\mathcal{L}$ with a pitch p.

Based on the "small-amplitude" displacement screw assumption, the screw displacement $\mathbf{s}$, the rigid-body twist $\mathbf{t}$ and the wrench $\mathbf{w}$ are obtained by multiplying the unit screw $\hat{\mathbf{s}}$ in eq. (4.1) by a "small" amplitude Θ, an arbitrary amplitude Ω with units of angular velocity, and an amplitude F with units of force, respectively:

$$\begin{aligned} \mathbf{s} &= \Theta\hat{\mathbf{s}} = \begin{bmatrix} \boldsymbol{\theta} \\ \mathbf{r} \times \boldsymbol{\theta} + p\boldsymbol{\theta} \end{bmatrix}, \quad \mathbf{t} = \Omega\hat{\mathbf{s}} = \begin{bmatrix} \boldsymbol{\omega} \\ \mathbf{r} \times \boldsymbol{\omega} + p\boldsymbol{\omega} \end{bmatrix}, \\ \mathbf{w} &= F\hat{\mathbf{s}} = \begin{bmatrix} \mathbf{f} \\ \mathbf{r} \times \mathbf{f} + p\mathbf{f} \end{bmatrix} \end{aligned} \tag{4.2}$$

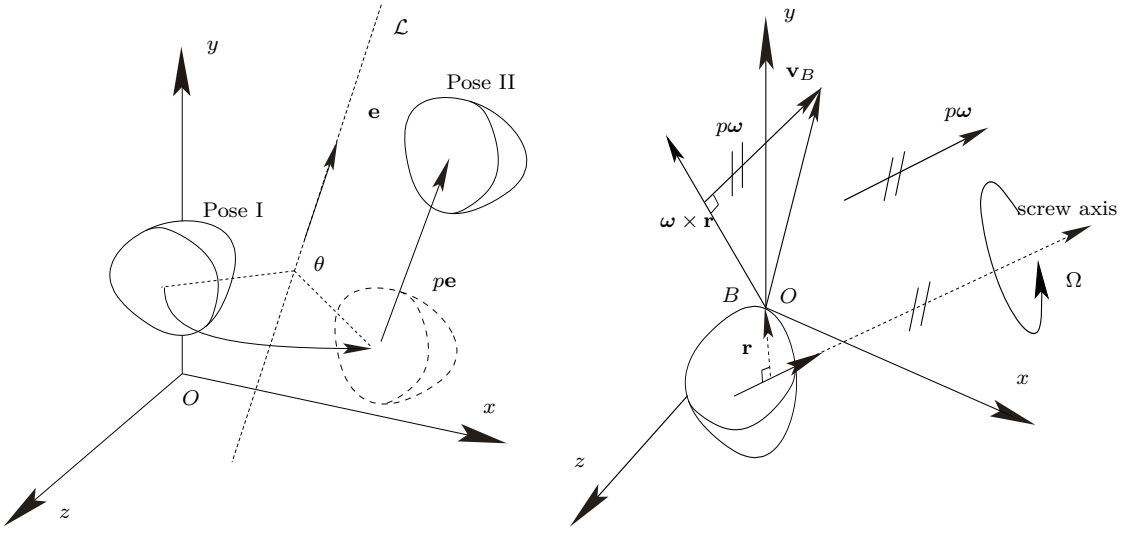

(a) Screw motion combining rotation and translation

(b) Twist screw elements: the point B of the body is instantaneously at the origin O

Fig. 4.2 Screw of a rigid body

Figure 4.2(b) depicts the screw elements of a twist $\mathbf{t}$ for a rigid body, i.e., the angular velocity $\boldsymbol{\omega}$ and the velocity $\mathbf{v}_B$ of a point B of the rigid body, the screw nut, which coincides instantaneously with the origin O.

At the outset, it is recalled that scientific code assumes that all the entries of the matrix

under eigen-analysis bear the same units, and hence, its eigenvectors can be *normalized* to render them of unit norm. In the context of eigenscrew analysis, the said norm cannot be defined, but the putative unit eigenvectors are still useful to extract the desired information from them.

Assuming that $\mathbf{k}_i$, for $i = 1, \ldots, 6$, a *unit screw*, is the i^{th} eigenvector of the 6×6 stiffness matrix $\mathbf{K}$, and κ_i the corresponding eigenvalue, the eigenvalue problem is formulated as:

$$\mathbf{K}\mathbf{k}_i = \kappa_i \mathbf{\Gamma}\mathbf{k}_i \tag{4.3}$$

where κ_i can be proven to have units of force (N) from the expansion of eq. (4.3), while $\mathbf{\Gamma}$ denotes the 6×6 permutation matrix, defined as

$$\mathbf{\Gamma} = \begin{bmatrix} \mathbf{O}_{3\times3} & \mathbf{1}_{3\times3} \\ \mathbf{1}_{3\times3} & \mathbf{O}_{3\times3} \end{bmatrix}, \quad \mathbf{\Gamma} = \mathbf{\Gamma}^{-1} \tag{4.4}$$

in which $\mathbf{O}_{3\times3}$ denotes the 3×3 zero matrix, and $\mathbf{1}_{3\times3}$ the 3×3 identity matrix, $\mathbf{\Gamma}$ thus converting screw axis- into radial coordinates [53]. Henceforth κ_i is referred to as the ith eigenforce. In screw theory, the *reciprocal product* of two screws is defined as the power Π developed by a wrench $\mathbf{w}$ acting on a rigid body that moves with a twist $\mathbf{t}$, namely,

$$\Pi = \mathbf{t}^T \mathbf{\Gamma} \mathbf{w} \tag{4.5}$$

Screws constitute vector spaces that do not admit an inner product [110]. A twist $\mathbf{t}$ is said to be reciprocal to a wrench $\mathbf{w}$ when their reciprocal product is zero, i.e., in eq. (4.5), $\Pi = 0$.

With reference to [50], based on $\mathbf{K}$, the procedure to obtain the eigenscrews is outlined below:

Let $\boldsymbol{\lambda}_i$ and λ_i denote the i^{th} *generalized* unit eigenvector and its corresponding eigenvalue, as returned from an eigenvalue solver when applied to $\mathbf{K}$:

$$\mathbf{K}\boldsymbol{\lambda}_i = \lambda_i \mathbf{\Gamma}\boldsymbol{\lambda}_i \tag{4.6}$$

whence,

$$\kappa_i \mathbf{\Gamma}\mathbf{k}_i = \lambda_i \mathbf{\Gamma}\boldsymbol{\lambda}_i \tag{4.7}$$

Since $\mathbf{\Gamma}$ is nonsingular, it is apparent that

$$\kappa_i \mathbf{k}_i = \lambda_i \boldsymbol{\lambda}_i \tag{4.8}$$

According to eq. (4.1), it is convenient to expand eq. (4.8) into block-form to calculate all the factors on the left-hand side, as:

$$\kappa_i \begin{bmatrix} \mathbf{e}_i \\ \mathbf{p}_i \times \mathbf{e}_i + p_i \mathbf{e}_i \end{bmatrix} = \lambda_i \begin{bmatrix} \boldsymbol{\eta}_i \\ \boldsymbol{\zeta}_i \end{bmatrix} \tag{4.9}$$

where $\boldsymbol{\eta}_i$ and $\boldsymbol{\zeta}_i$ are three-dimensional blocks of $\boldsymbol{\lambda}_i$ for simplicity.

Expressions for $\mathbf{e}_i$ and κ_i are readily obtained upon taking the norm of the upper blocks of the foregoing equation, and recalling that $\| \mathbf{e}_i \| = 1$, whence,

$$\mathbf{e}_i = \frac{\boldsymbol{\eta}_i}{\| \boldsymbol{\eta}_i \|}, \quad \kappa_i = \lambda_i \| \boldsymbol{\eta}_i \| \tag{4.10}$$

The i^{th} eigenpitch p_i is obtained upon equating the lower blocks of eq. (4.9), and dot-multiplying the equation thus resulting by $\mathbf{e}_i$, which yields,

$$p_i = \frac{\lambda_i}{\kappa_i} \mathbf{e}_i^T \boldsymbol{\zeta}_i \tag{4.11}$$

Similarly, $\mathbf{p}_i$ is expressed in terms of the lower blocks in eq. (4.9). For convenience, the equation is rewritten in a simple form, as:

$$\mathbf{E}_i \mathbf{p}_i = -\frac{\lambda_i}{\kappa_i} \boldsymbol{\zeta}_i + p_i \mathbf{e}_i \tag{4.12}$$

where[1] $\mathbf{E}_i$ is the *cross-product matrix* (CPM) of the vector $\mathbf{e}_i$, defined as

$$\mathbf{E}_i = \text{CPM}(\mathbf{e}_\text{i}) = \frac{\partial (\mathbf{e}_\text{i} \times \mathbf{v})}{\partial \mathbf{v}} \quad \forall \quad \mathbf{v} \in \mathbb{R}^3 \tag{4.13}$$

An additional condition is imposed upon $\mathbf{p}_i$, by defining it to be the position vector of the

[1] $\mathbf{E}_i$ is defined as the 3×3 skew-symmetric matrix with the property $\mathbf{E}_i \mathbf{p}_i \equiv \mathbf{e}_i \times \mathbf{p}_i$

point of the ith screw axis $\mathcal{L}_i$ of minimum magnitude:

$$\mathbf{e}_i^T \mathbf{p}_i = 0 \tag{4.14}$$

Then, by adjoining eq. (4.14) to eq. (4.12), an augmented system of four linear equations in the three unknown components of $\mathbf{p}_i$ is obtained:

$$\mathbf{A}_i \mathbf{p}_i = \mathbf{b}_i \tag{4.15}$$

in which,

$$\mathbf{A}_i \equiv \begin{bmatrix} \mathbf{E}_i \\ \mathbf{e}_i^T \end{bmatrix}, \quad \mathbf{b}_i \equiv \begin{bmatrix} -\dfrac{\lambda_i}{\kappa_i}\boldsymbol{\zeta}_i + p_i \mathbf{e}_i \\ 0 \end{bmatrix} \tag{4.16}$$

It is noteworthy that eq. (4.15) is an "overdetermined" linear system, but overdeterminacy is only formal, as the four equations are consistent, hence the quotation marks. Finally, based on eq. (4.15), the unique solution for vector $\mathbf{p}_i$ of minimum Euclidean norm yields,

$$\mathbf{p}_i = \frac{\boldsymbol{\eta}_i \times \boldsymbol{\zeta}_i}{\| \boldsymbol{\eta}_i \|^2} \tag{4.17}$$

thereby computing all the eigenscrew parameters in the generalized eigenvalue problem associated with the stiffness matrix.

The physical significance of screws on accelerometer stiffness is worth investigating. In the case of uniaxial accelerometers, for example, suppose that the accelerometer is mounted on a rigid body that undergoes translational and rotational motions simultaneously. According to screw theory, we can assume that the accelerometer is subjected to a small-amplitude displacement—one involving a small angle of rotation—determined by a screw $\mathbf{s}$. Then, the screw will induce a wrench. For numerous accelerometer applications, the screw axis is not the same as the wrench axis. The main objective of accelerometer design is to have the screw axis coincide with the wrench axis, which is the sensitive direction. By doing so, an applied force along the sensitive axis will cause a pure translation accordingly. This criterion is called the *force-compliant* feature-based condition for compliant mechanisms [111].

4.4 Lumped-parameter Model

For compliant mechanisms, the lumped-parameter method is interesting for the kinematic design. The key feature of the lumped-parameter approach is its relying on traditional mechanism analysis to model the compliant mechanisms as equivalent rigid link mechanisms. The stiffness of each part of the compliant mechanism is analyzed in its local frame and transformed into the global frame. By doing so, the lumped-parameter method is extended to include the stiffness analysis of spatial compliant mechanisms.

4.4.1 Lagrangian Formulation

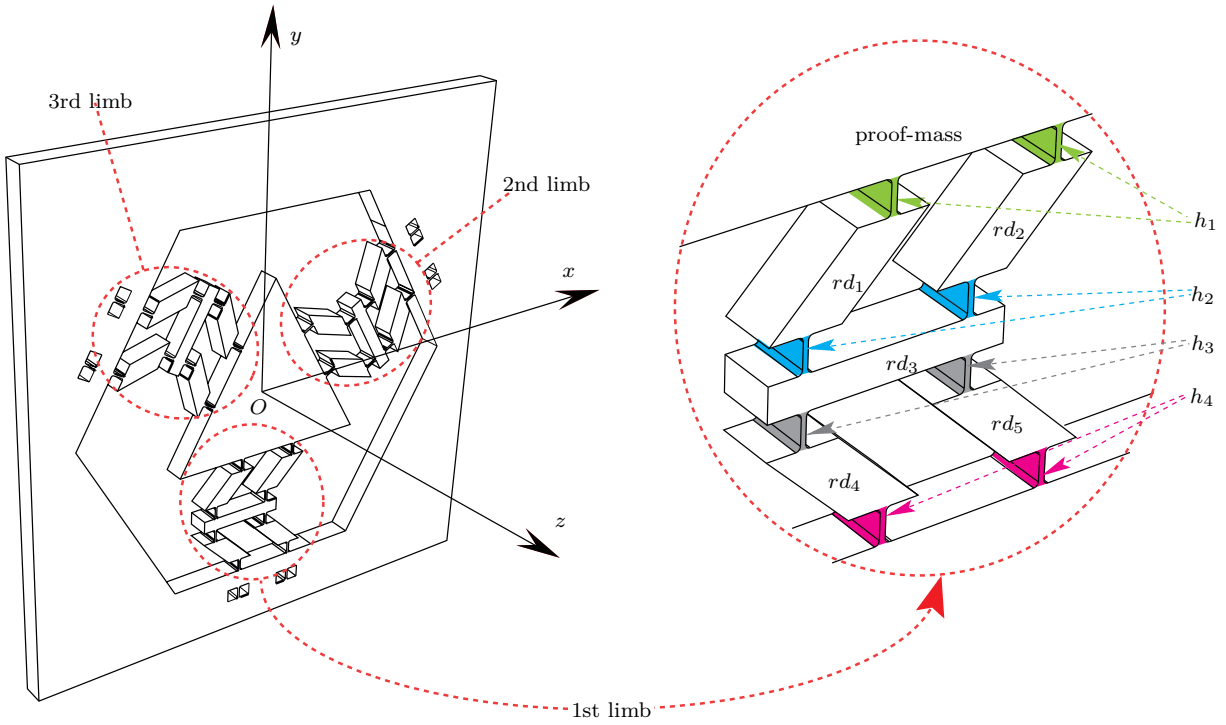

Fig. 4.3 Three limbs of the SBA

As illustrated in Fig. 4.3, each limb of the SBA is apparently composed of two categories of mechanisms: conventional and compliant. The former include rigid links, rd_1, rd_2, rd_3, rd_4, and rd_5, shown in the figure, to connect the proof-mass with the compliant hinges. Due to their rigidity, the links are assumed to have zero compliance. The latter are the Lamé-notched flexure hinges, h_1, h_2, h_3, h_4 in the same figure.

Following the Lagrangian formulation, the stiffness of the SBA can be obtained based on the kinetic and potential energies, which are investigated below:

System Kinetic Energy

The generalized small-amplitude displacement (SAD) screw $\mathbf{u}$ of the system, in frame $Oxyz$, is

$$\mathbf{u} = \begin{bmatrix} \theta_x & \theta_y & \theta_z & u_x & u_y & u_z \end{bmatrix}^T \tag{4.18}$$

where θ_x, θ_y, θ_z are the "small" angular displacements, while u_x, u_y, u_z are their translational counterparts.

Therefore, the twist $\mathbf{t}$ is obtained as the time derivative of $\mathbf{u}$, namely,

$$\mathbf{t} \equiv \dot{\mathbf{u}} \tag{4.19}$$

Since the centre of mass of the system coincides with the centre of mass of the proof-mass, letting the mass matrix of the proof-mass be $\mathbf{M}_{\rm pm}$, the kinetic energy of the proof-mass is

$$T_{\rm pm} = (1/2)\mathbf{t}^T \mathbf{M}_{\rm pm} \mathbf{t} \tag{4.20}$$

with

$$\mathbf{M}_{\rm pm} = \begin{bmatrix} \mathbf{I}_{\rm pm} & \mathbf{O} \\ \mathbf{O} & m_{\rm pm}\mathbf{1} \end{bmatrix} \tag{4.21}$$

where $\mathbf{I}_{\rm pm}$ is the inertia matrix of the proof-mass about the centre of mass, $m_{\rm pm}$ being its mass and $\mathbf{O}$ the 3×3 zero matrix. Within the framework of Reiner [112], with the SBA dimensions illustrated in Fig. 3.10, the inertia matrix of the proof-mass is

$$\mathbf{I}_{\rm pm} = \frac{m_{\rm pm} l^2}{24} \begin{bmatrix} 1 & 0 & 0 \\ 0 & 1 & 0 \\ 0 & 0 & 2 \end{bmatrix} \tag{4.22}$$

where l is the edge length of the triangular proof-mass.

The system kinetic energy also includes the kinetic energy of other rigid parts. As illustrated in Fig. 4.3, three limbs having exactly the same structure are combined to form the SBA, with their angular separation of 120° in the plane of the proof-mass. Taking the

first limb, for example, and assuming that the mass matrix for the i^{th} rigid part rd_i is $\mathbf{M}_{\text{rd}_i}$, the twist being $\mathbf{t}_{\text{rd}_i}$, then, the corresponding kinetic energy is

$$T_{\text{rd}_i} = \frac{1}{2}\mathbf{t}_{\text{rd}_i}^T \mathbf{M}_{\text{rd}_i} \mathbf{t}_{\text{rd}_i} \tag{4.23}$$

with

$$\mathbf{M}_{\text{rd}_i} = \begin{bmatrix} \mathbf{I}_{\text{rd}} & \mathbf{O} \\ \mathbf{O} & m_{\text{rd}}\mathbf{1} \end{bmatrix} \tag{4.24}$$

in which m_{rd} is the mass of the i^{th} rigid part, and $\mathbf{I}_{\text{rd}}$ is its inertia matrix about its centre of mass. Twist of all rigid links are expressed in terms of that of the proof-mass centre of mass, based upon the geometric relationship therein contained.

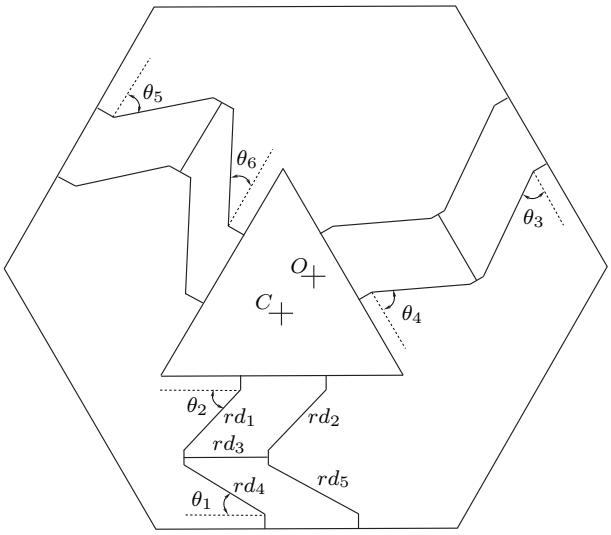

Fig. 4.4 Geometric relationship of rigid links with proof-mass centre of mass: O is the original proof-mass centre of mass, C being that in motion

As shown in Fig. 4.4, the relationship of the SAD screw of rigid links rd_1, rd_2, rd_3, rd_4, rd_5 with $\mathbf{u}$ along x and y-directions are expressed as

$$\begin{aligned} u_{x_1} = u_{x_2} &= e\cos\alpha - e\cos\theta_1 & u_{y_1} = u_{y_2} &= e\sin\theta_1 + \frac{e}{2}\sin\theta_2 - \frac{3e}{2}\sin\alpha \\ u_{x_3} &= \frac{e}{2}\cos\alpha - e\cos\theta_1 - \frac{e}{2}\cos\theta_2 & u_{y_3} &= e\sin\theta_1 - e\sin\alpha \\ u_{x_4} = u_{x_5} &= \frac{e}{2}\cos\alpha - \frac{e}{2}\cos\theta_1 & u_{y_4} = u_{y_5} &= \frac{e}{2}\sin\theta_1 - \frac{e}{2}\sin\alpha \end{aligned} \tag{4.25}$$

with $u_x = -e\left(\sin\theta_2 + \cos\theta_1\right)$, $u_y = 2e\sin\alpha - e\sin\theta_2 - e\sin\theta_1$.

It is noteworthy that relationship of screw components along the out-of-plane and rotational directions of rigid links with those of the proof-mass is not straightforward, thus their analysis results are not accurate.

We can now obtain the kinetic energy of the first limb as the sum of the kinetic energies of the composed rigid parts T_{rd_i}, namely,

$$T_1 = \sum_{i=1}^{5} T_{\mathrm{rd}_i} \tag{4.26}$$

Likewise, following a similar procedure, the kinetic energy of the second and third limbs can be obtained, which are denoted as T_2 and T_3, respectively. Therefore, the total kinetic energy of the SBA is obtained as:

$$T = T_{\mathrm{pm}} + \sum_{i=1}^{3} T_1 \tag{4.27}$$

System Potential Energy

The system potential energy involves the elastic deformation of the flexure hinges, caused by the displacement of the proof-mass. It is noteworthy that the rigid parts have no influence on the system potential energy. In order to obtain the system potential energy, the assumptions below are introduced:

- All the calculations are conducted in the global coordinate frame, whose origin is located at the proof-mass centre of mass.
- Both the translational and rotational motions of the flexure hinges are small.
- The mass and moment of inertia of the flexure hinges are ignored.
- All flexure hinges are Lamé-notched hinges and have the same compliance.
- Each pair of parallel hinges h_1, h_2, h_3, h_4, as illustrated in Fig. 4.3, has the same motion amplitudes under a SAD undergone by the proof-mass centre of mass[2].

[2]In Fig. 4.3, a colour code for stress intensity is used, which is visible on the pdf file of the thesis.

Based upon the above assumptions, the SAD $\mathbf{u}_{\mathrm{h}_i}$ for hinge h_i is defined, as

$$\mathbf{u}_{\mathrm{h}_i} = \begin{bmatrix} \theta_{\mathrm{h}_{x_i}} & \theta_{\mathrm{h}_{y_i}} & \theta_{\mathrm{h}_{z_i}} & u_{\mathrm{h}_{x_i}} & u_{\mathrm{h}_{y_i}} & u_{\mathrm{h}_{z_i}} \end{bmatrix}^T \tag{4.28}$$

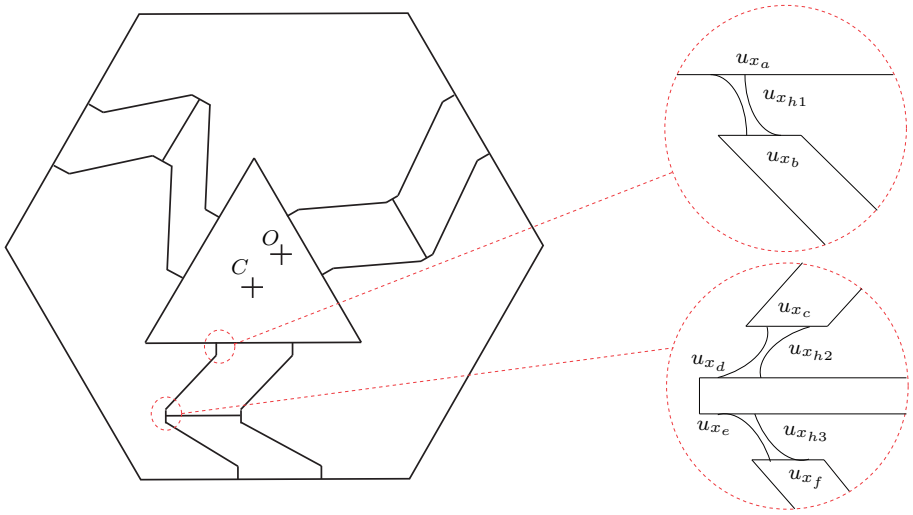

Fig. 4.5 Deformation of flexure hinges: O is the original proof-mass centre of mass, C being that in motion

Since a SAD is given to the proof-mass centre of mass, it is possible to derive the deformation for each flexure hinge $\mathbf{u}_{hi}$ with respect to $\mathbf{u}$. Through this way, the deformation of each flexure hinge is assumed as the subtraction of the displacements of the two rigid links end planes connecting to it.

As illustrated in Fig. 4.5, SAD screw components along x-direction of flexure hinges h_1, h_2, h_3 are obtained as

$$u_{x_{h1}} = u_{x_a} - u_{x_b}, \quad u_{x_{h2}} = u_{x_c} - u_{x_d}, \quad u_{x_{h3}} = u_{x_e} - u_{x_f} \tag{4.29}$$

where u_{x_i}, $i = a, b, c, d, e, f$ are SAD screw components along x-direction of the rigid-link end-plane connecting the flexure hinges. By the same token, deformation of the flexure hinges along y-direction is calculated. Deformations along the out-of-plane direction and rotational directions of flexure hinges cannot be accurately obtained.

Hence, the procedure for obtaining the potential energy of the i^{th} Lamé-notched hinge becomes straightforward; it is expressed as

$$V_{\text{h}_i} = \frac{1}{2}\mathbf{u}_{\text{h}_i}^T \mathbf{K}_{\text{h}} \mathbf{u}_{\text{h}_i} \tag{4.30}$$

where $\mathbf{K}_{\text{h}}$ is the 6×6 stiffness matrix of the Lamé-notched hinge, which was studied in Section 3.3.

The potential energy for the first limb is expressed as

$$V_1 = \sum_{i=1}^{4} V_{\text{h}_i} \tag{4.31}$$

Hence, the system potential energy is the sum of the potential energies of all the limbs, namely,

$$V = \sum_{i=1}^{3} V_i \tag{4.32}$$

Lagrange's Equations

Within D'Souza et al.'s framework [113], the dynamics equations of the system can be obtained following Lagrange's formulation. With the Lagrangian defined as $L = T - V$, the governing equations are

$$\frac{d}{dt}\left(\frac{\partial L}{\partial \dot{\mathbf{u}}}\right) - \frac{\partial L}{\partial \mathbf{u}} = \mathbf{0} \tag{4.33}$$

Equation (4.33) can be cast in compact form as

$$\mathbf{M}_{\text{sys}}\ddot{\mathbf{u}} + \mathbf{K}_{\text{sys}}\mathbf{u} = \mathbf{0} \tag{4.34}$$

in which $\mathbf{M}_{\text{sys}}$ and $\mathbf{K}_{\text{sys}}$ are the resultant system mass and stiffness matrices, respectively.

As a result, the system stiffness matrix is:

$$\mathbf{K}_{\text{sys}} = \begin{bmatrix} \mathbf{K}_{rr} & \mathbf{K}_{rt} \\ \mathbf{K}_{rt}^T & \mathbf{K}_{tt} \end{bmatrix} \tag{4.35}$$

with the various blocks displayed below:

$$\mathbf{K}_{rr} = \begin{bmatrix} 0.1131 & 0 & 0 \\ 0 & 0.2354 & 0 \\ 0 & 0 & 0.2878 \end{bmatrix} \times 10^{-4}\ \text{Nm}, \quad \mathbf{K}_{rt} = \begin{bmatrix} 0 & 0 & 0 \\ 0 & 0 & 19.378 \\ -0.7054 & 0 & 0 \end{bmatrix} \times 10^{-4}\ \text{N},$$
$$\mathbf{K}_{tt} = \begin{bmatrix} 4.9968 & 0 & 0 \\ 0 & 5.5942 & 0 \\ 0 & 0 & 13.4021 \end{bmatrix} \times 10^{3}\ \text{N/m} \tag{4.36}$$

in which $\mathbf{K}_{rr}$ is the rotational stiffness matrix, $\mathbf{K}_{tt}$ denoting the translational stiffness matrix, $\mathbf{K}_{rt}$ being the coupling stiffness matrix.

The mass matrix is

$$\mathbf{M}_{\text{sys}} = \begin{bmatrix} \mathbf{I} & \mathbf{O}_{3\times3} \\ \mathbf{O}_{3\times3} & m\mathbf{1} \end{bmatrix} \tag{4.37}$$

where $m = 0.3095 \times 10^{-6}$ kg is the mass of the proof-mass, $\mathbf{I}$ being its inertia matrix about the centre of mass, which is

$$\mathbf{I} = \begin{bmatrix} 0.4755 & 0 & 0 \\ 0 & 0.4755 & 0 \\ 0 & 0 & 0.5833 \end{bmatrix} \times 10^{-12}\ \text{kgm}^2 \tag{4.38}$$

4.4.2 Structure Description

As shown in Fig. 4.3, each limb of the SBA is composed of both serial and parallel chains of flexure hinges and rigid links. As can be seen from Fig. 4.6(a), a serial chain consists of several rigid links and flexure joints. The small spheres indicate flexure hinges, the parallelepipeds indicating rigid links. A parallel chain can be described as a rigid proof-mass connected by a set of serial chains, as shown in Fig. 4.6(b). Before analyzing the mechanical characteristics of both chains, several assumptions are listed below:

- The limb can be composed of either a serial or a parallel chain, or even of both.
- Both rigid links and flexure joints are considered flexure members.
- The compliance matrix of rigid links is assumed to vanish.

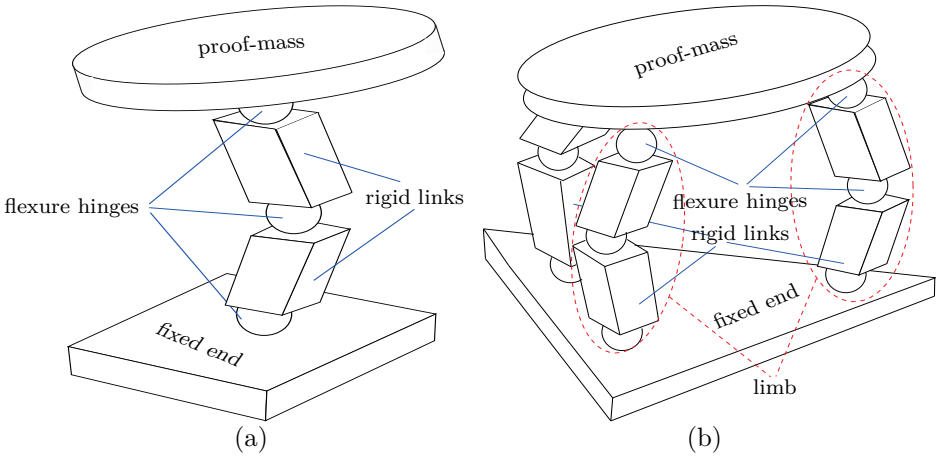

Fig. 4.6 Flexure hinge chains: (a) serial; (b) parallel

Compliant Serial Chain

For the i^{th} flexure member, let $\mathbf{s}_i$ be a six-dimensional SAD screw expressed in the reference frame $Oxyz$ attached at the chain end-plane, and $\mathbf{s}_i^{\text{loc}}$ its local counterpart at its local frame $O_ix_iy_iz_i$. Therefore,

$$\mathbf{s}_i = \mathbf{J}_i\mathbf{s}_i^{\text{loc}} \tag{4.39}$$

where $\mathbf{H}_i$, the matrix transforming $\mathbf{s}_i^{\text{loc}}$ into $\mathbf{s}_i$, is now introduced [114, 115]:

$$\mathbf{H}_i = \begin{bmatrix} \mathbf{R}_i & \mathbf{O} \\ -\mathbf{R}_i\mathbf{D}_i & \mathbf{R}_i \end{bmatrix} \tag{4.40}$$

in which $\mathbf{R}_i$ denotes the rotation matrix from local frame $O_ix_iy_iz_i$ to the reference frame $Oxyz$, while $\mathbf{O}$ is the 3×3 zero matrix, and $\mathbf{D}_i$ is the cross-product matrix of the vector $\mathbf{d}_i$ pointing from O_i to O, namely,

$$\mathbf{D}_i = \text{CPM}(\mathbf{d}_\text{i}) = \frac{\partial(\mathbf{d}_\text{i} \times \mathbf{v})}{\partial \mathbf{v}} \quad \forall \quad \mathbf{v} \in \mathbb{R}^3 \tag{4.41}$$

Likewise, the external wrench $\mathbf{w}$ at the chain end-plane expressed in frame $Oxyz$ is balanced by the reaction wrench $\mathbf{w}_i^{\text{loc}}$ at $O_ix_iy_iz_i$, namely,

$$\mathbf{w}_i^{\text{loc}} = \mathbf{H}_i^T\mathbf{w} \tag{4.42}$$

In a serial chain, all n hinges are assumed flexure members, each behaving as a spring with stiffness matrix $\mathbf{K}_i^{\text{loc}}$ in frame $O_i x_i y_i z_i$.

According to the deformation relationship of the serial chain, the SAD $\mathbf{s}$ at the end-plane is the summation of the individual SADs of all the flexure members, namely,

$$\mathbf{s} = \sum_{i=1}^{n} \mathbf{s}_i = \sum_{i=1}^{n} \mathbf{H}_i \mathbf{s}_i^{\text{loc}} \tag{4.43}$$

Based on eqs. (4.39–4.43), the desired transformation is obtained as

$$\mathbf{C}_s \mathbf{w} = \sum_{i=1}^{n} \mathbf{H}_i \mathbf{C}_i^{\text{loc}} \mathbf{w}_i^{\text{loc}} = \sum_{i=1}^{n} \mathbf{H}_i \mathbf{C}_i^{\text{loc}} \mathbf{H}_i^T \mathbf{w} \tag{4.44}$$

Consequently, the complete compliance of the serial chain becomes [35]

$$\mathbf{C}_s = \sum_{i=1}^{n} \mathbf{H}_i \mathbf{C}_i^{\text{loc}} \mathbf{H}_i^T \tag{4.45}$$

Compliant Parallel Chain

A typical example of parallel chain is illustrated in Fig. 4.6(b). It is noteworthy that, due to the rigidity of the proof-mass, the end-plane of each limb and the proof-mass have the same translational and rotational displacements.

For parallel chains, the end-plane SAD of all n limbs is the same, namely,

$$\mathbf{s} = \mathbf{H}_1 \mathbf{s}_1 = \mathbf{H}_2 \mathbf{s}_2 = \cdots = \mathbf{H}_n \mathbf{s}_n \tag{4.46}$$

where $\mathbf{s}_i$ is the SAD of the i^{th} limb in its local frame $O_i x_i y_i z_i$, while $\mathbf{s}$ denotes the SAD of one landmark point O on the proof-mass, and $\mathbf{H}_i$ is the transformation matrix from frame $O_i x_i y_i z_i$ to frame $Oxyz$, which takes the form displayed in eq. (4.40).

Meanwhile, with reference to eq. (4.42), a wrench $\mathbf{w}$ applied to point O on the proof-mass is the sum of each wrench $\mathbf{w}_i$ acting on the i^{th} limb, i.e.,

$$\mathbf{w} = \sum_{i=1}^{n} (\mathbf{H}_i^T)^{-1} \mathbf{w}_i \tag{4.47}$$

Further, with $\mathbf{K}_p$ and $\mathbf{K}_i$ denoting the stiffness matrices of the parallel chain structure

and the i^{th} limb, respectively, eq. (4.47) can be rewritten as

$$\mathbf{w} = \mathbf{K}_p\mathbf{s} = \sum_{i=1}^{n} \mathbf{H}_i^{-T}\mathbf{w}_i = \sum_{i=1}^{n} \mathbf{H}_i^{-T}\mathbf{K}_i\mathbf{s}_i = \sum_{i=1}^{n} \mathbf{H}_i^{-T}\mathbf{K}_i\mathbf{H}_i^{-1}\mathbf{s} \tag{4.48}$$

Consequently, the stiffness matrix of the parallel chain is obtained as [34]:

$$\mathbf{K}_p = \sum_{i=1}^{n} \mathbf{H}_i^{-T}\mathbf{K}_i\mathbf{H}_i^{-1} \tag{4.49}$$

SBA Limb Stiffness Analysis

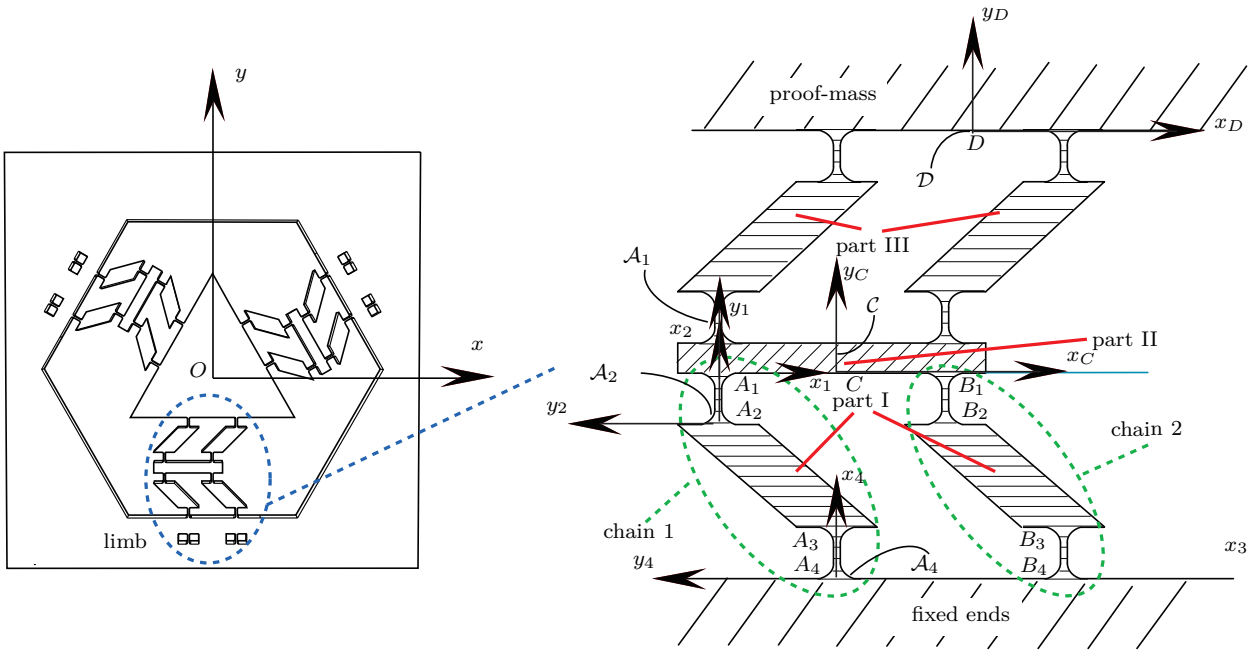

Fig. 4.7 Serial and parallel chains of the SBA limb

Figure 4.7 shows one SBA limb composed of both serial and parallel chains. The limb can be regarded as a serial combination of two Π joints and one intermediate rigid link, labeled parts I, III, and II, respectively. The parts are combined as a serial chain, whose bottom and top parts are connected to the fixed-end and to the proof-mass, respectively. For each part, the stiffness and compliance matrices, $\mathbf{K}_i^{\text{loc}}$, $\mathbf{C}_i^{\text{loc}}$, where $i = \text{I}, \text{II}, \text{III}$, are calculated in the corresponding local frames; a transformation matrix $\mathbf{H}_i$ is then introduced

to transform them into the global frame $Oxyz$, which is attached at the centre of mass of the proof-mass.

1. **Part I Compliance Matrix**
   Part I is a Π joint and can be regarded as a parallel chain, as "chain 1" and "chain 2" illustrated in Fig. 4.7. Each chain is composed of two Lamé-notched hinges (A_1-A_2, A_3-A_4, B_1-B_2, B_3-B_4) and one rigid link (A_2-A_3, B_2-B_3). In the reference frame $\mathcal{A}_1$, attached at point A_1, the total compliance matrix of chain 1 is obtained as

$$\mathbf{C}_{\text{ch1}} = \text{diag}\left(\mathbf{C}_{A_1A_2}, \mathbf{C}_{A_3A_4}\right) \tag{4.50}$$

   in which $\mathbf{C}_{A_1A_2}$ and $\mathbf{C}_{A_3A_4}$ denote the local compliance matrices of the flexure hinges in frames $\mathcal{A}_2$ and $\mathcal{A}_4$, respectively.

   Further, the 6×12 transformation matrix that transforms the local compliance matrix of each flexure member to the reference frame $\mathcal{A}_1$ is written as

$$\mathbf{H}_{\text{ch1}} = \left[\mathbf{H}_{A_1A_2}, \mathbf{H}_{A_3A_4}\right] \tag{4.51}$$

   where

$$\mathbf{H}_{A_1A_2} = \begin{bmatrix} \mathbf{R}_z\left(-\frac{\pi}{2}\right) & \mathbf{O} \\ -\mathbf{R}_z\left(-\frac{\pi}{2}\right)\mathbf{D}_{A_1A_2} & \mathbf{R}_z\left(-\frac{\pi}{2}\right) \end{bmatrix}, \quad \mathbf{H}_{A_3A_4} = \begin{bmatrix} \mathbf{R}_z\left(-\frac{\pi}{2}\right) & \mathbf{O} \\ -\mathbf{R}_z\left(-\frac{\pi}{2}\right)\mathbf{D}_{A_3A_4} & \mathbf{R}_z\left(-\frac{\pi}{2}\right) \end{bmatrix} \tag{4.52}$$

   in which $\mathbf{D}_{A_1A_2} \equiv \text{CPM}\left(\mathbf{d}_{A_2A_1}\right)$, and $\mathbf{D}_{A_3A_4} \equiv \text{CPM}\left(\mathbf{d}_{A_4A_1}\right)$, with $\mathbf{d}_{A_2A_1}$ and $\mathbf{d}_{A_4A_1}$ denoting vectors pointing from point A_2 to A_1 and A_4 to A_1, respectively. With reference to eq. (4.40), $\mathbf{R}_z\left(-\pi/2\right)$ here denotes that, frames $\mathcal{A}_2$ and $\mathcal{A}_4$ can be rotated into frame $\mathcal{A}_1$, by an angle of $-\pi/2$ about z-axis.

   Therefore, with reference to eq. (4.45), the compliance matrix of chain 1 in frame $\mathcal{A}_1$ is

$$\left[\mathbf{C}_{\text{ch1}}\right]_{\mathcal{A}_1} = \mathbf{H}_{\text{ch1}}\mathbf{C}_{\text{ch1}}\mathbf{H}_{\text{ch1}}^T \tag{4.53}$$

   The stiffness matrix of the same chain is obtained as the inverse of its compliance matrix:

$$\left[\mathbf{K}_{\text{ch1}}\right]_{\mathcal{A}_1} = \left[\mathbf{C}_{\text{ch1}}\right]_{\mathcal{A}_1}^{-1} \tag{4.54}$$

By the same token, the stiffness matrix $[\mathbf{K}_{\text{ch2}}]_{\mathcal{B}_1}$ of chain 2 in frame $\mathcal{B}_1$, the corresponding local frame attached at point B_1, can be obtained following the same procedure.

Moreover, as illustrated in Fig. 4.7, the midpoint C between A_1 and B_1, is chosen as the origin of the reference frame $\mathcal{C}$ to express the total stiffness matrix $\mathbf{K}_{\text{I}}$ of part I. Hence, according to eq. (4.49), $\mathbf{K}_{\text{I}}$, expressed in frame C, is obtained as

$$\mathbf{K}_{\text{I}} = \mathbf{H}'_{\text{I}}\mathbf{K}_{\text{I}}\mathbf{H}_{\text{I}} \tag{4.55}$$

where $\mathbf{H}'_{\text{I}} = \begin{bmatrix}\mathbf{H}_{\text{A}_1\text{C}}^{-T} & \mathbf{H}_{\text{B}_1\text{C}}^{-T}\end{bmatrix}$, $\mathbf{K}_{\text{I}} = \text{diag}\left([\mathbf{K}_{\text{ch1}}]_{A_1} \quad [\mathbf{K}_{\text{ch2}}]_{B_1}\right)$ and $\mathbf{H}_{\text{I}} = \begin{bmatrix}\mathbf{H}_{\text{A}_1\text{C}}^{-1} & \mathbf{H}_{\text{B}_1\text{C}}^{-1}\end{bmatrix}$, with

$$\mathbf{H}_{\text{A}_1\text{C}} = \begin{bmatrix}\mathbf{1} & \mathbf{O}\\ -\text{CPM}\left(\mathbf{d}_{A_1C}\right) & \mathbf{1}\end{bmatrix}, \quad \mathbf{H}_{\text{B}_1\text{C}} = \begin{bmatrix}\mathbf{1} & \mathbf{O}\\ -\text{CPM}\left(\mathbf{d}_{B_1C}\right) & \mathbf{1}\end{bmatrix} \tag{4.56}$$

where $\mathbf{d}_{A_1C}$ denote the vector pointing from point A_1 to C, $\mathbf{d}_{B_1C}$ being the vector pointing from point A_1 to C.

2. **Part II Compliance Matrix**
   It is noteworthy that the compliance matrix of the rigid links vanishes, i.e.,

$$\mathbf{C}_{\text{II}} = \mathbf{O}_{6\times 6} \tag{4.57}$$

3. **Part III Compliance Matrix**
   As shown in Fig. 4.7, with reference to frame $\mathcal{D}$, a similar procedure is applied to obtain the compliance and stiffness matrices $\mathbf{C}_{\text{III}}$ and $\mathbf{K}_{\text{III}}$, respectively, of Part III.

4. **Limb Stiffness Matrix**
   Based on the compliance matrices of each part in its local frame $[\mathbf{C}_{\text{I}}]_{\mathcal{C}}$, $[\mathbf{C}_{\text{III}}]_{\mathcal{D}}$, the complete compliance matrix of the first limb in the global coordinate frame $Oxyz$ is obtained following eq. (4.45):

$$\mathbf{C}_1 = \mathbf{H}_1\mathbf{C}_1^{\text{loc}}\mathbf{H}_1^T \tag{4.58}$$

in which $\mathbf{H}_1 = [\mathbf{H}_{CO}\,\mathbf{H}_{DO}]$, while $\mathbf{C}_1^{\mathrm{loc}} = \mathrm{diag}\,([\mathbf{C}_{\mathrm{I}}]_{\mathcal{C}}, [\mathbf{C}_{\mathrm{III}}]_{\mathcal{D}})$, with

$$\mathbf{H}_{CO} = \begin{bmatrix} \mathbf{1} & \mathbf{O} \\ -\mathbf{D}_{CO} & \mathbf{1} \end{bmatrix}, \quad \mathbf{H}_{DO} = \begin{bmatrix} \mathbf{1} & \mathbf{O} \\ -\mathbf{D}_{DO} & \mathbf{1} \end{bmatrix} \tag{4.59}$$

with $\mathbf{D}_{CO} \equiv \mathrm{CPM}\,(\mathbf{d}_{CO})$, and $\mathbf{D}_{DO} \equiv \mathrm{CPM}\,(\mathbf{d}_{DO})$, while $\mathbf{d}_{CO}$ and $\mathbf{d}_{DO}$ denote vectors pointing from point C to O and D to O, respectively.

Consequently, the stiffness of the limb is obtained as:

$$\mathbf{K}_1 = \mathbf{C}_1^{-1} \tag{4.60}$$

Stiffness Matrix of the SBA

As shown in Fig. 4.3, the three limbs are combined in a parallel chain, their reference point O coinciding with the proof-mass centre of mass. The stiffness matrices of the other two limbs in the global frame $Oxyz$ are obtained following the same procedure as per the first limb. According to eq. (4.49), the 6×6 global stiffness matrix of the SBA is obtained as

$$\mathbf{K}_{\mathrm{sys}} = \sum_{i=1}^{3} \mathbf{K}_i \tag{4.61}$$

i.e.,

$$\mathbf{K}_{\mathrm{sys}} = \begin{bmatrix} \mathbf{K}_{rr} & \mathbf{K}_{rt} \\ \mathbf{K}_{rt}^T & \mathbf{K}_{tt} \end{bmatrix} \tag{4.62}$$

with the various blocks displayed below:

$$\mathbf{K}_{rr} = \begin{bmatrix} 0.1577 & 0 & 0 \\ 0 & 0.1577 & 0 \\ 0 & 0 & 0.2961 \end{bmatrix} \times 10^{-4}\ \mathrm{Nm}, \quad \mathbf{K}_{rt} = \begin{bmatrix} 0 & 0 & 0 \\ 0 & 0 & 1.000 \\ 1.000 & 0 & 0 \end{bmatrix} \times 10^{-6}\ \mathrm{N},$$
$$\mathbf{K}_{tt} = \begin{bmatrix} 5.6147 & 0 & 0 \\ 0 & 5.6147 & 0 \\ 0 & 0 & 30.824 \end{bmatrix} \times 10^{3}\ \mathrm{N/m} \tag{4.63}$$

From eq. (4.62), it is observed that the mechanism behaves isotropically in the x- and y-directions. Moreover, both the translational and rotational stiffnesses in the z-direction

are much higher than their counterparts in the x- and y-directions. That is, the structure has a very high out-of-plane stiffness, the in-plane motion being much easier to excite.

Mass Matrix of the SBA

The 6×6 mass matrix for the SBA is expressed as

$$\mathbf{M}_{\text{sys}} = \begin{bmatrix} m\mathbf{1}_{3\times3} & \mathbf{O} \\ \mathbf{O}_{3\times3} & \mathbf{I}_{3\times3} \end{bmatrix} \tag{4.64}$$

where m and $\mathbf{I}_{3\times3}$ are the mass of the proof-mass and its moment-of-inertia matrix.

With reference to Fig. 4.7, the moments of inertia $\mathbf{I}_{\text{I}}$ and $\mathbf{I}_{\text{III}}$ of Parts I and III in limb I are calculated with respect to their own center-of-mass. Two rotation matrices $\mathbf{R}_{\text{I}}$ and $\mathbf{R}_{\text{III}}$ are defined, in order to transform the moment-of-inertia matrix of each part into the coordinate frame $Oxyz$ as

$$\mathbf{I}_{\text{I}}^{R} = \mathbf{R}_{\text{I}}\mathbf{I}_{\text{I}}\mathbf{R}_{\text{I}}^{T}, \quad \mathbf{I}_{\text{III}}^{R} = \mathbf{R}_{\text{III}}\mathbf{I}_{\text{III}}\mathbf{R}_{\text{III}}^{T} \tag{4.65}$$

with $\mathbf{I}_{\text{I}}^{R}$, $\mathbf{I}_{\text{III}}^{R}$ denoting the moment-of-inertia matrices of Parts I and III in the reference frame $Oxyz$. As illustrated in Fig. 4.7, since the axes of the local $O_3x_3y_3z_3$ frame are parallel to those of $Oxyz$, the moment-of-inertia matrix of Part II, $\mathbf{I}_{\text{II}}$, need not be transformed. Denoting the vector directed from O to the centre of mass of Parts I, II and III by $\mathbf{l}_1$, $\mathbf{l}_2$ and $\mathbf{l}_3$, the moment-of-inertia matrices of each part with respect to O is expressed as

$$\mathbf{I}_{\text{I}}^{O} = \mathbf{I}_{\text{I}}^{R} + \mathbf{I}_{\text{I}}^{\text{ad}}, \quad \mathbf{I}_{\text{II}}^{O} = \mathbf{I}_{\text{II}} + \mathbf{I}_{\text{II}}^{\text{ad}}, \quad \mathbf{I}_{\text{III}}^{O} = \mathbf{I}_{\text{III}}^{R} + \mathbf{I}_{\text{III}}^{\text{ad}} \tag{4.66}$$

According to *Steiner's theorem*[3], with $\mathbf{I}_{\text{I}}^{\text{ad}}$, $\mathbf{I}_{\text{II}}^{\text{ad}}$ and $\mathbf{I}_{\text{III}}^{\text{ad}}$ being given by,

$$\begin{aligned} \mathbf{I}_{\text{I}}^{\text{ad}} &= \begin{bmatrix} m_{\text{I}}l_{\text{Ix}}^2 & 0 & 0 \\ 0 & m_{\text{I}}l_{\text{Iy}}^2 & 0 \\ 0 & 0 & m_{\text{I}}l_{\text{Iz}}^2 \end{bmatrix}, \quad \mathbf{I}_{\text{II}}^{\text{ad}} = \begin{bmatrix} m_{\text{II}}l_{\text{IIx}}^2 & 0 & 0 \\ 0 & m_{\text{II}}l_{\text{IIy}}^2 & 0 \\ 0 & 0 & m_{\text{II}}l_{\text{IIz}}^2 \end{bmatrix}, \\ \mathbf{I}_{\text{III}}^{\text{ad}} &= \begin{bmatrix} m_{\text{III}}l_{\text{IIIx}}^2 & 0 & 0 \\ 0 & m_{\text{III}}l_{\text{IIIy}}^2 & 0 \\ 0 & 0 & m_{\text{III}}l_{\text{IIIz}}^2 \end{bmatrix} \end{aligned} \tag{4.67}$$

[3]Steiner's theorem is best known as "the parallel-axis theorem".

in which m_{I}, m_{II}, and $\mathrm{m_{III}}$ are masses of the three parts. Following the same procedure, the moment-of-inertia matrices of Parts I, II and III in the two other limbs are also calculated, with the proof-mass centre of mass O as the reference point. The relatively small mass of the flexure hinges is neglected here.

The inertia matrix of the proof-mass with respect to its centre of mass O is obtained as:

$$\mathbf{I}_{\mathrm{pm}} = \frac{m_{\mathrm{pm}}}{24}\begin{bmatrix} a^2+2w^2 & 0 & 0 \\ 0 & a^2+2w^2 & 0 \\ 0 & 0 & 2a^2 \end{bmatrix} \tag{4.68}$$

where m_{pm} is the mass of the proof-mass. Therefore, the total inertia matrix of the system is:

$$\mathbf{I} = \mathbf{I}_{\mathrm{pm}} + \mathbf{I}_{\mathrm{I}} + \mathbf{I}_{\mathrm{II}} + \mathbf{I}_{\mathrm{III}} \tag{4.69}$$

where $\mathbf{I}_{\mathrm{I}} = \mathbf{I}_{\mathrm{I}}^{O} + \mathbf{I}_{\mathrm{II}}^{O} + \mathbf{I}_{\mathrm{III}}^{O}$, $\mathbf{I}_{\mathrm{II}}$ and $\mathbf{I}_{\mathrm{III}}$ being obtained from eq. (4.66). Assuming that the system mass is m (0.3095×10^{-6} kg), then the inertia matrix $\mathbf{I}$ is calculated as:

$$\mathbf{I} = \begin{bmatrix} 0.4974 & 0 & 0 \\ 0 & 0.4974 & 0 \\ 0 & 0 & 0.6802 \end{bmatrix} \times 10^{-12}\ \mathrm{kgm^2} \tag{4.70}$$

4.4.3 FE Validation

Both the energy and structural approaches are validated via FEA. The FE validation is conducted on the FE model illustrated in Fig. 3.12. 3D 8-node structure brick element SOLID 73 is used to build the model, based on the assumption that the rotational dof of the system are also significant in modal analysis. Taking into account the whole SBA model, the dof of the FEA model may be tens of thousands, thereby leading to extremely time-consuming calculation. The 6×6 stiffness matrix is computed in ANSYS as described below:

1. Apply, successively, a unit force at the proof-mass centre of mass and a unit moment in the corresponding translational and rotational directions. A vector

$$\mathbf{w} = [M_x \quad M_y \quad M_z \quad F_x \quad F_y \quad F_z]^T \tag{4.71}$$

is constructed, which stores the loading wrenches. Six loading cases $\mathbf{w}_i$ are defined, with $\mathbf{w}_i$ having all but its i^{th} entry equal to 0.

2. The FEA for each loading case $\mathbf{w}_i$ is conducted, then the position and orientation of the proof-mass centroid are obtained; the respective "small" translational and angular displacements are stored in the six-dimensional vector $\Delta\mathbf{s}_i$, which is the i^{th} column of the compliance matrix $\mathbf{C}$.

3. For a general load $\mathbf{w}$, $\Delta\mathbf{s}$ is obtained as

$$\Delta\mathbf{s} = \mathbf{C}\mathbf{w} \tag{4.72}$$

4. The 6×6 stiffness matrix is expressed simply as the inverse of $\mathbf{C}$.

Consequently, the stiffness matrix obtained through FEA is

$$\mathbf{K}_{\text{fea}} = \begin{bmatrix} \mathbf{K}_{rr} & \mathbf{K}_{rt} \\ \mathbf{K}_{rt}^T & \mathbf{K}_{tt} \end{bmatrix} \tag{4.73}$$

with

$$\mathbf{K}_{rr} = \begin{bmatrix} 0.1203 & 0.0061 & 0 \\ 0.0061 & 0.1208 & 0 \\ 0 & 0 & 0.2771 \end{bmatrix} \times 10^{-5}\ \text{Nm}, \quad \mathbf{K}_{rt} = \begin{bmatrix} 0 & 0 & 0.0050 \\ 0 & 0 & 0.4064 \\ -0.4430 & 0.0013 & 0 \end{bmatrix} \times 10^{-3}\ \text{N}$$
$$\mathbf{K}_{tt} = \begin{bmatrix} 5.5819 & 0 & 0 \\ 0 & 5.5807 & 0 \\ 0 & 0 & 25.0652 \end{bmatrix} \times 10^{3}\ \text{N/m} \tag{4.74}$$

Regarding both the Lagrangian formulation and the structural analysis, a good agreement is observed between the stiffness matrix derived and its FEA counterpart for the translational dof, with the MAPE, as defined in eq. (3.53), of 19.085% and 8.057%, respectively. For the rotational stiffness, the MAPE is higher for both cases, of 34.9% and 22.83%, respectively.

The reason for the difference between the Lagrangian formulation and the FEA analysis may come from a feature of the former: the potential energy only includes the strain energy

of the flexure hinges, while ANSYS calculates the strain energy of all parts, based upon the large-dof FE model. Another factor to explain the difference lies in that the system potential energy is derived indirectly from the stiffness matrix introduced in Section 3.3, which includes inherent, unavoidable errors. The calculation of the kinetic energy also suffers from computational inaccuracy. For example, the assumption of a direct relationship of the angular velocity of each rigid part with that of the proof-mass is not accurate, because of the deformation of the flexure hinges connecting them. Within the FE model, a reasonably high mesh density is able to calculate the deformation of the flexure hinges, the effects of their deformation on the angular velocity of each rigid part thus being taken into account.

The difference between the structural and the FE analyses comes from the assumption in the former. In the structural analysis, no compliance is assumed for the rigid links. As illustrated in the mode shapes of the SBA in Fig. 3.13, besides the flexure hinges, the rigid links can also deform, i.e., the putative rigid links observe a non-zero compliance in the FE model. The FEM is thus capable of a more accurate stiffness analysis.

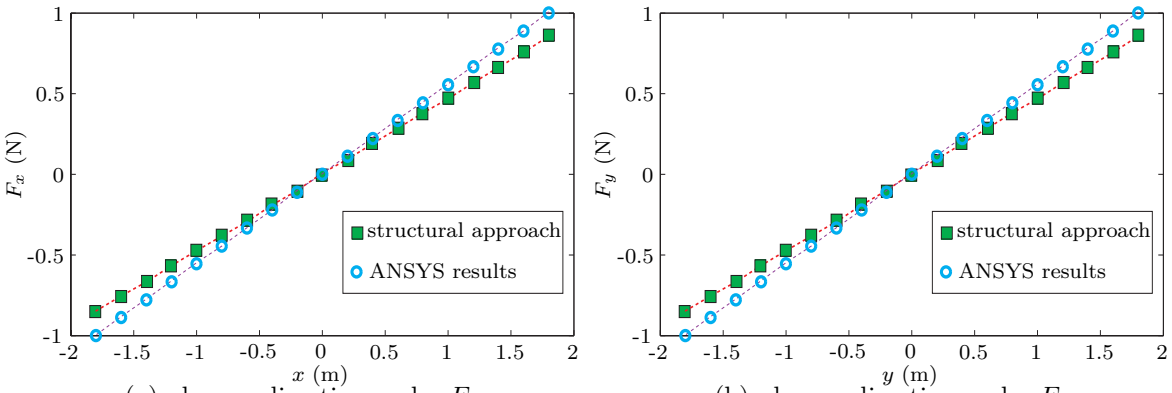

(a) along x direction under F_x (b) along y direction under F_y

Fig. 4.8 Proof-mass centre of mass displacement found through both the structural and the FE analyses

Figure. 4.8 illustrates the displacement of the proof-mass centre of mass under applied loads F_x and F_y, respectively, with the slopes as the stiffness in the corresponding direction. A good agreement between the two approaches is observed, and a negligible nonlinearity appears for the stiffness obtained with ANSYS.

4.4.4 Modal Validation

Based on the stiffness and mass matrices derived by the structural analysis approach, the modal analysis is conducted. Following Angeles [116], the frequency matrix $\mathbf{\Omega}$ is defined as the positive-definite square root of $\mathbf{\Omega}^2 \equiv \mathbf{N}^{-1}\mathbf{K}\mathbf{N}^{-1}$, where $\mathbf{N}$ is the positive-definite square root of $\mathbf{M}_{\text{sys}}$, while $\mathbf{K}_{\text{sys}}$ is the system stiffness matrix.

Let $\{\omega_i\}_1^6$ be the six eigenvalues of $\mathbf{\Omega}$, the six natural frequencies of the system being denoted $\{f_i\}_1^6$, with $f_i = \omega_i/2\pi$ in Hz, which is recorded below in array $\mathbf{f}$ as:

$$\mathbf{f} = \begin{bmatrix} 5616 & 5616 & 9406 & 20632.6 & 20632.6 & 35752.6 \end{bmatrix}^T \text{ Hz} \tag{4.75}$$

The corresponding eigenmodes are stored in the matrix below:

$$\mathbf{V} = \begin{bmatrix} 1.0000 & 0 & 0 & 0 & 0 & 0 \\ 0 & 1.0000 & 0 & 0 & 0 & 0.0942 \\ 0 & 0 & 1.0000 & -0.0075 & 0 & 0 \\ 0 & 0 & 0 & 1.0000 & 0 & 0 \\ 0 & 0 & 0 & 0 & 1.0000 & 0 \\ 0 & 0 & 0 & 0 & 0 & 1.0000 \end{bmatrix} \tag{4.76}$$

Based on the modal-analysis results, we can conclude that the SBA has the same acceleration sensitivity in the x- and y-directions, while along the z-axis the sensitivity is about one-half that of the former. Moreover, pure translation occurs in the Oxy plane, which meets well the SBA design objectives.

With ANSYS, the natural frequencies of the system are directly obtained as:

$$\boldsymbol{\omega}_{\text{fea}} = \begin{bmatrix} 5858.3 & 5859.1 & 12890 & 29006 & 29036 & 33051 \end{bmatrix}^T \text{ Hz} \tag{4.77}$$

With reference to eqs. (4.75) and (4.77), it is concluded that the first two natural frequencies obtained by means of the two approaches are in good agreement. It is noticeable that the difference in the third frequency is somewhat higher (26%) than those of other frequencies (around 9%).

The results are also validated through the first six mode shapes shown in Fig. 3.13. Almost pure translational motions along the x-, y- and z-directions are detected in Figs. 3.13(a)–(c), with slight parasitic motions observed. This behavior tallies with the modal analysis

results displayed in eqs. (4.75) and (4.76). Likewise, the rotations shown in Figs. 3.13(d)–3.13(f) also match the modal analysis results in eq. (4.76).

4.5 Decoupling of the Stiffness Matrix

4.5.1 Decoupling in Compliant Mechanisms

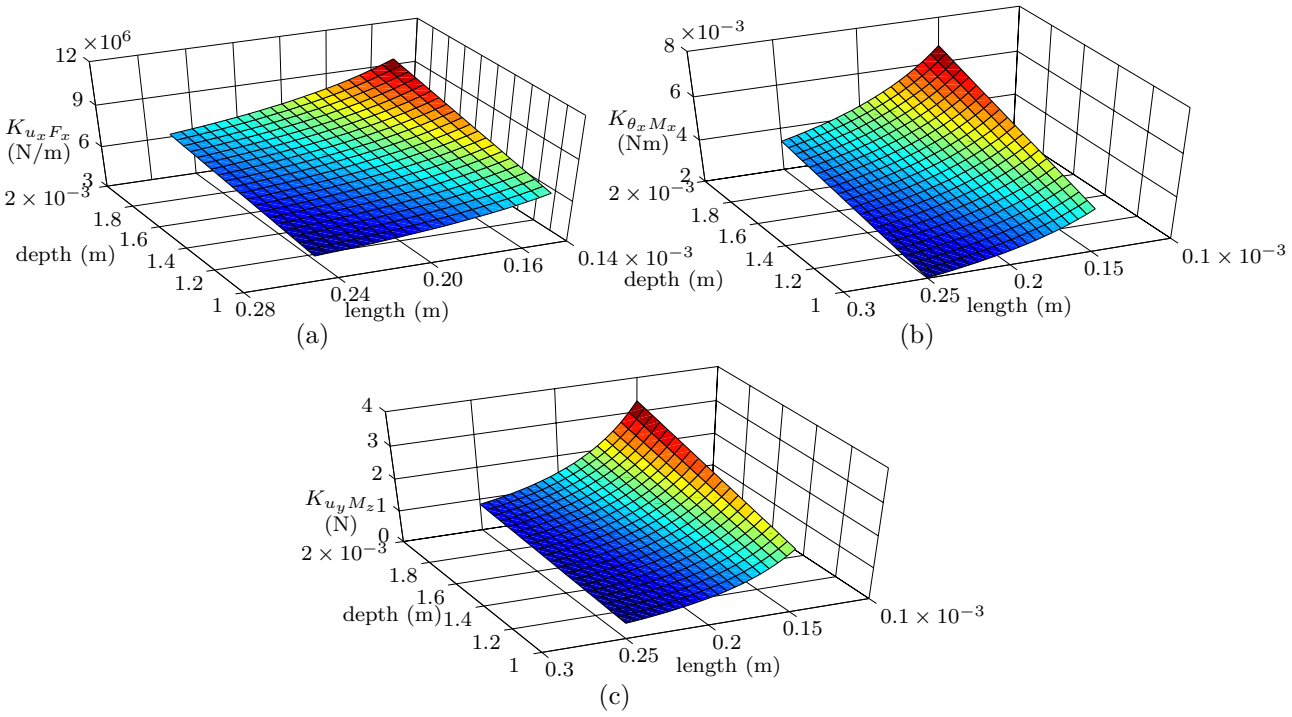

Fig. 4.9 Some stiffness components vs. design parameters: (a) $K_{u_xF_x}$; (b) $K_{\theta_xM_x}$; (c) $K_{u_yM_z}$

The 6×6 compliance matrix $\mathbf{C}_h$ of the Lamé-notched hinge is given in eq. (3.3), the stiffness matrix $\mathbf{K}_h$ of the Lamé-notched hinge being obtained as the inverse of $\mathbf{C}_h$, namely,

$$\mathbf{K}_h = \mathbf{C}_h^{-1} = \begin{bmatrix} \mathbf{K}_{h,tt} & \mathbf{K}_{h,tr} \\ \mathbf{K}_{h,tr}^T & \mathbf{K}_{h,rr} \end{bmatrix} \tag{4.78}$$

with the usual notation for the three different blocks.

Figure 4.9 illustrates the translational stiffness components $K_{u_xF_x}$, rotational component $K_{\theta_xM_x}$ and coupling term $K_{u_yM_z}$ of the Cartesian stiffness matrix of the Lamé-notched

hinge. As shown in the figure, all translational, rotational and coupling components in the Cartesian stiffness matrix behave nonlinearly with respect to the two design parameters and exhibit sensitivity to only one linear combination of the two. Hence, any slight change of a design parameter will have an effect on the stiffness. For this reason, stiffness analysis plays an important role in the whole process of accelerometer design. However, the compliant nature of flexure hinges accompanies a much higher probability of coupling between the translational and the rotational stiffness blocks, in comparison with conventional mechanisms. In accelerometer design, numerous flexure hinges are employed to provide compliant motions; hence, the coupling terms may not be negligible. Therefore, under such situations, the decoupling of the Cartesian stiffness matrix becomes significant in providing a precise stiffness analysis of the whole system.

4.5.2 Decoupling Process

The analysis below is reported in [50]. It is reproduced here for completeness.

Decoupling of the Cartesian stiffness matrix is possible if and only if the 3×3 coupling block $\mathbf{K}_{rt}$ is singular, of rank 2 or 1 [50]. Moreover, decoupling is achieved by means of a similarity transformation that involves only a shift of the origin.

Let the stiffness matrix under study be denoted by $[\mathbf{K}]_{\mathcal{A}}$ when represented in a coordinate frame labeled $\mathcal{A}$. With this matrix representation known, the representation $[\mathbf{K}]_{\mathcal{B}}$ of the same matrix is required in a second frame $\mathcal{B}$, under the assumption that the orientation of the axes of the two frames are different, and so are their origins.

The matrix $\mathbf{S}$ that transforms the components of a unit screw $\hat{\mathbf{s}}$ from $\mathcal{B}$-coordinates into $\mathcal{A}$-coordinates is given by [117]

$$\mathbf{S} = \begin{bmatrix} \mathbf{Q} & \mathbf{O}_{3\times 3} \\ \mathbf{DQ} & \mathbf{Q} \end{bmatrix} \tag{4.79}$$

where $\mathbf{Q}$ and $\mathbf{d}$ denote the rotation matrix and the translation that carries the origin of frame $\mathcal{B}$ into that of $\mathcal{A}$, while $\mathbf{D} \equiv \mathrm{CPM}(\mathbf{d})$.

Matrices $[\mathbf{K}]_{\mathcal{A}}$ and $[\mathbf{K}]_{\mathcal{B}}$ are displayed below:

$$[\mathbf{K}]_{\mathcal{A}} = \begin{bmatrix} \mathbf{K}_{rr} & \mathbf{K}_{rt} \\ \mathbf{K}_{rt}^T & \mathbf{K}_{tt} \end{bmatrix} \quad [\mathbf{K}]_{\mathcal{B}} = \begin{bmatrix} \mathbf{K}'_{rr} & \mathbf{K}'_{rt} \\ \mathbf{K}'^T_{rt} & \mathbf{K}'_{tt} \end{bmatrix} \tag{4.80}$$

The similarity transformation that relates $[\mathbf{K}]_{\mathcal{A}}$ with $[\mathbf{K}]_{\mathcal{B}}$ is known to be [118]:

$$[\mathbf{K}]_{\mathcal{B}} = \mathbf{\Gamma S \Gamma}^{-1}[\mathbf{K}]_{\mathcal{A}}\mathbf{S}^{-1} \tag{4.81}$$

where, in light of eq. (4.4),

$$\mathbf{\Gamma S \Gamma}^{-1} = \mathbf{\Gamma S \Gamma} = \begin{bmatrix} \mathbf{Q} & \mathbf{DQ} \\ \mathbf{O} & \mathbf{Q} \end{bmatrix} \tag{4.82}$$

Substituting eq. (4.80) into eq. (4.81) yields

$$\begin{aligned} \mathbf{K}'_{rr} &= \mathbf{Q}(\mathbf{K}_{rr} - \mathbf{K}_{rt}\mathbf{D})\mathbf{Q}^T + \mathbf{DQ}(\mathbf{K}_{rt}^T - \mathbf{K}_{tt}\mathbf{D})\mathbf{Q}^T \\ \mathbf{K}'_{rt} &= (\mathbf{QK}_{rt} + \mathbf{DQK}_{tt})\mathbf{Q}^T \\ \mathbf{K}'_{tt} &= \mathbf{QK}_{tt}\mathbf{Q}^T \end{aligned} \tag{4.83}$$

Under the decoupling condition $\mathbf{K}'_{rt} = \mathbf{O}$, but no condition is imposed on $\mathbf{Q}$, which can thus be freely chosen, the simplest choice being the 3×3 identity matrix $\mathbf{1}$. If $\mathbf{Q} = \mathbf{1}$, eqs. (4.83) yield,

$$\mathbf{K}'_{rr} = \mathbf{K}_{rr} - \mathbf{K}_{rt}\mathbf{D} + \mathbf{D}(\mathbf{K}_{rt}^T - \mathbf{K}_{tt}\mathbf{D}) \tag{4.84a}$$

$$\mathbf{DK}_{tt} = -\mathbf{K}_{rt} \tag{4.84b}$$

$$\mathbf{K}'_{tt} = \mathbf{K}_{tt} \tag{4.84c}$$

whence $\mathbf{D}$ can be determined from eq. (4.84b). However, $\mathbf{D}$ being a 3×3 skew-symmetric matrix, the product $\mathbf{DK}_{tt}$ is at most of rank 2, according to Sylvester's Theorem [119].

Therefore, the right-hand side of eq. (4.84b) is bound to be of rank 2 or less. If $\mathbf{K}_{rt}$ is of full rank, then decoupling is not possible. Under the assumption that $\mathbf{K}_{rt}$ is singular, then $\mathbf{D}$ is found upon taking the axial vector[4] of both sides of eq. (4.84b), which yields [47]

$$\mathbf{Md} = \mathbf{k}_{rt}, \quad \mathbf{M} = \frac{1}{2}\left[\mathbf{1}\mathrm{tr}\left(\mathbf{K}_{tt}\right) - \mathbf{K}_{tt}\right] \tag{4.85}$$

where $\mathbf{k}_{rt}$ is the axial vector of $\mathbf{K}_{rt}$, $\mathbf{M}$ has units of force, and $\mathrm{tr}(\cdot)$ is the trace of its matrix

[4] Within the concept of field theory [120], the axial vector of a 3×3 matrix $\mathbf{A}$ is defined as $\mathbf{a} \equiv \mathrm{vect}(\mathbf{A}) \equiv (1/2)\left[a_{32} - a_{23} \quad a_{13} - a_{31} \quad a_{21} - a_{12}\right]^T$, a vector invariant of $\mathbf{A}$.

argument.

If $\mathbf{M}$ is invertible, then $\mathbf{d} = \mathbf{M}^{-1}\mathbf{k}_{rt}$; otherwise, one of two cases occurs: a) $\mathrm{tr}(\mathbf{K}_{tt}) = 0$ and b) $\mathbf{K}_{tt}$ is a rank-one matrix. In either case, $\mathbf{M}$ fails to be invertible, but $\mathbf{d}$ can still be calculated, as explained in [50].

4.5.3 Simulation Example of SBA

The decoupling of the stiffness matrix is implemented on the SBA design. Two approaches based on screw theory are employed to find the eigenscrews of the Cartesian stiffness matrix. First, following the decoupling process outlined in Sec. 4.5.2, the stiffness matrix is decoupled and its eigenvalue analysis is conducted upon the decoupled stiffness submatrices. Then, the generalized eigenscrew problem described in Sec. 4.3 is solved for the example, for comparison purposes.

The SBA structure is designed to allow for a two-degree-of-freedom pure translation of the triangular proof-mass in the plane of the figure. At the same time, a complex deformation is detected on the flexure hinges connecting the proof-mass to the frame. However, spurious motions of the proof-mass in the other four directions also occur due to the flexibility of the hinges. In addition, the stiffnesses associated with these motions are much higher than those of the translational motions. The foregoing features will become apparent with the eigenvalue and eigenscrew analyses of the stiffness matrix from eq. (4.74).

Decoupling of the Stiffness Matrix

For the SBA model, it is not difficult to prove that $\mathbf{K}_{rt}$ is of rank 2, decoupling thus being possible, with matrix $\mathbf{M}$ of eq. (4.85) obtained as

$$\mathbf{M}_{\mathrm{SBA}} = \begin{bmatrix} 15.32 & 0 & 0 \\ 0 & 15.32 & 0 \\ 0 & 0 & 5.58 \end{bmatrix} \ \mathrm{N/m} \tag{4.86}$$

which is diagonal, with the first two diagonal entries coinciding to the first four digits. It is not difficult to prove that $\mathbf{M}_{\text{SBA}}$ is invertible, whence $\mathbf{d}$ and $\mathbf{D}$ are obtained as

$$\mathbf{d}_{\text{SBA}} = \begin{bmatrix} 0.13 \\ 0.01 \\ 0 \end{bmatrix} \times 10^{-4}, \quad \mathbf{D}_{\text{SBA}} = \begin{bmatrix} 0 & 0 & 0.01 \\ 0 & 0 & -0.13 \\ -0.01 & 0.13 & 0 \end{bmatrix} \times 10^{-4} \tag{4.87}$$

where both $\mathbf{d}_{\text{SBA}}$ and $\mathbf{D}_{\text{SBA}}$ have units of mm, their entries being five orders of magnitude below the dimensions of the device.

Further, $\mathbf{K}'_{rr}$ and $\mathbf{K}'_{tt}$ are calculated in turn as:

$$\mathbf{K}'_{rr} = \begin{bmatrix} 1.20 & 0.06 & 0 \\ 0.06 & 1.21 & 0 \\ 0 & 0 & 2.77 \end{bmatrix} \times 10^{-2} \text{ Nmm}, \ \mathbf{K}'_{tt} = \begin{bmatrix} 5.58 & 0 & 0 \\ 0 & 5.58 & 0 \\ 0 & 0 & 25.06 \end{bmatrix} \text{ N/mm} \tag{4.88}$$

where $\mathbf{K}'_{rr}$ and $\mathbf{K}'_{tt}$ have units of Nmm and N/mm, respectively. It is noteworthy that both $\mathbf{K}'_{rr}$ and $\mathbf{K}'_{tt}$ show no difference with their counterpart matrices of eq. (4.74), up to the digits displayed.

The corresponding eigenvalues and eigenvectors are arrayed as:

$$\begin{aligned} \mathbf{f}_{rr} &= \begin{bmatrix} 0.01 \\ 0.01 \\ 0.03 \end{bmatrix} \text{ Nmm}, \quad \mathbf{\Lambda}_{rr} = \begin{bmatrix} 0.72 & 0.69 & 0 \\ 0.69 & 0.72 & 0 \\ 0 & 0 & 1.00 \end{bmatrix} \\ \mathbf{f}_{tt} &= \begin{bmatrix} 0.56 \\ 0.56 \\ 2.51 \end{bmatrix} \times 10^3 \text{ N/mm}, \quad \mathbf{\Lambda}_{tt} = \begin{bmatrix} 0.42 & 0.91 & 0 \\ 0.91 & 0.42 & 0 \\ 0 & 0 & 1.00 \end{bmatrix} \end{aligned} \tag{4.89}$$

It is thus found that the SBA exhibits a quasi-isotropic stiffness in the xy-plane. As the out-of-plane translational stiffness is about five times higher than its in-plane counterpart, there is still room for improvement, by means of a dimensional fine-tuning of the current model. Furthermore, tilt motions occur along axes L of Fig. 4.10, which are more likely to happen than the in-plane rotation.

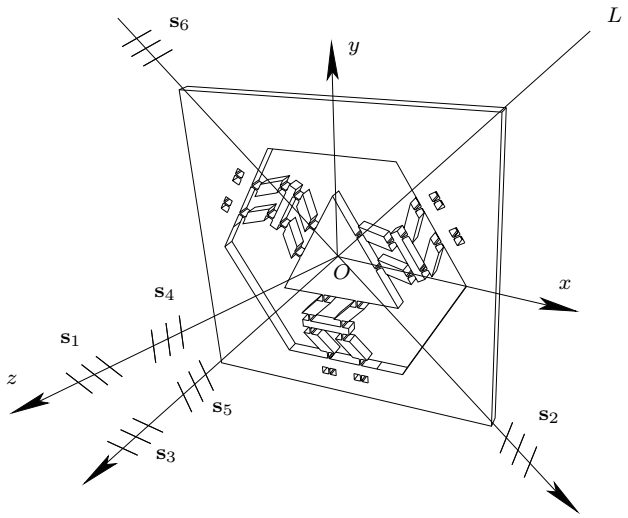

Fig. 4.10 Eigenscrew illustration for SBA

Solution of the Generalized Eigenvalue Problem

In order to solve the generalized eigenvalue problem, the procedure of Sec. 4.3 is applied to the stiffness matrix $\mathbf{K}$ of eq. (4.73). The eigenvalue and the eigenvector arrays $\boldsymbol{\lambda}$ and $\boldsymbol{\Lambda}$, respectively, are displayed below:

$$\boldsymbol{\lambda} = \begin{bmatrix} 0.83 \\ 0.27 \\ 0.25 \\ 0.25 \\ 0.27 \\ 0.83 \end{bmatrix}, \quad \boldsymbol{\Lambda} = \begin{bmatrix} 0.61 & 0.69 & 0.72 & 0.72 & 0.69 & 0.61 \\ 0.12 & 0.72 & 0.69 & 0.69 & 0.72 & 0.12 \\ 0.99 & 0.19 & 0.55 & 0.55 & 0.19 & 0.99 \\ 0.12 & 0.33 & 0.32 & 0.32 & 0.33 & 0.12 \\ 0.18 & 0.34 & 0.31 & 0.31 & 0.34 & 0.18 \\ 0.33 & 0.14 & 0.17 & 0.12 & 0.14 & 0.33 \end{bmatrix} \tag{4.90}$$

The eigenforces were obtained as:

$$\kappa_1 = -\kappa_6 = 0.83 \text{ N}, \ \kappa_2 = -\kappa_5 = 0.26 \text{ N}, \ \kappa_3 = -\kappa_4 = 0.25 \text{ N} \tag{4.91}$$

the corresponding eigenpitches being:

$$p_1 = -p_6 = 0.03 \text{ mm/rad}, \ p_2 = -p_5 = 0.05 \text{ mm/rad}, \ p_3 = -p_4 = 0.04 \text{ mm/rad} \tag{4.92}$$

The six eigenscrews are given below:

$$\mathbf{S} = \begin{bmatrix} 0 & 0.69 & 0.72 & 0.72 & 0.69 & 0 \\ 0 & 0.72 & 0.69 & 0.69 & 0.72 & 0 \\ 0.99 & 0 & 0 & 0 & 0 & 0.99 \\ 0 & 0.03 & 0.03 & 0.03 & 0.03 & 0 \\ 0 & 0.03 & 0.03 & 0.03 & 0.03 & 0 \\ 0.03 & 0 & 0 & 0 & 0 & 0.03 \end{bmatrix} \tag{4.93}$$

whose elements are dimensionless. Notice that the three eigenscrew axes of Fig. 4.10 bear dashes of opposite inclinations, indicating pitches of opposite hands.

All screw axes are found to pass through the centre of mass O of the proof-mass. As per the numerical results in eq. (4.93), four screw axes—the second, third, fourth and fifth columns in $\mathbf{S}$—lie in the x-y plane, the remaining two on the z-axis, which is in good agreement with the symmetric layout of the structure. However, none of the eigenpitches displayed in eq. (4.92) vanishes, and none is unbounded, thereby ruling out both pure rotations and pure translations. Therefore, the finite and nonzero eigenpitches denote spurious scew motions, which tallies with the eigenvectors listed in eq. (4.89). The six eigenscrews, namely, the columns of $\mathbf{S}$ of eq. (4.93), are displayed in the 3D layout of the SBA in Fig. 4.10. Likewise, $\mathbf{s}_1$, $\mathbf{s}_2$, $\mathbf{s}_3$ point in the positive directions of the corresponding axes, while $\mathbf{s}_4$, $\mathbf{s}_5$, $\mathbf{s}_6$ point in the negative directions.

It is noteworthy that slight errors are detected from the comparison of the decoupled stiffness submatrices with their coupled counterparts. Considering that the stiffness matrix is obtained by means of FEA, discretization errors are deemed to be the source of the spurious results, which is reflected in the coupling submatrix. The FEA error thus needs to be filtered for design purposes. Hence, when submatrix $\mathbf{K}_{rt}$ is rank-deficient, decoupling is achievable by means of a "small" shift of the origin. Thus, the discretization error is filtered by means of decoupling. After that, the translational and rotational stiffness properties can be obtained independently via a simple eigenvalue problem, associated with two 3×3 symmetric, positive-definite matrices.

4.6 Summary

This chapter focused on the stiffness analysis of the SBA. Two approaches, named Lagrangian formulation and structural analysis, were adopted and enhanced to obtain the stiffness and mass matrices of the SBA. The numerical results were compared with those obtained by FEA in ANSYS; they showed a reasonable agreement consistently with the ANSYS results. It was shown that stiffness-decoupling led to a straightforward analysis of the compliant mechanism with an enhanced accuracy.

The second topic of this chapter is the decoupling of the Cartesian stiffness matrix and its application to the design of accelerometers designed with a compliant-mechanism structure. Based on eigenscrew theory, the Cartesian stiffness matrix is decoupled and the stiffness submatrices $\mathbf{K}'_{tt}$, $\mathbf{K}'_{rr}$ are compared with their counterparts $\mathbf{K}_{tt}$, $\mathbf{K}_{rr}$ before decoupling. Consequently, for the SBA, $\mathbf{K}'_{tt}$ and $\mathbf{K}'_{rr}$ are numerically almost identical to $\mathbf{K}_{tt}$ and $\mathbf{K}_{rr}$, respectively. The discretization error inherent to FEA is deemed to be the source of the spurious results, which is reflected in the nonzero coupling submatrix. Upon zeroing of this submatrix, the independent translational and rotational stiffness analyses are possible. Thereafter, the eigenvalue analysis is conducted on the decoupled stiffness submatrices. For validation purposes, the eigenscrews are also computed, based on a generalized eigenvalue analysis. The real, symmetric pairs of eigenvalues yield the corresponding eigenpitches for both cases, while the corresponding eigenvectors help explain the motions of the proof-mass.

Chapter 5

MEMS Fabrication

5.1 Overview

This chapter focuses on the MEMS fabrication of the SBA designed and analyzed in the foregoing chapters. The MEMS fabrication is conducted at McGill Nanotools Microfab[1]. The objective of the MEMS fabrication is to validate the manufacturability of our SBA design, with the purpose of conducting, at a later stage, experimental tests.

5.2 Microfabrication

5.2.1 Process Flow

As illustrated in Fig. 5.1, the entire process flow starts from the ⟨100⟩-oriented 4-inch single crystal silicon wafer, with a thickness of 300 μ m. The process flow involves five steps: alignment marks etch; diffusion of resistors; diffusion of conducting region; metallization; and structure etch, with masks 1–5 in Fig. 5.2. In Step 2, the piezoresisitors can be located either on the sidewall, or the top of the flexure hinges. The sidewall resistors are commonly realized by means of ion implantation technique [121, 122, 123]. However, the high cost and the lack of ion implantation equipment force us to turn to the top resistor realization: ion diffusion.

The specifications of the substrate are listed in Table 5.1. It is noteworthy that the

[1]McGill Nanotools Microfab, McGill Institute for Advanced Materials, Ernest Rutherford Building, 3600 University St. Montreal, Quebec, H3A 2T8, Canada.

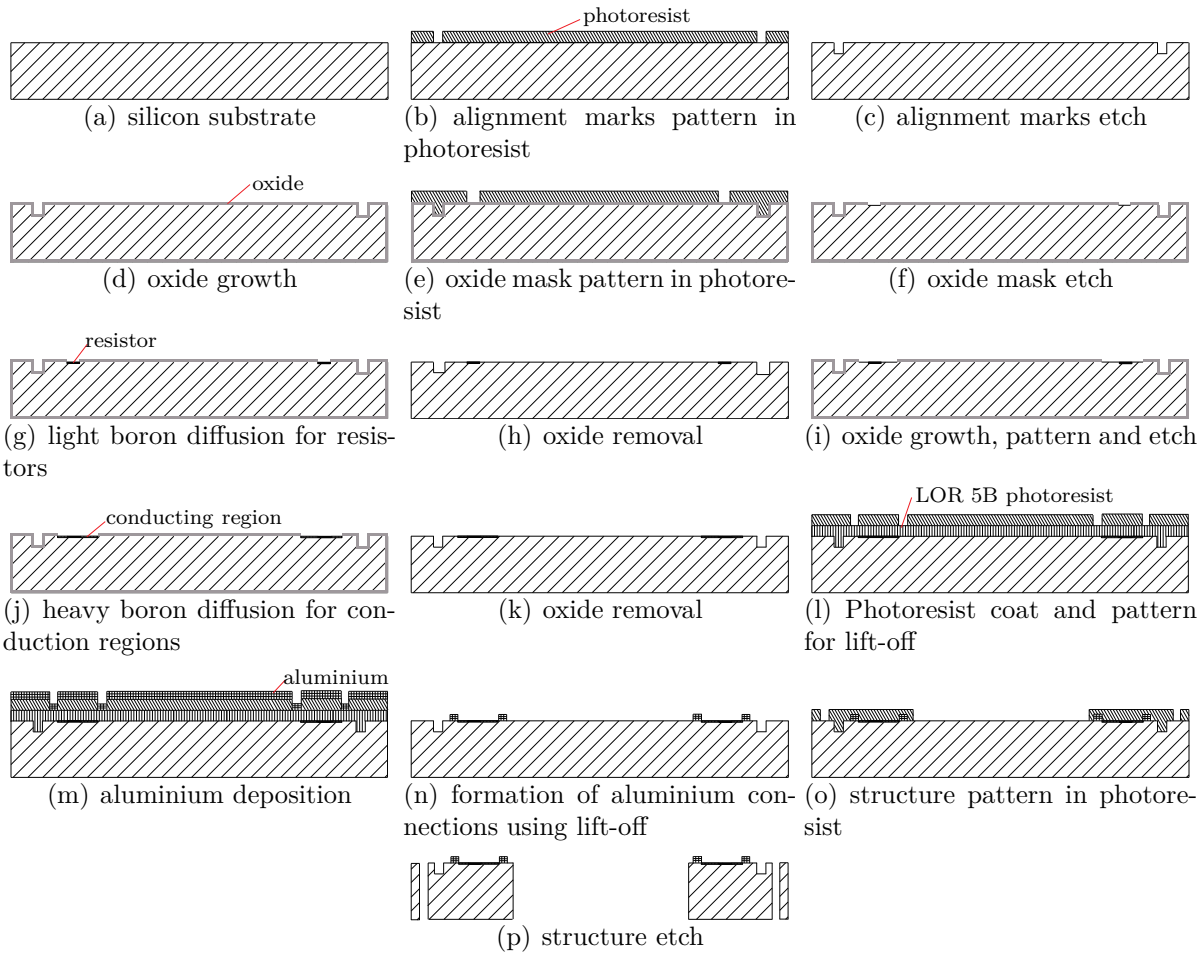

(a) silicon substrate (b) alignment marks pattern in photoresist (c) alignment marks etch

(d) oxide growth (e) oxide mask pattern in photoresist (f) oxide mask etch

(g) light boron diffusion for resistors (h) oxide removal (i) oxide growth, pattern and etch

(j) heavy boron diffusion for conduction regions (k) oxide removal (l) Photoresist coat and pattern for lift-off

(m) aluminium deposition (n) formation of aluminium connections using lift-off (o) structure pattern in photoresist

(p) structure etch

Fig. 5.1 SBA fabrication process flow: (a)–(c) alignment marks etch; (d)–(h) diffusion of resistors; (i)–(k) diffusion of conducting region; (l)–(n) metallization; and (o)–(p) structure etch

silicon substrate is chosen as phosphorus doped n-type, which is intended to meet the requirement for forming a p-n junction during the boron diffusion steps.

Table 5.1 Wafer specifications

material	single-crystal silicon
diameter	4 inch (100 mm)
type and doping	Phosphorus (N)
orientation	100
resistivity	0.5-20 Ω cm
thickness	300 μm
polish	double side polished

5.2.2 Microfabrication Process

Alignment Marks

The wafer is coated with a 1.4-μm layer of Shipley-1813 photoresist and softbaked following the recipe of Table B.1. The pattern on mask 1 in Fig. 5.2 is transferred to the wafer using EVG620 aligner with the recipe listed in Table B.2. Then, the wafer is processed for development and hardbake in terms of the recipe of Table B.3. After the lithography process, the patterned alignment marks are etched down to 4 μm on the silicon substrate using the Deep Reactive Ion Etching (DRIE) process in Table B.5. Finally, an image of the etched alignment mark on the wafer surface after DRIE is captured under microscope, as shown in Fig. 5.3(a). As an example, a microphotograph of alignment for a pair of marks in the resistor diffusion step is illustrated in Fig. 5.3(b). For preparing the wafer for the next step, a standard wafer clean procedure is conducted on the solvent bench to remove the photoresist mask, with relevant parameters listed in Table B.4.

Diffusion of Resistors and Conduction Regions

In order to remove any possible metallic impurities, a special cleaning procedure is conducted prior to the diffusion step. The wafer is soaked in hot H_2SO_4 and H_2O with a 4 : 1 volume ratio, then rinsed by distilled (DI) water, and soaked in 48% hydrofluoric (HF) acid. Unlike ion implantation, ion diffusion is a process under high temperature, which the photoresist mask could not sustain. Hence, silicon dioxide (SiO_2) is selected as the diffusion

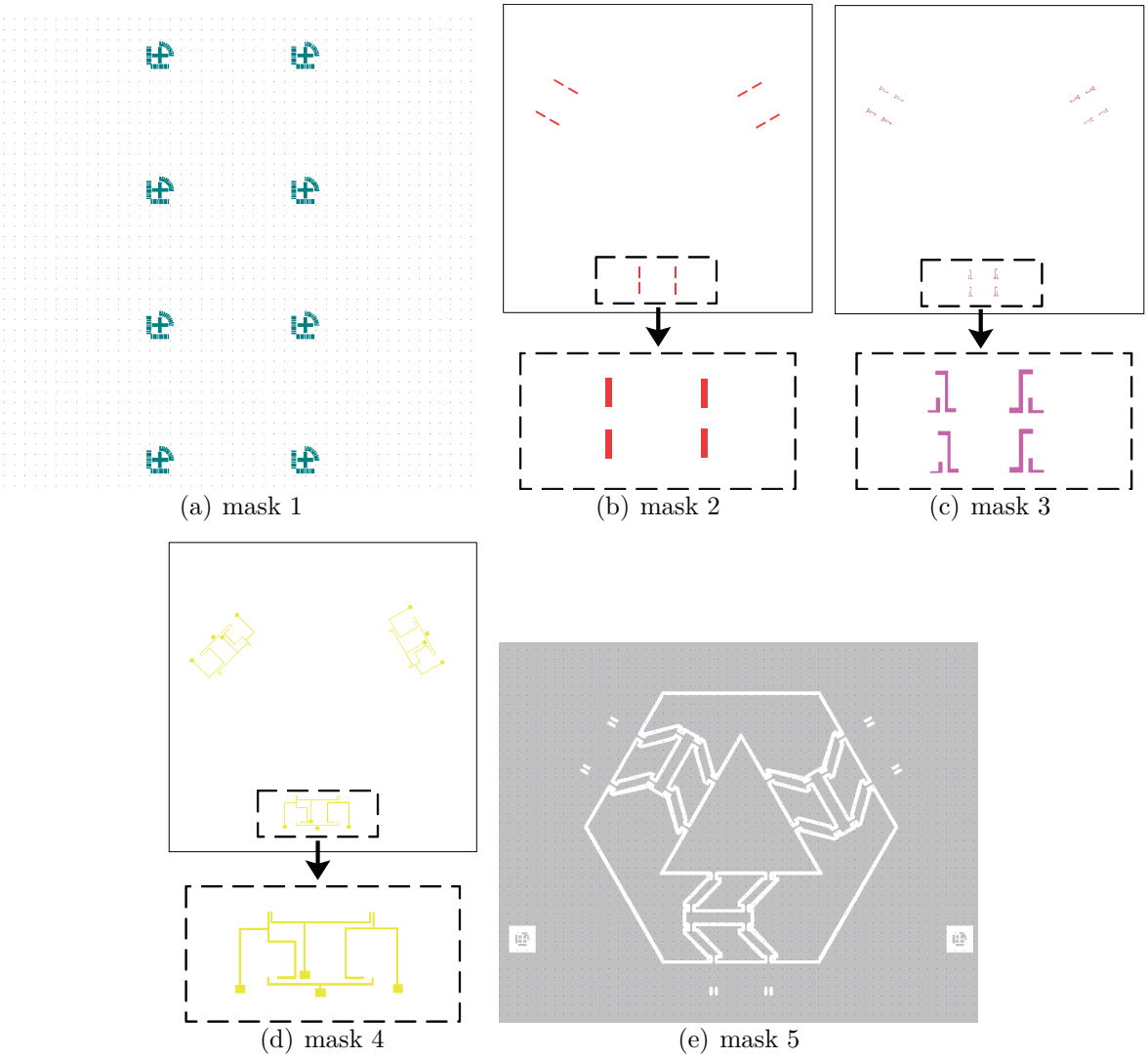

(a) mask 1 (b) mask 2 (c) mask 3

(d) mask 4 (e) mask 5

Fig. 5.2 Masks of the SBA

mask. A 5000-Å layer of silicon dioxide is grown at 1100 °C over the wafer in the Tylan oxidation furnace as per the recipe in Table B.6. Then, a 1.4-μm layer of Shipley-1813 photoresist coated on the oxide layer is patterned in terms of mask 2, as per the recipes of Tables B.1, B.2 and B.3. Afterwards, the oxide mask is etched down to 0.55 μm following the recipe in Table B.7, to form an opening for the subsequent diffusion step. The diffusion process comprises four steps:

1. Preparation of boron diffusion: the wafer is soaked in hot H_2SO_4 and H_2O with a

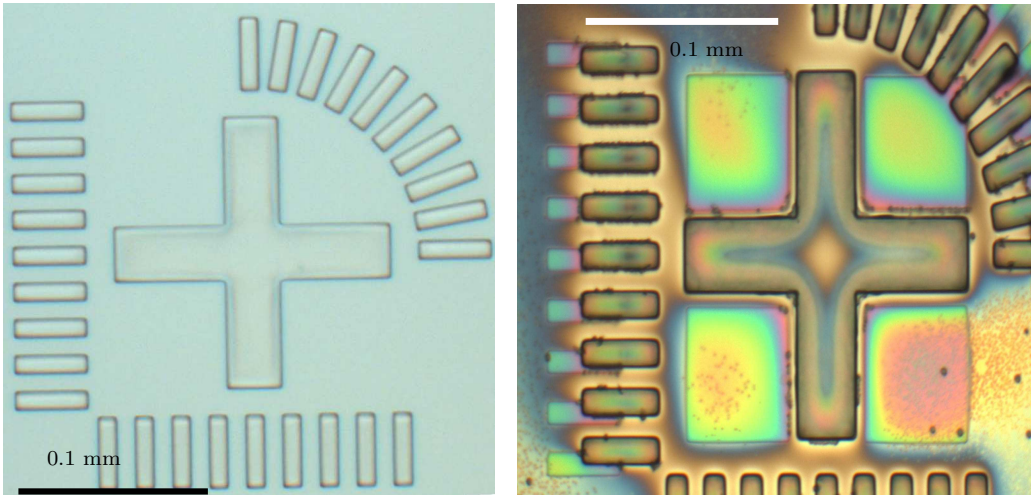

(a) (b)

Fig. 5.3 Microphotographs of: (a) an etched alignment mark; (b) a mark alignment for resistor diffusion step

volume ratio 4 : 1, then rinsed by DI water, and soaked in 48% HF acid, in order to remove any possible metallic impurities.

2. Pre-deposition diffusion process: the boron dopant is spinned on wafer at 3000 rpm for 10 seconds and baked at 150 °C for 10 minutes. It is noteworthy that the objective of the baking process is to harden the spinned Boron film.

3. Drive-in diffusion process: conducted in a Tylan LPCVD furnace at 1000 °C for 60 minutes, under an atmosphere of 75% nitrogen, 25% oxygen, with an approximate sheet resistance[2] of 188 Ω/□.

4. Post diffusion cleanup: the wafer is soaked in 48% HF acid to remove the remaining boron stains and oxide.

Thereafter comes the post-diffusion cleanup step, in which the wafer is soaked in 48% HF acid to remove the remaining boron stains and oxide.

The diffusion of the conducting region can be accomplished following the above procedure, except for the temperature (1100 °C) and duration (120 minutes) in the drive-in step, which forms a sheet resistance of around 16 Ω/□.

[2]To avoid confusion between sheet resistance and bulk resistance, the unit "ohms per square"—denoted Ω/□—is exclusively used for the former.

Metallization

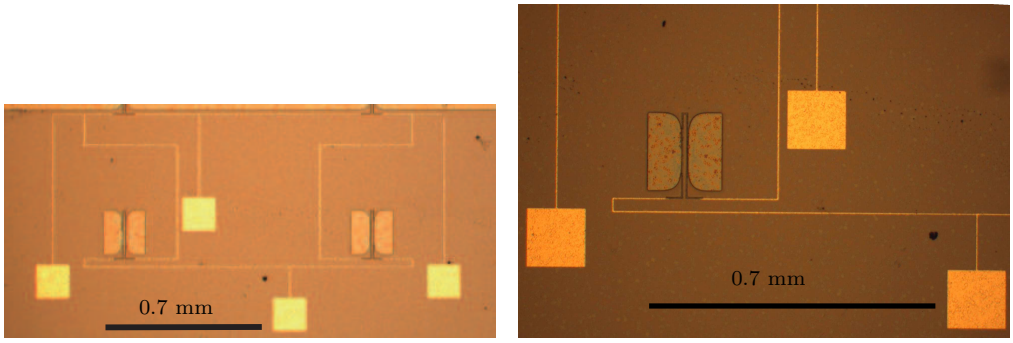

(a) (b)

Fig. 5.4 Microphotographs of: (a) overview of measurement circuit located on the top surface ; and (b) zoom-in

Mask 4 shown in Fig. 5.2 is devised to delineate areas on the wafer that form the circuit interconnects and contact pads. In accordance with the pattern shown on that mask, a technique defining the aluminium connections is adopted: lift-off [124]. In order to ensure a better lift-off effect, an improved process called *LOR 5B lift-off* is employed, during which the lift-off resist (LOR 5B) serves as an underlying layer to create an undercut. In combination with evaporation techniques, the undercut will bring a discontinuity in the deposited aluminium layer which permits optimum lift-off in the adequate solvent.

A regular solvent clean process as described in Table B.4 is implemented as the first step, for the purpose of preparing a better surface quality for processing. Then, the LOR 5B and Shipley-1813 photoresist are coated and soft-baked successively by means of the Site Service Spin Coater. Afterwards, the wafer is processed with exposition and development in terms of mask 4, as per the recipes in Tables B.2 and B.3. It is noteworthy that, unlike the regular lithography process described in the former subsections, the wafer could not be hard-baked here, since it may cause difficulty for peeling off the aluminium in the lift-off. Afterwards, deposition of a 0.2-μm layer of aluminium on the substrate using BJD1800 e-beam evaporator precedes the lift-off step, which follows the recipe of Table B.8. Finally, the substrate is rinsed by nanoremover PG, isopropyl alcohol and distilled water, in succession.

An image of the measurement circuit formed by lift-off is captured via microscope, as shown in Fig. 5.4(a). A zoom-in of the aluminium connections as well as boron-diffused

piezoresistors and conduction region is illustrated in Fig. 5.4(b).

Structure Etch

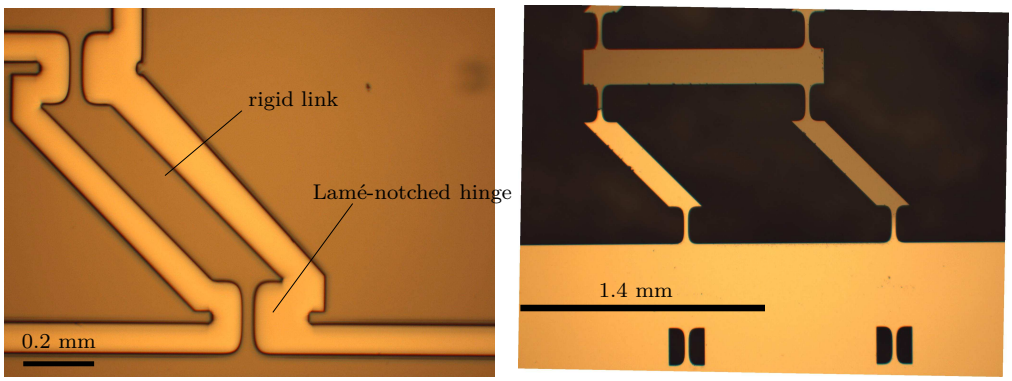

Fig. 5.5 Microphotographs of Lamé-notched hinge: (a) after photolithography; and (b) after etching

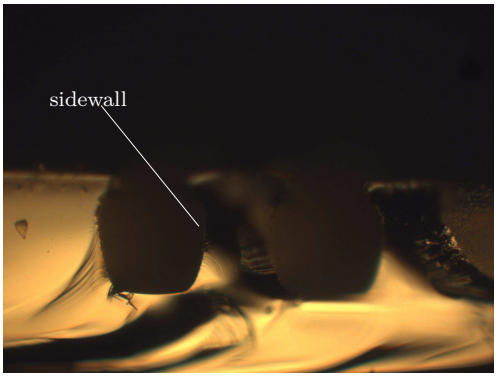

Fig. 5.6 Microphotograph of the overetched trench sidewall after DRIE

The carving of the SBA mechanical structure is conducted using a single DRIE process, which is up to 300-μm deep. It is noteworthy that the 1.4-μm Shipley-1813 photoresist no longer works here, due to the thick etch depth. Instead, the AZ9245 is used as the mask, which is a high-resolution thick photoresist.

The wafer is coated with 10-μm thick AZ9245 photoresist, patterned and developed according to Tables B.2. It is noticeable that the exposure dosage increases to 250 mJ/cm^2 each cycle for four cycles, in conformity with the photoresist thickness increase. After

that, the substrate is hard-baked in the oven for 60 minutes to enhance the adhesion of photoresist with wafer surface, or the photoresist layer may not be capable of sustaining the long-time etching process. After the lithography process, a microphotograph of the Lamé-notched hinge is shown in Fig. 5.5(a), which illustrates that the pattern is fully developed after UV exposure.

The wafers are processed using DRIE, one at a time, with a six-inch carrier wafer underneath, to protect the etching equipment, since a through-substrate etching is required. In order to investigate what recipe is appropriate, a set of etching tests are conducted with varying values of its parameters, i.e., the source power, the gas flow, the temperature, the gas pressure, frequency of the generator, etc. Figure 5.6 depicts the cross sectional view of the substrate trench under the conditions of over-high source power and generator frequency. It can be observed that the trench sidewall is not upright due to an overetching caused by the aggressive recipe. During the tests, it was also found that if the source power is adjusted to 2500 watts or less, the photoresist mask is etched away before the depth of 300 μm could be reached in the silicon, mainly for the reason of extremely long duration. By trial and error, the recipe illustrated in Table B.9 is verified to provide a better effect for through-wafer etching. Finally, zoom-in of the Lamé-notched hinge layouts formed via the DRIE process is shown in Fig. 5.5(b).

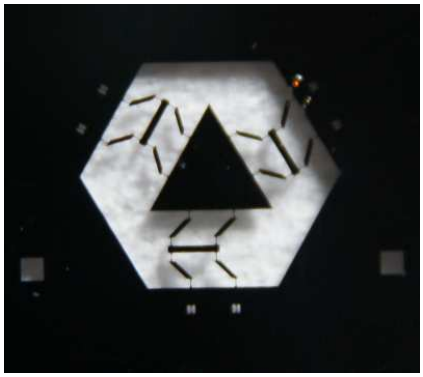

Fig. 5.7 Microphotographs of the SBA

After structural etching, the SBA MEMS model is accomplished, as illustrated in Fig. 5.7.

5.3 Summary

This chapter described the MEMS fabrication process of the SBA. The fabrication was conducted on a 4" crystal silicon, by five masks. Both the mechanical structure and the electronic measurement system were successfully produced. By virtue of its planar nature, the SBA design was proven to be manufacturable. Experiment testing of the SBA MEMS model is the subject of future work.

Chapter 6

Isotropic SBA Strapdowns

6.1 Overview

In this chapter, the idea of a novel tetrahedral strapdown carrying four SBAs is proposed, its applications in estimating rigid body angular velocity and acceleration being investigated. It is noteworthy that, besides angular velocity and acceleration, rigid-body pose-and-twist also includes translational components. However, they are trivial compared with their angular counterparts. Hence, the translational components of rigid-body pose-and-twist are not considered in this analysis. Based on the strapdown layout, an estimation algorithm of the rigid-body angular acceleration, angular velocity and attitude is proposed. In order to validate the strapdown in estimating rigid body pose and twist, two representative simulation examples, a rotating rigid disk and a free-rotating rigid brick, are included. Moreover, for the purpose of showcasing the accuracy of the tetrahedral SBA strapdown, the general-type SBA strapdown with six SBAs is also tested in the simulation examples. For both strapdowns, the estimated pose and twist are compared with their "exact" values, obtained by integration of the rigid-body motion initial-value problem, with the errors recorded. Finally, a summary regarding the accuracy and performance of the SBA tetrahedral strapdown is included.

6.2 The Rigid-body Acceleration Field

A rigid body $\mathcal{B}$, moving in space with n uniaxial accelerometers collocated at n body points $\{P_i\}_1^n$, is illustrated in Fig. 6.1. A reference point B, of position vector $\mathbf{b}$, is chosen

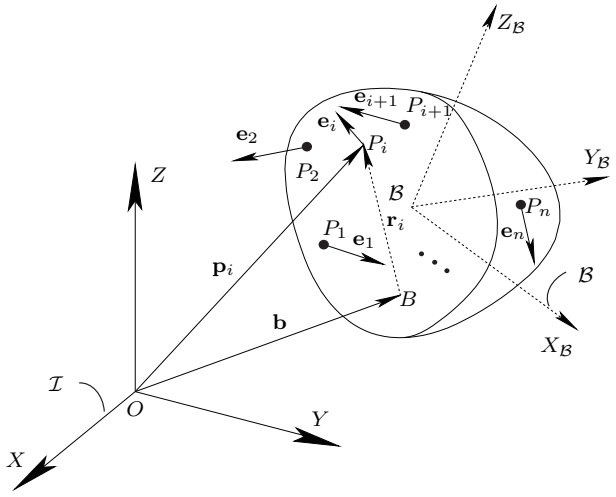

Fig. 6.1 A rigid body carrying n uniaxial accelerometers

on the body. It is noteworthy that B need be neither the centroid nor the centre of mass of the body. The position vector of the i^{th} accelerometer, located at point P_i, is denoted by $\mathbf{p}_i$. Vector $\mathbf{r}_i$ is now introduced as $\mathbf{r}_i = \mathbf{p}_i - \mathbf{b}$, for $i = 1, \ldots, n$.

The physical principle under which accelerometers work is based on the dynamics of the relative motion between the centre of mass C_i of the accelerometer proof-mass and point P_i of the body under probing. The excitation of this motion is the absolute acceleration of point P_i. For conciseness, the dynamics governing the relative motion is not included here, as this is common to all accelerometers [125].

From rigid-body kinematics, the acceleration $\ddot{\mathbf{p}}_i$ of P_i is given by

$$\ddot{\mathbf{p}}_i = \ddot{\mathbf{b}} + \dot{\boldsymbol{\omega}} \times \mathbf{r}_i + \boldsymbol{\omega} \times (\boldsymbol{\omega} \times \mathbf{r}_i) = \ddot{\mathbf{b}} + \mathbf{W}\mathbf{r}_i, \quad i = 1, \ldots, n \tag{6.1}$$

where $\mathbf{W} = \dot{\boldsymbol{\Omega}} + \boldsymbol{\Omega}^2$ is the *angular acceleration matrix*, while $\boldsymbol{\Omega} \equiv \mathrm{CPM}(\boldsymbol{\omega})$.

It is noteworthy that the acceleration field of a rigid body is completely characterized by three vectors: the translational acceleration $\ddot{\mathbf{b}}$ of a landmark or base point B, the angular acceleration $\dot{\boldsymbol{\omega}}$ and the angular velocity $\boldsymbol{\omega}$. Equation (6.1) can be recast in the form:

$$\ddot{\mathbf{p}}_i - \ddot{\mathbf{b}} = \ddot{\mathbf{p}}_i^{\perp} + \ddot{\mathbf{p}}_i^{\parallel} \quad i = 1, \ldots, n \tag{6.2}$$

with the term $\ddot{\mathbf{p}}_i^{\perp} \equiv \dot{\boldsymbol{\Omega}}\mathbf{r}_i$ denoting the tangential point-acceleration component, $\ddot{\mathbf{p}}_i^{\parallel} \equiv \boldsymbol{\Omega}^2\mathbf{r}_i$

its centripetal counterpart[1], respectively, as illustrated in Fig. 6.2.

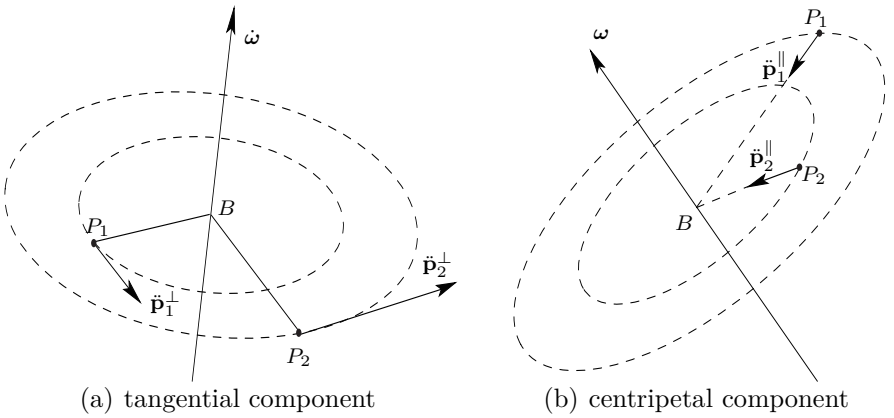

Fig. 6.2 Acceleration field of a rigid body

6.3 SBA Strapdowns

6.3.1 General and Isotropic SBA Strapdowns

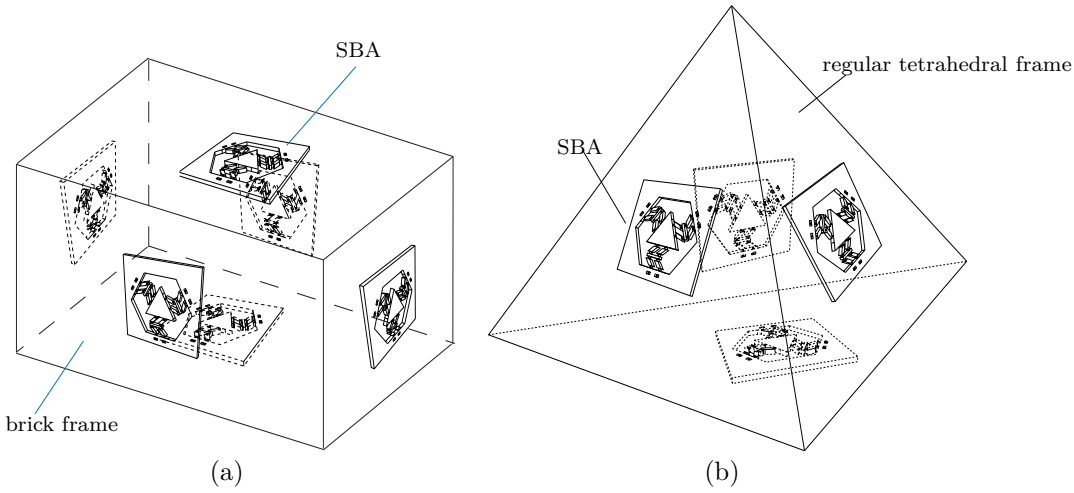

Fig. 6.3 Accelerometer strapdowns: (a) non isotropic; (b) isotropic

One instance of a common strapdown is depicted in Fig. 6.3(a), which comprises six SBAs, one on each face of a brick, i.e., a rectangular parallelepiped. Each SBA is attached

[1]Superscripts $\perp$ and $\parallel$ are to be read "perp" and "par", respectively.

at each face centroid, where the SBA proof-mass centroid is placed. On the other hand, Fig. 6.3(b) illustrates a second instance, *isotropic*[2], that is based on the regular tetrahedron. Moreover, alternative isotropic polyhedral strapdowns, e.g., the other four Platonic solids, the Buckyball[3], and so on, could be used, as they all exhibit the same properties, which will be discussed in Section 6.4.

Let $\{\mathbf{p}_i\}_1^n$ be the corresponding position vectors of the set $\{P_i\}_1^n$, with centroid C, of position vector $\mathbf{c}$, and n denoting the number of SBAs for a general strapdown, namely,

$$\mathbf{c} = \frac{1}{n}\sum_{i=1}^{n}\mathbf{p}_i \tag{6.3}$$

Unlike multi-axial accelerometer strapdowns made of a combination of multiple single-axis accelerometers, the SBA does not have a pair of sensitive directions, by virtue of the *planar isotropy* of the structure. This means that the proof-mass plane includes two principal axes of translational stiffness, at right angles, but otherwise of arbitrary orientations within the plane. Moreover, the two principal stiffnesses in the plane are identical, thereby leading to structural isotropy in the plane. This means that any pair of mutually perpendicular lines passing through P_i, the centroid of the i^{th} face, defines a pair of principal translational-stiffness directions in the face plane.

6.3.2 Angular-acceleration Estimation

When n SBAs move with the rigid-body under probing, each SBA provides one *two-dimensional* acceleration-vector signal in its own plane. It is noteworthy that the i^{th} SBA does not directly and explicitly provide acceleration readouts in the strapdown coordinate system, but rather yields signals associated with the displacement of the proof-mass in its plane; these lead to acceleration signals in the local coordinate frame $\mathcal{F}_i$ of the SBA. For clarity, two other coordinate frames are also introduced, the strapdown-fixed coordinate frame $\mathcal{S}$, and the inertial coordinate system $\mathcal{I}$, the latter illustrated in Fig. 6.1. Apparently, the rotation matrix $\mathbf{R}_i$ from the i^{th} accelerometer frame $\mathcal{F}_i$ to the strapdown-fixed frame $\mathcal{S}$ can be calculated offline, as described in Appendix A. Henceforth, subscripted brackets are

[2]This concept refers to the second moment of the array of vertices of the isotropic polyhedron, a.k.a. the geometric moment-of-inertia tensor, with three identical eigenvalues.

[3]The Buckyball is also known as the 60-vertex truncated icosahedron, whose shape appears in soccer balls.

used to indicate the *representation frame*; when no bracket is included, the representation frame is $\mathcal{I}$, the inertial frame.

From eq. (6.1), the relative acceleration of $\{P_i\}_1^n$ with respect to C can be expressed as

$$\ddot{\mathbf{p}}_i - \ddot{\mathbf{c}} = (\dot{\mathbf{\Omega}} + \mathbf{\Omega}^2)(\mathbf{p}_i - \mathbf{c}), \quad i = 1, \ldots, n \tag{6.4}$$

in the inertial frame $\mathcal{I}$.

Moreover, a $3 \times n$ matrix $\mathbf{\Pi}$ is defined:

$$\mathbf{\Pi} \equiv \begin{bmatrix} \boldsymbol{\pi}_1 & \boldsymbol{\pi}_2 & \ldots & \boldsymbol{\pi}_n \end{bmatrix}, \ \boldsymbol{\pi}_i = \mathbf{p}_i - \mathbf{c}, \ i = 1, \ldots, n \tag{6.5}$$

with similar definitions for $\dot{\mathbf{\Pi}}$ and $\ddot{\mathbf{\Pi}}$.

Based on eqs. (6.4) and (6.5), we have

$$\ddot{\boldsymbol{\pi}}_i \equiv \ddot{\mathbf{p}}_i - \ddot{\mathbf{c}} = (\dot{\mathbf{\Omega}} + \mathbf{\Omega}^2)\boldsymbol{\pi}_i, \quad i = 1, \ldots, n \tag{6.6}$$

Similar to eq. (6.2), $\ddot{\boldsymbol{\pi}}_i$ can be decomposed into two parts: the relative tangential acceleration $\ddot{\boldsymbol{\pi}}_i^{\perp}$ and its centripetal counterpart $\ddot{\boldsymbol{\pi}}_i^{\parallel}$, i.e.,

$$\ddot{\boldsymbol{\pi}}_i^{\perp} = \dot{\mathbf{\Omega}}\boldsymbol{\pi}_i, \quad \ddot{\boldsymbol{\pi}}_i^{\parallel} = \mathbf{\Omega}^2\boldsymbol{\pi}_i, \quad i = 1, \ldots, n \tag{6.7}$$

It is noteworthy that, in the two instances of Fig. 6.3, the position vector $\boldsymbol{\pi}_i$ is perpendicular to the face of the polyhedron containing point P_i. This is an important property, that will be henceforth referred to as the $\boldsymbol{\pi}_i$-**perpendicularity property** (PP). This property holds for all isotropic arrays, but not so for all polyhedral arrays. It does, however, hold for the brick strapdown of Fig. 6.3(a).

It is thus apparent that the tangential component $\ddot{\boldsymbol{\pi}}_i^{\perp}$ lies in the i^{th} face of the polyhedron, which is measured by the SBA attached at point P_i. By virtue of the geometric isotropy of the tetrahedron as well as the elastic, planar isotropy of the SBA, the centripetal acceleration component $\ddot{\boldsymbol{\pi}}_i^{\parallel}$ is filtered out, thereby leaving its tangential counterpart as the accelerometer readout. In this way, the estimation algorithm is greatly simplified, as shown below. For the sake of generality, a n-faced polyhedral strapdown with the PP is assumed henceforth.

The readout of the i^{th} SBA is $\left[\ddot{\boldsymbol{\pi}}_i^{\perp}\right]_{\mathcal{F}_i}$, which is the relative tangential acceleration

expressed in frame $\mathcal{F}_i$. Then, to express this vector in the inertial frame, two coordinate transformations are involved: $\mathbf{R}_i$, to transform the vector from $\mathcal{F}_i$ to $\mathcal{S}$ and $\mathbf{Q}$, the proper orthogonal matrix defining the attitude of the strapdown, which takes vectors represented in $\mathcal{S}$ into their representation in $\mathcal{I}$, namely,

$$\ddot{\boldsymbol{\pi}}_i^{\perp} = \mathbf{Q}\left[\ddot{\boldsymbol{\pi}}_i^{\perp}\right]_{\mathcal{S}}, \quad \left[\ddot{\boldsymbol{\pi}}_i^{\perp}\right]_{\mathcal{S}} = \mathbf{R}_i\left[\ddot{\boldsymbol{\pi}}_i^{\perp}\right]_{\mathcal{F}_i} \tag{6.8}$$

Upon assembling all n equations (6.7), and recalling the definitions of eq. (6.5), the relations below follow:

$$\ddot{\boldsymbol{\Pi}}^{\perp} = \dot{\boldsymbol{\Omega}}\boldsymbol{\Pi}, \quad \ddot{\boldsymbol{\Pi}}^{\perp} = \mathbf{Q}\left[\mathbf{R}_1\left[\ddot{\boldsymbol{\pi}}_1^{\perp}\right]_{\mathcal{F}_1} \quad \mathbf{R}_2\left[\ddot{\boldsymbol{\pi}}_2^{\perp}\right]_{\mathcal{F}_2} \quad \cdots \quad \mathbf{R}_n\left[\ddot{\boldsymbol{\pi}}_n^{\perp}\right]_{\mathcal{F}_n}\right] \tag{6.9}$$

Further, the representation of the array defined in eq. (6.5) in $\mathcal{I}$-coordinates, denoted by $\boldsymbol{\Pi}$, is obtained as

$$\boldsymbol{\Pi} = \mathbf{Q}\left[\boldsymbol{\Pi}\right]_{\mathcal{S}}$$

Post-multiplying both sides of the first of eqs. (6.9) by $\boldsymbol{\Pi}^T$ yields

$$\ddot{\boldsymbol{\Pi}}^{\perp}\boldsymbol{\Pi}^T = \dot{\boldsymbol{\Omega}}\mathbf{R}, \quad \mathbf{R} \equiv \boldsymbol{\Pi}\boldsymbol{\Pi}^T \tag{6.10}$$

Next, the axial vector of both sides of eq. (6.10) is taken, which produces

$$\mathrm{vect}(\ddot{\boldsymbol{\Pi}}^{\perp}\boldsymbol{\Pi}^T) = \frac{1}{2}\mathbf{J}\dot{\boldsymbol{\omega}} \tag{6.11}$$

where $\mathbf{J}$ is a symmetric, positive-definite matrix, given by [1]:

$$\mathbf{J} \equiv \mathrm{tr}(\mathbf{R})\mathbf{1} - \mathbf{R} = \mathbf{Q}\left[\mathbf{J}\right]_{\mathcal{S}}\mathbf{Q}^T \tag{6.12}$$

in which $\mathbf{1}$ denotes the 3×3 identity matrix. In fact, $\mathbf{J}$ can be regarded as the 3×3 inertia matrix of an array of unit masses collocated at $\{P_i\}_1^n$, with respect to C. Notice that $\mathbf{R}$ is body-pose dependent, and hence, $\mathbf{J}$ is also. In body-fixed, i.e., in strapdown-coordinates $\mathcal{S}$, however, the foregoing matrix is constant:

$$\left[\mathbf{J}\right]_{\mathcal{S}} = \mathrm{tr}\left(\left[\mathbf{R}\right]_{\mathcal{S}}\right)\mathbf{1} - \left[\mathbf{R}\right]_{\mathcal{S}}, \; \mathbf{R} = \mathbf{Q}\left[\boldsymbol{\Pi}\right]_{\mathcal{S}}\left[\boldsymbol{\Pi}\right]_{\mathcal{S}}^T\mathbf{Q}^T = \mathbf{Q}\left[\mathbf{R}\right]_{\mathcal{S}}\mathbf{Q}^T \tag{6.13}$$

which means that, for strapdown readouts, $[\mathbf{J}]_{\mathcal{S}}$ must be transformed by means of a similarity transformation to inertial coordinates at every sampling instant.

The angular acceleration for an accelerometer strapdown that is designed, nevertheless, with the PP, is obtained from eq. (6.11) as

$$\dot{\boldsymbol{\omega}} = 2\mathbf{J}^{-1}\text{vect}\left(\ddot{\mathbf{\Pi}}^{\perp}\mathbf{\Pi}^{T}\right) \tag{6.14}$$

or, for $\mathbf{J}$ given in strapdown coordinates, as

$$\dot{\boldsymbol{\omega}} = 2\left(\mathbf{Q}\,[\mathbf{J}]_{\mathcal{S}}\,\mathbf{Q}^{T}\right)^{-1}\text{vect}\left(\mathbf{Q}\left[\ddot{\mathbf{\Pi}}^{\perp}\right]_{\mathcal{S}}[\mathbf{\Pi}]_{\mathcal{S}}^{T}\,\mathbf{Q}^{T}\right) \tag{6.15}$$

For isotropic strapdowns, any isotropic polyhedron with n vertices is now considered. For brevity, only the five Platonic solids and the Buckyball are included here; moreover, the *dual*[4] property of the Platonic solids is applied. For instance, the dual polyhedron of the icosahedron with side a is an inscribed dodecahedron with side $b = (\sqrt{5}-1)a/2$. To calculate $\mathbf{J}$ for the icosahedron, it is obviously more convenient to utilize the vertex coordinates of its dual dodecahedron, instead of finding its own centroid coordinates for each face. Values of $\mathbf{J}$ are recorded for the solids of interest in Table 6.1.

Table 6.1 Expressions for $\mathbf{R}$ and $\mathbf{J}$ pertaining to the Platonic solids and the Buckyball

	Tetrahedron	Cube	Octahedron
$\mathbf{R}$	$\frac{1}{18}a^2\mathbf{1}$	$\frac{1}{2}a^2\mathbf{1}$	$\frac{4}{9}a^2\mathbf{1}$
$\mathbf{J}$	$\frac{1}{9}a^2\mathbf{1}$	$a^2\mathbf{1}$	$\frac{8}{9}a^2\mathbf{1}$
	Dodecahedron	**Icosahedron**	**Buckyball**
$\mathbf{R}$	$(20+8\sqrt{5})a^2\mathbf{1}$	$\frac{10(\sqrt{5}-1)^2(3+\sqrt{5})}{(1+\sqrt{5})^2}a^2\mathbf{1}$	$(\frac{40}{3}+\frac{232}{45}\sqrt{5})a^2\mathbf{1}$
$\mathbf{J}$	$(40+16\sqrt{5})a^2\mathbf{1}$	$\frac{20(\sqrt{5}-1)^2(3+\sqrt{5})}{(1+\sqrt{5})^2}a^2\mathbf{1}$	$(\frac{80}{3}+\frac{464}{45}\sqrt{5})a^2\mathbf{1}$

With reference to Table 6.1, for the Platonic solids, and the Buckyball, $\mathbf{J}$ can be expressed as $\mathbf{J} = \sigma^2\mathbf{1}$, where σ^2 represents a positive scalar factor. Hence, eq. (6.12) becomes

$$\mathbf{J} = \sigma^2\mathbf{Q}\mathbf{1}\mathbf{Q}^{T} = \sigma^2\mathbf{Q}\mathbf{Q}^{T} = \sigma^2\mathbf{1} = [\mathbf{J}]_{\mathcal{S}} \tag{6.16}$$

[4]For any Platonic solid, its dual polyhedron is constructed in such way that each vertex of the latter coincides with the centroid of the corresponding face of the former.

Therefore, for an isotropic accelerometer strapdown, the rotation matrix $\mathbf{Q}$ is filtered out, which leads to $\mathbf{J} = [\mathbf{J}]_{\mathcal{S}}$. Because of the symmetry of the set of vertices of the regular tetrahedron, and hence, of the set $\{P_i\}_1^n$, $[\mathbf{J}]_{\mathcal{S}}$, the second moment of this set, is isotropic because $[\mathbf{R}]_{\mathcal{S}} = (1/18)a^2\mathbf{1}$, with a denoting the length of each tetrahedron edge. Therefore, the $[\mathbf{J}]_{\mathcal{S}}$ matrix remains immutable, i.e., independent of the strapdown attitude, which eases greatly the estimation of the angular acceleration.

Consequently, the angular acceleration is calculated, for an isotropic strapdown, as

$$\dot{\boldsymbol{\omega}} = 2\,[\mathbf{J}]_{\mathcal{S}}^{-1}\,\mathrm{vect}\left(\mathbf{Q}\left[\ddot{\mathbf{\Pi}}^{\perp}\right]_{\mathcal{S}}[\mathbf{\Pi}]_{\mathcal{S}}^{T}\,\mathbf{Q}^{T}\right) = \frac{2}{\sigma^2}\mathbf{Q}\mathrm{vect}\left(\left[\ddot{\mathbf{\Pi}}^{\perp}\right]_{\mathcal{S}}[\mathbf{\Pi}]_{\mathcal{S}}^{T}\right) \tag{6.17}$$

which follows because of the frame-invariance of the axial vector.

By virtue of the identity $\mathrm{vect}\left(\mathbf{a}\mathbf{b}^T\right) \equiv -\,(1/2)\,\mathbf{a}\times\mathbf{b}$ [1], for any 3-dimensional vectors $\mathbf{a}$ and $\mathbf{b}$, the above $\mathrm{vect}\,(\cdot)$ expression can be shown to take the form $\mathrm{vect}\left(\left[\ddot{\mathbf{\Pi}}^{\perp}\right]_{\mathcal{S}}[\mathbf{\Pi}]_{\mathcal{S}}^{T}\right) = \left[\mathbf{P}\ddot{\boldsymbol{\pi}}^{\perp}\right]_{\mathcal{S}}$, where $[\mathbf{P}]_{\mathcal{S}}$ is a row array of $n\,3\times 3$ blocks $[\mathbf{\Pi}_i]_{\mathcal{S}}$ that map any 3-dimensional vector $\mathbf{r}$ into $[\boldsymbol{\pi}_i]_{\mathcal{S}}\times\mathbf{r}$, and $\left[\ddot{\boldsymbol{\pi}}^{\perp}\right]_{\mathcal{S}}$ is a $3n$-dimensional vector, their product, $\left[\mathbf{P}\ddot{\boldsymbol{\pi}}^{\perp}\right]_{\mathcal{S}}$, being rightfully a 3-dimensional vector. Therefore, the above expression for $\dot{\boldsymbol{\omega}}$ takes the form

$$\dot{\boldsymbol{\omega}} = \frac{1}{\sigma^2}\mathbf{Q}\left[\mathbf{P}\ddot{\boldsymbol{\pi}}^{\perp}\right]_{\mathcal{S}} \tag{6.18}$$

and hence, a) $[\mathbf{P}]_{\mathcal{S}}$ being constant, it is to be computed off-line and b) no matrix inversion is needed in this case. Although inverting a 3×3 matrix in real time does not add a significant computational overhead to the foregoing computation, it is still worth avoiding it, in order to avoid roundoff-error amplification that, even if small, may contribute significantly to the buildup of drift in the pose-estimation algorithm. On the other hand, for the non-isotropic stradown, $\mathbf{J}$ depends on $\mathbf{Q}$, as made apparent from eq. (6.12), which must thus be updated at every sampled instant. That is, the updating of $\mathbf{J}$ requires knowledge of the current strapdown attitude, which is given by $\mathbf{Q}$. However, the current attitude is not known, but rather two sampling instants earlier, since the angular velocity is obtained in the previous sampled instant. Therefore, this estimation algorithm is prone to drift. Any drift will hamper the algorithm effectiveness in pose-and-twist estimation.

6.3.3 Angular-velocity Estimation

The estimation of the angular velocity is now straightforward, as it can be derived from the integration of the angular acceleration. A widely used numerical method is Simpson's rule, whereby quadratic polynomials are adopted to approximate the value of a definite integral, namely,

$$\hat{\boldsymbol{\omega}}_{k+1} = \boldsymbol{\omega}_k + \frac{h}{2}(\dot{\boldsymbol{\omega}}_k + \dot{\boldsymbol{\omega}}_{k+1}) \tag{6.19}$$

in which h represents the constant sampling time, and $\hat{\boldsymbol{\omega}}_{k+1}$ denotes the estimate of $\boldsymbol{\omega}_{k+1}$. It is noteworthy that a drift over time is inevitable due to this integration process. Hence, other numerical techniques have to be brought into play, to attenuate the truncation error in the numerical quadrature.

It is recalled that for single-step methods, such as Simpson's rule, only one previous point is used to estimate the successive point. Multi-step methods require information on several prior points, among which central-differences are representative [126]. The central-difference method is a robust numerical tool to integrate ordinary differential equations. In this method, for the k^{th} time step, $\dot{\boldsymbol{\omega}}_k$ can be expressed as

$$\dot{\boldsymbol{\omega}}_k = \frac{1}{2h}\left(-\boldsymbol{\omega}_{k-1} + \boldsymbol{\omega}_{k+1}\right) \tag{6.20}$$

and hence, the angular velocity at the $(k+1)^{\text{st}}$ time step can be obtained in terms of the angular acceleration and angular velocity at previous time steps, namely,

$$\boldsymbol{\omega}_{k+1} = \boldsymbol{\omega}_{k-1} + 2h\dot{\boldsymbol{\omega}}_k \tag{6.21}$$

6.3.4 Rigid-body Attitude

The rigid-body attitude, given by the rotation matrix $\mathbf{Q}$ from a reference attitude, can be expressed using the Euler-Rodrigues parameters—isomorphic to the quaternion— [1], namely, by means of the four-dimensional array $\boldsymbol{\eta}$:

$$\boldsymbol{\eta} = \begin{bmatrix} \mathbf{q} \\ q_0 \end{bmatrix} \equiv \begin{bmatrix} \sin(\phi/2)\,\mathbf{e} \\ \cos(\phi/2) \end{bmatrix} \tag{6.22}$$

in which the rotation $\mathbf{Q}$ is characterized by an axis of direction parallel to the unit vector $\mathbf{e}$, and an angle ϕ about the axis, namely,

$$\mathbf{Q} = \left(q_0^2 - \mathbf{q}^T\mathbf{q}\right)\mathbf{1} + 2\mathbf{q}\mathbf{q}^{\mathrm{T}} + 2q_0\mathrm{CPM}(\mathbf{q}) \tag{6.23}$$

with $\mathbf{1}$ already defined when $\mathbf{J}$ was introduced in eq. (6.12), while the CPM$(\cdot)$ operator was introduced in eq. (4.13).

The linear relationship between the time-rate of change of $\boldsymbol{\eta}$ and $\boldsymbol{\omega}$ is known to be [1]:

$$\dot{\boldsymbol{\eta}} = \mathbf{H}\boldsymbol{\omega} \tag{6.24}$$

with

$$\mathbf{H} = \frac{1}{2}\begin{bmatrix} q_0\mathbf{1} - \mathrm{CPM}(\mathbf{q}) \\ -\mathbf{q}^T \end{bmatrix} \tag{6.25}$$

Substitution of eq. (6.25) into eq. (6.24) leads to

$$\begin{bmatrix} \dot{\mathbf{q}} \\ \dot{q}_0 \end{bmatrix} = \frac{1}{2}\begin{bmatrix} \boldsymbol{\Omega}(t) & \boldsymbol{\omega}(t) \\ -\boldsymbol{\omega}^T(t) & 0 \end{bmatrix}\begin{bmatrix} \mathbf{q} \\ q_0 \end{bmatrix} \tag{6.26}$$

The above equation can be cast in compact form as

$$\dot{\boldsymbol{\eta}} = \mathbf{A}\boldsymbol{\eta}, \quad \mathbf{A} \equiv \frac{1}{2}\begin{bmatrix} \boldsymbol{\Omega}(t) & \boldsymbol{\omega}(t) \\ -\boldsymbol{\omega}^T(t) & 0 \end{bmatrix}, \quad \boldsymbol{\eta}_0 = \begin{bmatrix} \mathbf{0} \\ 1 \end{bmatrix} \tag{6.27}$$

which is an initial-value problem (IVP) in a linear, homogeneous, time-varying equation, that can be integrated numerically using a suite of methods [127]. Since any numerical integration will incur a truncation error, $\boldsymbol{\eta}$ obtained from the foregoing IVP will violate the normality condition $\|\boldsymbol{\eta}\| = 1$. This can be readily alleviated by dividing the computed $\boldsymbol{\eta}$ by its Euclidean norm [128].

Interestingly, matrix $\mathbf{A}$, as given in eq. (6.27), turns out to be isotropic, and hence, optimally conditioned. Its quadruple singular value is, in fact, $\|\mathbf{w}\|/2$.

6.3.5 Introduction of Noise

Because of unavoidable noise, the i^{th} SBA output $\hat{\ddot{\boldsymbol{\pi}}}_i^{\perp}(t)$ is expressed as the sum of three mutually independent vectors, namely,

$$\hat{\ddot{\boldsymbol{\pi}}}_i^{\perp}(t) = \ddot{\boldsymbol{\pi}}_{r,i}^{\perp}(t) + \delta\ddot{\boldsymbol{\pi}}_{b,i}^{\perp}(t) + \delta\ddot{\boldsymbol{\pi}}_{\nu,i}^{\perp}(t) \tag{6.28}$$

where $\ddot{\boldsymbol{\pi}}_{r,i}^{\perp}(t)$ is the actual value of the point-acceleration, whereas $\delta\ddot{\boldsymbol{\pi}}_{b,i}^{\perp}$ and $\delta\ddot{\boldsymbol{\pi}}_{\nu,i}^{\perp}$ are the bias and noise errors, respectively, which are modelled as orthogonal random variables following a Gaussian distribution with zero mean and isotropic variances $\sigma_{b,i}^2\mathbf{1}_{3\times3}$ and $\sigma_{\nu,i}^2\mathbf{1}_{3\times3}$:

$$\begin{bmatrix}\delta\ddot{\boldsymbol{\pi}}_{b,i}^{\perp}\\ \delta\ddot{\boldsymbol{\pi}}_{n,i}^{\perp}\end{bmatrix} \sim \mathcal{N}\left\{\begin{bmatrix}\mathbf{0}_3\\ \mathbf{0}_3\end{bmatrix}, \begin{bmatrix}\sigma_{b,i}^2\mathbf{1}_{3\times3} & \mathbf{O}_{3\times3}\\ \mathbf{O}_{3\times3} & \sigma_{\nu,i}^2\mathbf{1}_{3\times3}\end{bmatrix}\right\} \tag{6.29}$$

Note that the bias error is assumed constant throughout, noise error to be white and normally distributed. Moreover, $\mathbf{0}_n$ denotes the n-dimensional zero vector, $\mathbf{1}_{n\times n}$ the $n\times n$ identity matrix and $\mathbf{O}_{m\times n}$ the $m\times n$ zero matrix.

In an isotropic accelerometer strapdown, the n accelerometer outputs and their corresponding bias and noise errors are grouped in array form as:

$$\begin{aligned}&\hat{\ddot{\boldsymbol{\Pi}}}^{\perp} \equiv \begin{bmatrix}\hat{\ddot{\boldsymbol{\pi}}}_1^{\perp} & \hat{\ddot{\boldsymbol{\pi}}}_2^{\perp} & \dots & \hat{\ddot{\boldsymbol{\pi}}}_n^{\perp}\end{bmatrix}, \quad \ddot{\boldsymbol{\Pi}}^{\perp} \equiv \begin{bmatrix}\ddot{\boldsymbol{\pi}}_{r,1}^{\perp} & \ddot{\boldsymbol{\pi}}_{r,2}^{\perp} & \dots & \ddot{\boldsymbol{\pi}}_{r,n}^{\perp}\end{bmatrix},\\ &\delta\ddot{\boldsymbol{\Pi}}_b^{\perp} \equiv \begin{bmatrix}\delta\ddot{\boldsymbol{\pi}}_{b,1}^{\perp} & \delta\ddot{\boldsymbol{\pi}}_{b,2}^{\perp} & \dots & \delta\ddot{\boldsymbol{\pi}}_{b,n}^{\perp}\end{bmatrix}, \quad \delta\ddot{\boldsymbol{\Pi}}_{\nu}^{\perp} \equiv \begin{bmatrix}\delta\ddot{\boldsymbol{\pi}}_{\nu,1}^{\perp} & \delta\ddot{\boldsymbol{\pi}}_{\nu,2}^{\perp} & \dots & \delta\ddot{\boldsymbol{\pi}}_{\nu,n}^{\perp}\end{bmatrix}\end{aligned} \tag{6.30}$$

Then, eq. (6.28) can be rewritten as

$$\hat{\ddot{\boldsymbol{\Pi}}}^{\perp} = \ddot{\boldsymbol{\Pi}}^{\perp} + \delta\ddot{\boldsymbol{\Pi}}_b^{\perp} + \delta\ddot{\boldsymbol{\Pi}}_{\nu}^{\perp} \tag{6.31}$$

6.3.6 Error Propagation

With reference to eq. (6.18), let $\mathbf{y} = \boldsymbol{\alpha} \equiv \dot{\boldsymbol{\omega}}$, the estimator $\hat{\mathbf{y}}$ of $\mathbf{y}$ being defined as

$$\hat{\mathbf{y}} = \hat{\boldsymbol{\alpha}} = \frac{1}{\sigma^2}\mathbf{Q}\,[\boldsymbol{P}]_{\mathcal{S}}\left[\hat{\ddot{\boldsymbol{\pi}}}^{\perp}\right]_{\mathcal{S}} \tag{6.32}$$

Similar to $\hat{\ddot{\mathbf{\Pi}}}^{\perp}$ in eq. (6.31), $\hat{\mathbf{y}}$ can be decomposed as

$$\hat{\mathbf{y}} = \mathbf{y} + \delta\mathbf{y}_b + \delta\mathbf{y}_\nu \tag{6.33}$$

where $\mathbf{y} \equiv (1/\sigma^2)\mathbf{Q}\,[\boldsymbol{P}]_{\mathcal{S}}\left[\ddot{\boldsymbol{\pi}}^{\perp}\right]_{\mathcal{S}}$, $\delta\mathbf{y}_b \equiv (1/\sigma^2)\mathbf{Q}\,[\boldsymbol{P}]_{\mathcal{S}}\left[\delta\ddot{\boldsymbol{\pi}}_b^{\perp}\right]_{\mathcal{S}}$, and $\delta\mathbf{y}_\nu \equiv (1/\sigma^2)\mathbf{Q}\,[\boldsymbol{P}]_{\mathcal{S}}\left[\delta\ddot{\boldsymbol{\pi}}_\nu^{\perp}\right]_{\mathcal{S}}$.

Besides, $\delta\mathbf{y}_b$ and $\delta\mathbf{y}_\nu$ follow a Gaussian distribution such that

$$\begin{bmatrix}\delta\mathbf{y}_b \\ \delta\mathbf{y}_\nu\end{bmatrix} \sim \mathcal{N}\left\{\mathbf{0}_6, \begin{bmatrix}\mathbf{\Sigma}_{y,b}^2 & \mathbf{O}_{3\times3} \\ \mathbf{O}_{3\times3} & \mathbf{\Sigma}_{y,\nu}^2\end{bmatrix}\right\} \tag{6.34}$$

where

$$\begin{aligned}\mathbf{\Sigma}_{y,b}^2 &\equiv \mathbf{J}^{-1}(\sigma_{b,1}^2\mathbf{\Pi}_1\mathbf{\Pi}_1^T + \sigma_{b,2}^2\mathbf{\Pi}_2\mathbf{\Pi}_2^T + \sigma_{b,3}^2\mathbf{\Pi}_3\mathbf{\Pi}_3^T + \sigma_{b,4}^2\mathbf{\Pi}_4\mathbf{\Pi}_4^T)\mathbf{J}^{-T}, \\ \mathbf{\Sigma}_{y,\nu}^2 &\equiv \mathbf{J}^{-1}(\sigma_{\nu,1}^2\mathbf{\Pi}_1\mathbf{\Pi}_1^T + \sigma_{\nu,2}^2\mathbf{\Pi}_2\mathbf{\Pi}_2^T + \sigma_{\nu,3}^2\mathbf{\Pi}_3\mathbf{\Pi}_3^T + \sigma_{\nu,4}^2\mathbf{\Pi}_4\mathbf{\Pi}_4^T)\mathbf{J}^{-T}\end{aligned} \tag{6.35}$$

with $\mathbf{\Pi}_i$ denoting $\mathrm{CPM}\,(\boldsymbol{\pi}_i)$.

6.3.7 State-space Model

For our proposed estimation scheme, the state space model is formulated as

$$\begin{aligned}\dot{\mathbf{x}} &= \mathbf{F}\mathbf{x} + \mathbf{G}\mathbf{u} \\ \hat{\mathbf{y}} &= \mathbf{h}(\mathbf{x}) + \delta\mathbf{y}_\nu\end{aligned} \tag{6.36}$$

where

$$\mathbf{x} = \begin{bmatrix}\boldsymbol{\alpha}^T & \boldsymbol{\omega}^T & \delta\mathbf{y}_b^T\end{bmatrix}^T, \quad \delta\mathbf{y}_b = \delta\boldsymbol{\alpha}_b, \quad \mathbf{u} = \begin{bmatrix}\boldsymbol{\gamma}^T & \boldsymbol{\beta}_\alpha^T\end{bmatrix}^T,$$
$$\mathbf{F} = \begin{bmatrix}\mathbf{O}_{3\times3} & \mathbf{O}_{3\times6} \\ \mathbf{1}_{3\times3} & \mathbf{O}_{3\times6} \\ \mathbf{O}_{3\times3} & \mathbf{O}_{3\times6}\end{bmatrix}, \quad \mathbf{G} = \begin{bmatrix}\mathbf{1}_{3\times3} & \mathbf{O}_{3\times3} \\ \mathbf{O}_{3\times3} & \mathbf{O}_{3\times3} \\ \mathbf{O}_{3\times3} & \mathbf{1}_{3\times3}\end{bmatrix}, \quad \mathbf{h}(\mathbf{x}) = \boldsymbol{\alpha} + \delta\boldsymbol{\alpha}_b$$

.

Further, notice that, in eq. (6.36), the system inputs $\{\gamma_i\}_1^3$ and $\{\beta_{\alpha,i}\}_1^3$ are the time-rates of change of the angular acceleration—termed *the angular jerk*—and those of the bias errors, respectively.

It is noteworthy that direct measurement of the angular jerk and the time-rates of change of the errors are not produced by an accelerometer strapdown; therefore, they are

modelled as piecewise-constant functions, namely,

$$\mathbf{u}(t) = \begin{cases} \mathbf{u}_0 & t_0 \leq t < t_1, \\ \mathbf{u}_1 & t_1 \leq t < t_2, \\ \vdots & \vdots \\ \mathbf{u}_k & t_k \leq t < t_{k+1}, \\ \vdots & \vdots \end{cases} \qquad \mathbf{u}_k \sim \mathcal{N}\left\{\mathbf{0}_6, \boldsymbol{\Sigma}^2_{\mathbf{u}}\right\}$$

The angular jerk and the time-rates of change of the errors are assumed to be stochastically independent, their covariance matrices thereby taking the form:

$$\boldsymbol{\Sigma}^2_{\mathbf{u}} = \begin{bmatrix} \sigma^2_\gamma \mathbf{1}_{3\times3} & \mathbf{O}_{3\times3} \\ \mathbf{O}_{3\times3} & \boldsymbol{\Sigma}^2_\beta \end{bmatrix}, \quad \boldsymbol{\Sigma}^2_\beta = \sigma^2_\beta \mathbf{Q}\left[\mathbf{P}\right]_{\mathcal{S}}\left[\mathbf{P}\right]^T_{\mathcal{S}}\mathbf{Q}^T \tag{6.37}$$

where $\sigma^2_\gamma \mathbf{1}_{3\times3}$ is the covariance matrix of $\boldsymbol{\gamma}$, $\boldsymbol{\Sigma}^2_\beta$ that of the array defined as

$$\boldsymbol{\beta} = \begin{bmatrix} \boldsymbol{\beta}^T_\alpha & \boldsymbol{\beta}^T_\zeta \end{bmatrix}^T \tag{6.38}$$

The initial state of the estimate $\hat{\mathbf{x}}_0$ for the state-space system of eq. (6.36) is given as

$$\hat{\mathbf{x}}_0 \equiv \begin{bmatrix} \hat{\boldsymbol{\alpha}}_0 \\ \hat{\boldsymbol{\omega}}_0 \\ \delta\hat{\boldsymbol{\alpha}}_b \end{bmatrix} \sim \mathcal{N}\left\{ \begin{bmatrix} \boldsymbol{\alpha}_0 \\ \boldsymbol{\omega}_0 \\ \mathbf{0}_3 \end{bmatrix}, \begin{bmatrix} \sigma^2_{\alpha,0}\mathbf{1}_{3\times3} & \mathbf{O}_{3\times3} & \mathbf{O}_{3\times3} \\ \mathbf{O}_{3\times3} & \sigma^2_{\omega,0}\mathbf{1}_{3\times3} & \mathbf{O}_{3\times3} \\ \mathbf{O}_{3\times3} & \mathbf{O}_{3\times3} & \boldsymbol{\Sigma}^2_{y,\nu} \end{bmatrix} \right\} \tag{6.39}$$

where the initial estimate of the angular acceleration $\hat{\boldsymbol{\alpha}}_0$ and that of the angular velocity $\hat{\boldsymbol{\omega}}_0$ are assumed to be independent, with Gaussian distributions of means $\boldsymbol{\alpha}_0$ and $\boldsymbol{\omega}_0$, respectively, and corresponding isotropic variances $\sigma^2_{\alpha,0}\mathbf{1}_{3\times3}$ and $\sigma^2_{\omega,0}\mathbf{1}_{3\times3}$.

6.3.8 Extended Kalman Filter

For the purpose of feeding the extended Kalman filter with the SBA-strapdown estimation algorithm, the continuous-time state-space system in eq. (6.36) is discretized.

First, the state-transition matrix is introduced here for any time step $t_{k+1} - t_k$:

$$\boldsymbol{\Phi}(t_k, t_{k+1}) = e^{\mathbf{F}(t_{k+1}-t_k)} = \mathbf{1}_{9\times9} + \mathbf{F}(t_{k+1} - t_k)$$

i.e.,

$$\mathbf{\Phi}(t_k, t_{k+1}) = \mathbf{1}_{9\times 9} + \mathbf{F}h \tag{6.40}$$

under the assumption that $\Delta t_{k+1} \equiv t_{k+1} - t_k = h$ is constant.

The system state at time t_{k+1} can thus be expressed as

$$\mathbf{x}_{k+1} = \mathbf{\Phi}\mathbf{x}_k + \mathbf{\Upsilon}\mathbf{u}_k \tag{6.41}$$

where $\mathbf{\Upsilon} = \mathbf{G}h + (1/2)\mathbf{F}\mathbf{G}h^2$.

Further, the discrete-time measurement equation takes a form similar to its continuous-time counterpart of eq. (6.36):

$$\hat{\mathbf{y}}_k = \mathbf{h}(\mathbf{x}_k) + \delta\mathbf{y}_{\nu,k} \tag{6.42}$$

Moreover, the application of the extended Kalman filter requires the Jacobian matrix $\mathbf{H}$ of its time-continuous counterpart, as:

$$\mathbf{H}(\mathbf{x}) = \frac{\partial \mathbf{h}(\mathbf{x})}{\partial \mathbf{x}} = \begin{bmatrix} \mathbf{1}_{3\times 3} & \mathbf{O}_{3\times 3} & \mathbf{O}_{3\times 3} \end{bmatrix} \tag{6.43}$$

The estimation algorithm with Kalman filter is generalized below:

- **Model Forecast Step:**
  $\hat{\mathbf{x}}_k^-$, the a priori state estimate at time t_k, is calculated from $\hat{\mathbf{x}}_{k-1}^+$, the a posteriori state estimate at time t_{k-1}, as:
  $$\hat{\mathbf{x}}_k^- = \mathbf{\Phi}\hat{\mathbf{x}}_{k-1}^+ \tag{6.44}$$
  with covariance given by
  $$\mathbf{V}_k^- = \mathbf{\Phi}\mathbf{V}_{k-1}^+\mathbf{\Phi}^T + \mathbf{\Upsilon}\mathbf{\Sigma}_{\mathbf{u}}^2\mathbf{\Upsilon}^T \tag{6.45}$$

- **Data Assimilation Step:**
  $$\hat{\mathbf{x}}_k^+ = \hat{\mathbf{x}}_k^- + \mathbf{K}_k\left[\hat{\mathbf{y}}_k - \mathbf{h}(\hat{\mathbf{x}}_k^-)\right] \tag{6.46}$$
  where
  $$\mathbf{K}_k \approx \mathbf{V}_k^-\mathbf{H}(\hat{\mathbf{x}}_k^-)^T\left[\mathbf{H}(\hat{\mathbf{x}}_k^-)\mathbf{V}_k^-\mathbf{H}(\hat{\mathbf{x}}_k^-)^T + \mathbf{\Sigma}_{y,\nu}^2\right]^{-1} \tag{6.47}$$
  $$\mathbf{V}_k^+ \approx \left[\mathbf{1}_{9\times 9} - \mathbf{K}_k\mathbf{H}(\hat{\mathbf{x}}_k^-)\right]\mathbf{V}_k^- \tag{6.48}$$

$\mathbf{V}_k^-$ being the covariance of the error on the a priori state estimate $\mathbf{x}_k^-$, $\hat{\mathbf{V}}_k^+$ denoting its a posteriori counterpart $\hat{\mathbf{x}}_k^+$, and $\mathbf{K}_k$ is the Kalman gain.

6.3.9 Signal-to-noise Ratio

Upon denoting the true angular acceleration vector and its noisy counterpart as $\boldsymbol{\alpha}$ and $\hat{\boldsymbol{\alpha}}$, respectively, the error component of α is defined as [5]:

$$\sigma = \frac{\| \boldsymbol{\alpha} \|_2}{\| \delta\boldsymbol{\alpha} \|_2} = \frac{\| \boldsymbol{\alpha} \|_2}{\| \boldsymbol{\alpha} - \hat{\boldsymbol{\alpha}} \|_2} \tag{6.49}$$

where $\| \cdot \|_2$ represents the Euclidean norm of $(\cdot)$.

Based on the error component, the signal-to-noise ratio (SNR) can be obtained as [129]:

$$SNR = 20 \times \log_{10}\sigma \text{ db} \tag{6.50}$$

SNR is an important criterion in analyzing the sensitivity of accelerometer strapdowns. A high obtrusive background noise will result in a low SNR, which means a low strapdown sensitivity.

6.4 Simulation Examples

In order to verify the robustness of the foregoing estimation algorithm, two representative simulation examples are conducted: the harmonic rotation of a rigid disk about three orthogonal axes, and the free rotation of a rigid brick. For each example, a tetrahedral SBA strapdown and a brick SBA strapdown are rigidly attached to the rigid body at an arbitrary point on its surface, one at a time. Three vector variables, angular acceleration $\dot{\boldsymbol{\omega}}$, angular velocity $\boldsymbol{\omega}$ and attitude $\boldsymbol{\eta}$, are to be estimated using corresponding algorithms. The root-mean square (rms) error of the measured pose and twist with their exact counterparts is chosen as the criterion in evaluating the performance of each accelerometer strapdown.

6.4.1 Rotating Disk Under a Prescribed Applied Moment

The case of a harmonically rotating rigid disk is shown in Fig. 6.4, with uniform density $\rho = 7800$ kg/m^3, a radius $r = 0.2$ m and thickness $w = 0.03$ m. A tetrahedral strapdown

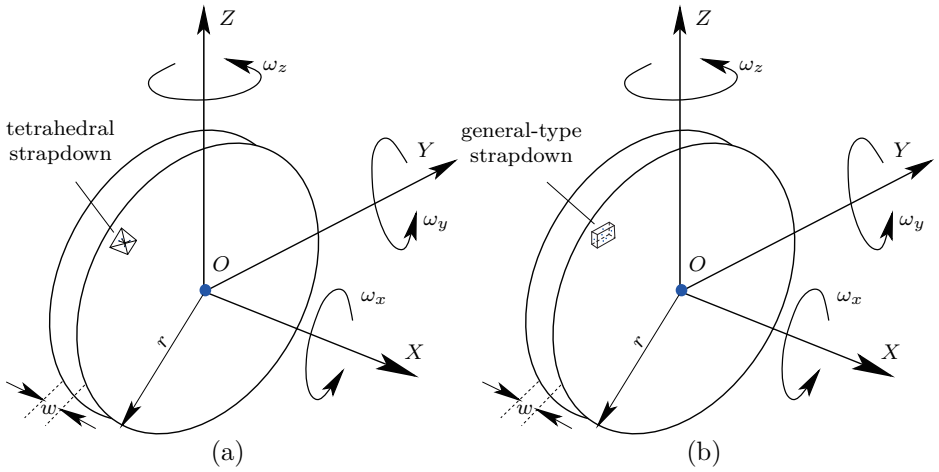

Fig. 6.4 A rigid rotating disk with IMU

is attached with its centroid located at point (0.015, −0.1, 0.1) m in the body-fixed frame shown in the foregoing figure—because of the geometric isotropy of the tetrahedral strapdown, its orientation in the body-fixed frame is immaterial. The disk is excited with a harmonic moment $\mathbf{n}(t)$.

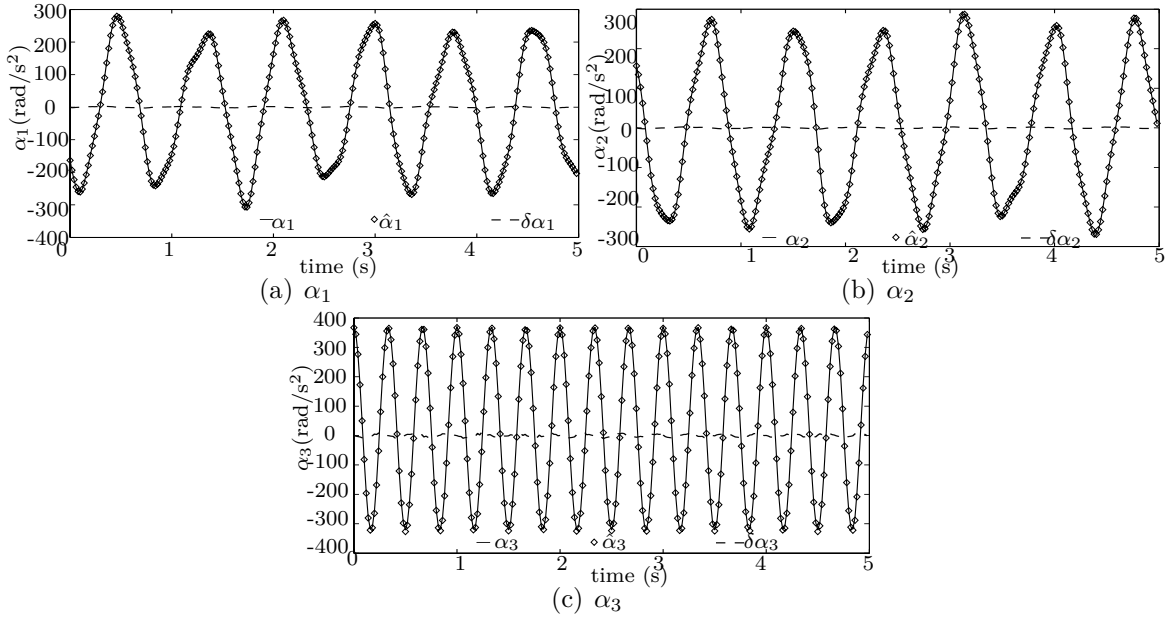

Fig. 6.5 Estimated acceleration of the disk of Fig. 6.4 using a tetrahedral SBA strapdown

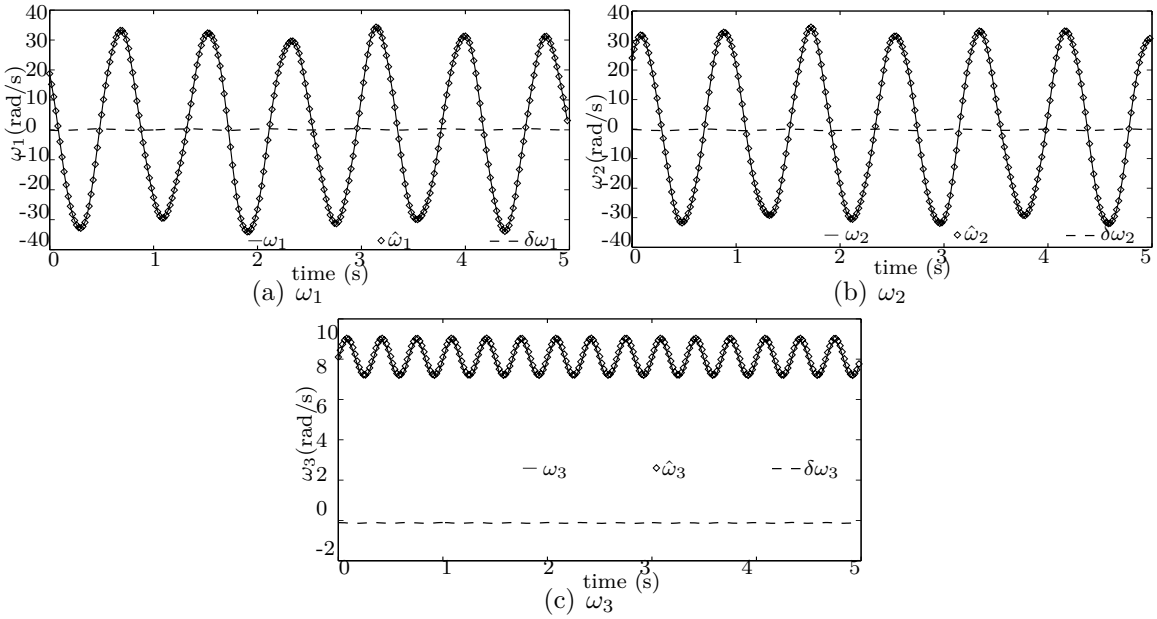

Fig. 6.6 Estimated angular velocity of the disk of Fig. 6.4 using a tetrahedral SBA strapdown

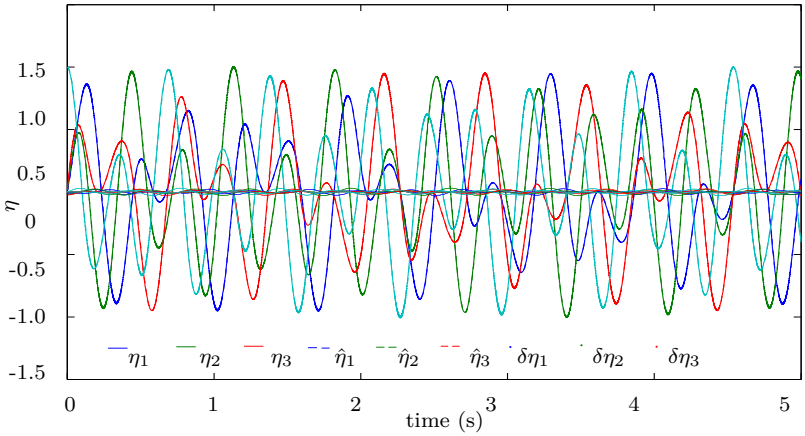

Fig. 6.7 Estimated attitude of the disk of Fig. 6.4 using a tetrahedral SBA strapdown

The equation of motion of the rotating disk is

$$\mathbf{I}\dot{\boldsymbol{\omega}} + \boldsymbol{\omega} \times \mathbf{I}\boldsymbol{\omega} = \mathbf{n}(t),\ \boldsymbol{\omega}(0) = \mathbf{0},\ \mathbf{n}(t) = [30\cos(4\pi t)\ 6\cos(5\pi t)\ 6\cos(6\pi t)]^T\ \mathrm{N\,m} \quad (6.51)$$

$\mathbf{I}$ being the centroidal inertia matrix of the rigid disk, namely, $\mathbf{I} = \rho\pi r^2 w\,\mathrm{diag}[(3r^2 + w^2)/12,\ (3r^2 + w^2)/12,\ r^2/2]\ \mathrm{kg\,m^2}$. The exact angular acceleration $\boldsymbol{\alpha}$ and its estimate $\hat{\boldsymbol{\alpha}}$

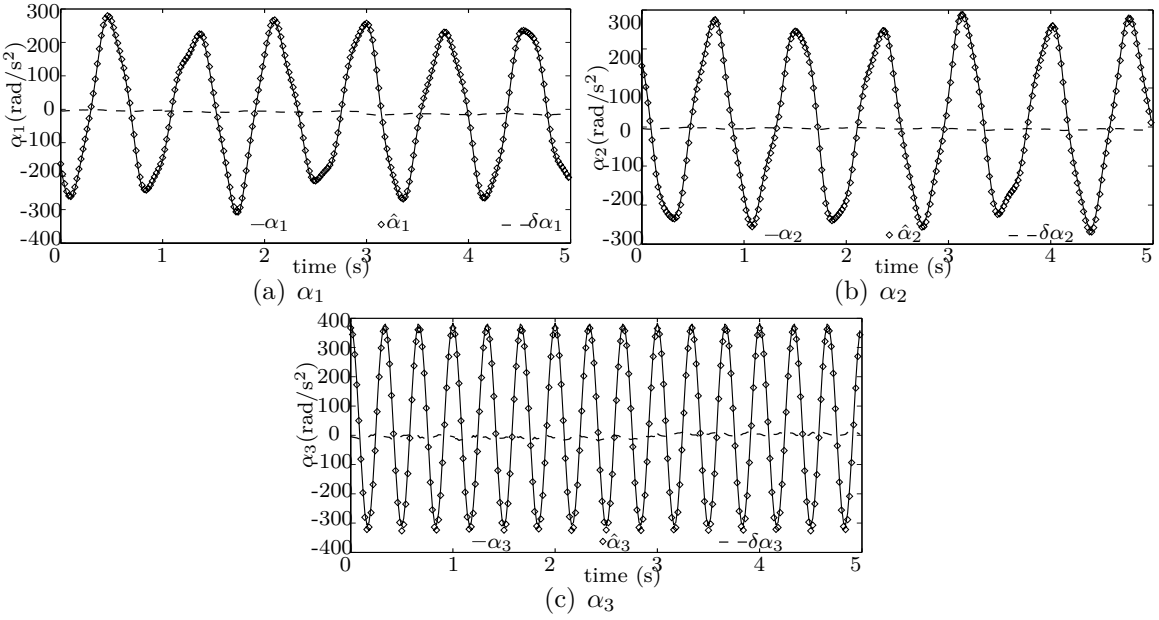

Fig. 6.8 Estimated acceleration of the disk of Fig. 6.4 using a brick SBA strapdown

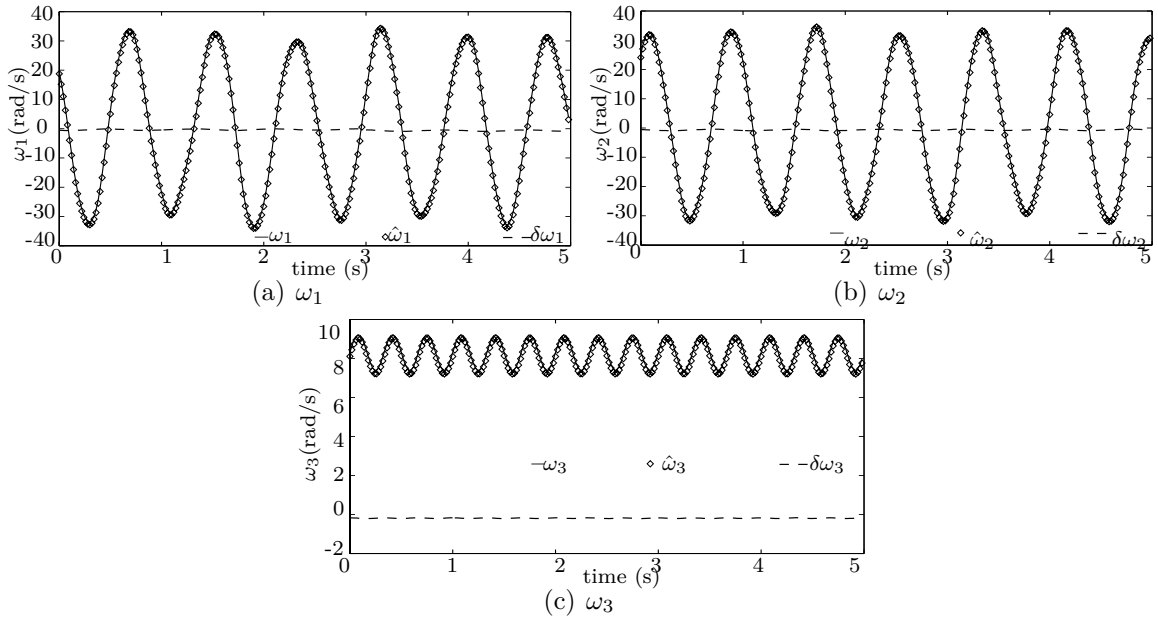

Fig. 6.9 Estimated angular velocity of the disk of Fig. 6.4 using a brick SBA strapdown

are plotted in Fig. 6.5, along with the error $\delta\boldsymbol{\alpha}$. The "exact" value is that obtained from

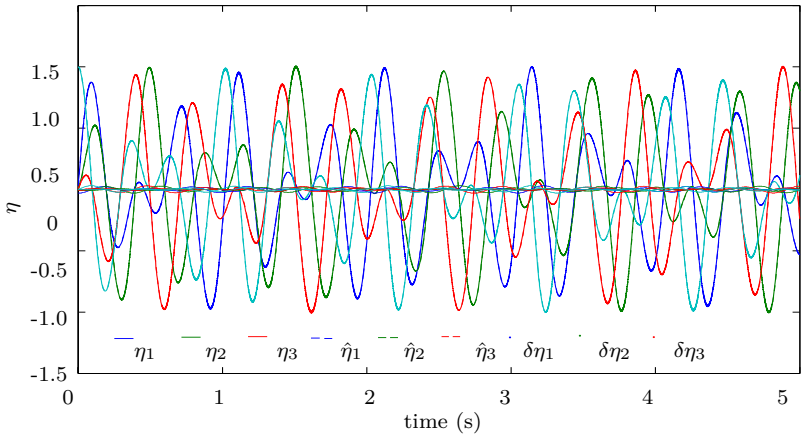

Fig. 6.10 Estimated attitude of the disk of Fig. 6.4 using a brick SBA strapdown

the numerical integration of the initial-value problem in eq. (6.51), "estimated" denoting the value obtained using the proposed estimation algorithm. The "error" is calculated as the numerical difference between the exact and the estimated values. From Fig. 6.5, it can be seen that the estimated value approaches the exact value, with a rms of the stabilized error of 0.1145 rad/s^2.

With reference to eq. (6.19), the central-difference method is adopted to obtain the estimated angular velocity $\hat{\boldsymbol{\omega}}$, as illustrated in Fig. 6.6. It can be seen that the estimated values do a good job in matching their exact counterparts. The rms value of the angular-velocity error over the whole period is obtained as 0.0416 rad/s.

Upon resorting to eq. (6.27), the attitude plots of the rotating disk are illustrated in Fig. 6.7. The exact and estimated attitude values are compared, the error $\delta\boldsymbol{\eta}$ being also plotted. We can observe a good match, the rms value of the error over the overall time interval being 0.0309.

Likewise, the brick SBA strapdown is used to measure the pose and twist of the disk. The strapdown is placed on the "front" face of the disk, with its centroid located a distance $d = 0.1$ m from the disk axis X. Figures 6.8–6.10 illustrate the estimated angular acceleration, angular velocity and attitude of the rigid disk, respectively. A good agreement between the measured and exact signals is observed, with the corresponding recorded rms values of the errors being 1.3693 rad/s^2, 0.2941 rad/s and 0.0678.

By comparison, it is apparent that for the harmonically excited rigid disk, the precision of the tetrahedral strapdown is much higher than that of the brick strapdown, which

carries, additionally, two more SBAs than its tetrahedral counterpart. Moreover, without knowledge of two earlier time steps for the updated $\mathbf{Q}$, the tetrahedral estimation is computationally more efficient, thereby reducing the overall computational cost.

For the rotating disk, the SNR of the strapdown in estimating the angular acceleration is obtained as

$$SNR = \begin{bmatrix} SNR_x \\ SNR_y \\ SNR_z \end{bmatrix} = \begin{bmatrix} 37.60 \\ 37.85 \\ 33.44 \end{bmatrix} \text{ db} \tag{6.52}$$

6.4.2 Freely Rotating Brick

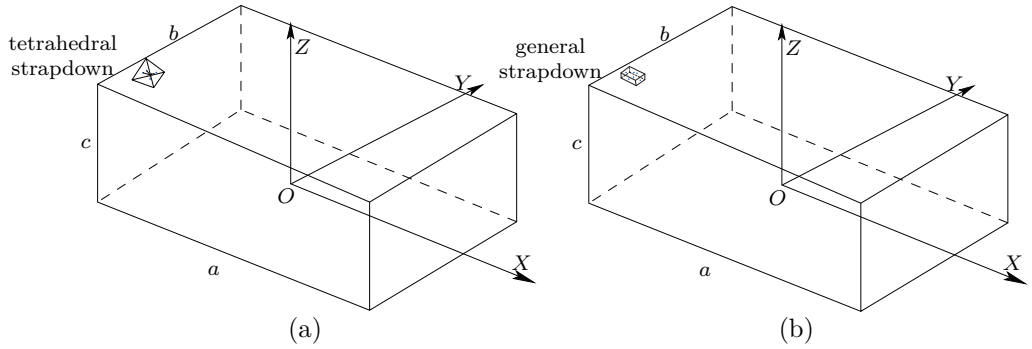

Fig. 6.11 A rigid brick with accelerometer strapdown

The second example involves a free rotating brick, depicted in Fig. 6.11, with dimensions given as: $a = 0.2$ m, $b = 0.15$ m and $c = 0.1$ m. Moreover, a frame $\mathcal{B}$ is attached to the brick under probing with its origin O located at the brick centre of mass. The tetrahedral as well as the brick strapdown are attached on the "top" face of the brick, of dimensions $a \times b$, one at a time, as illustrated in the figure, with the centroid of the strapdown coincident with that of the body face. Moreover, the brick strapdown is oriented so that its longest edges are parallel to their counterpart body-edges.The equation of motion of the brick is

$$\mathbf{I}\dot{\boldsymbol{\omega}} + \boldsymbol{\omega} \times \mathbf{I}\boldsymbol{\omega} = \mathbf{0}_3, \quad \boldsymbol{\omega}_0 = [13,\, 17,\, 22]^T \text{ rad/s} \tag{6.53}$$

where $\mathbf{I}$ is the inertia matrix of the brick about its centre of mass, when expressed in frame $\mathcal{B}$, $\mathcal{I}$ is given as $\mathbf{I}_{\mathcal{B}} = \rho \text{ diag}(2.6,\, 5,\, 4) \times 10^{-6}$ kg m^2, with a constant density $\rho = 2300$ kg/m^3. As $\boldsymbol{\omega}_0$ is not parallel to any of the principal directions of inertia—coincident with the

directions of the brick edges—the brick will wobble.

With the exact and estimated angular acceleration values plotted in Fig. 6.12, it is noteworthy that the estimated angular acceleration matches reasonably well the exact value, with a rms error over the whole simulation period of 0.1045 rad/s^2. That is, the strapdown estimation algorithm proposed here works well in estimating the angular acceleration of the freely rotating rigid body. Based upon the central-difference integration method within the estimation algorithm, the angular velocity is illustrated in Fig. 6.13, with a rms error of 0.3323 rad/s. The attitude is plotted in Fig. 6.14. A good agreement between the estimated and the exact attitude is observed, the rms error being 0.0402.

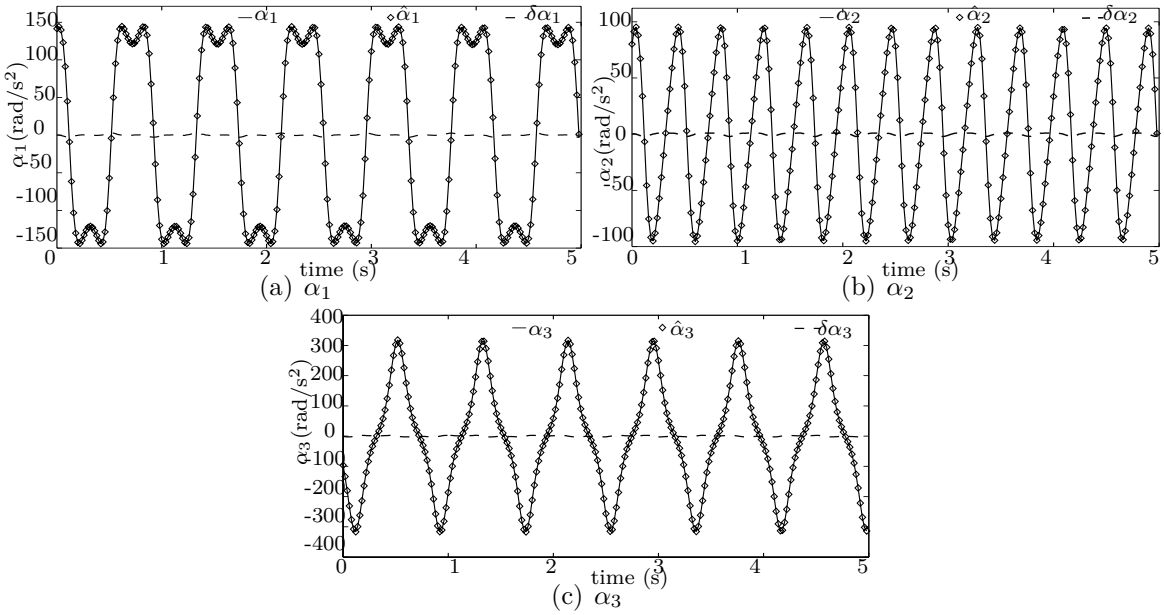

Fig. 6.12 Measured acceleration of the brick through isotropic SBA strapdown

Following the estimation algorithm of the brick SBA strapdown, the angular acceleration, angular velocity and attitude of the brick are shown in Figs. 6.15, 6.16 and 6.17, respectively. The estimated signals lie near the exact values, with error rms values of 4.3323 rad/s^2, 2.8726 rad/s and 0.0456, respectively. Hence, based upon the comparison of the rms errors of the simulation results, it is concluded that the tetrahedral SBA strapdown tracks the exact values better than its brick counterpart. The SNR of the strapdown in estimating the brick angular acceleration is 52.86 db, 47.39 db and 56.27 db in the x, y and z directions, respectively.

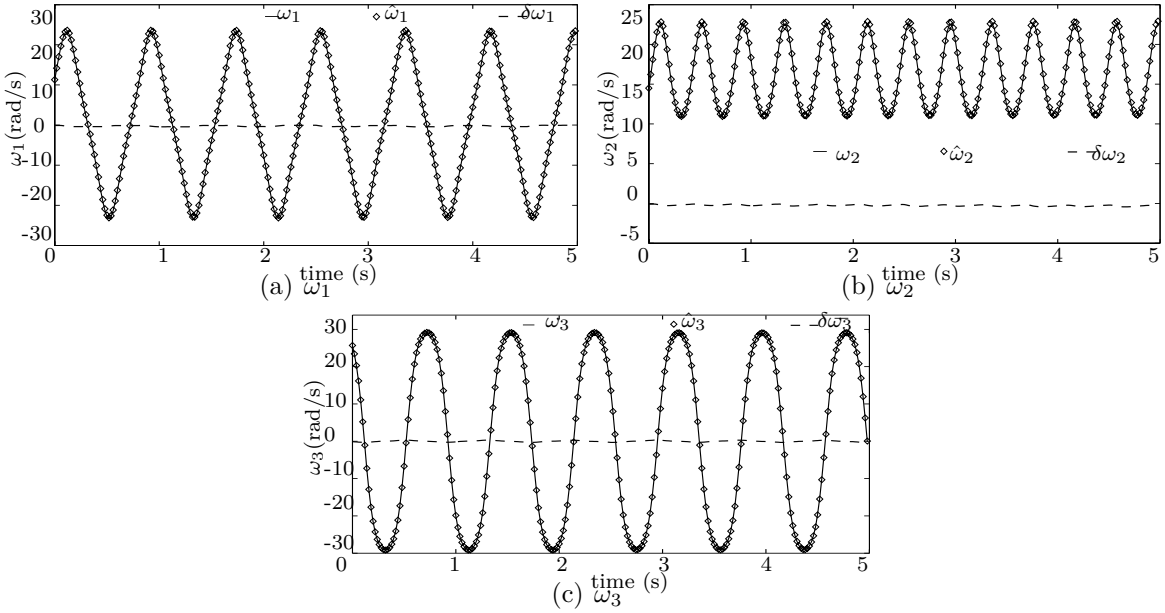

Fig. 6.13 Measured angular velocity of the brick through isotropic SBA strapdown

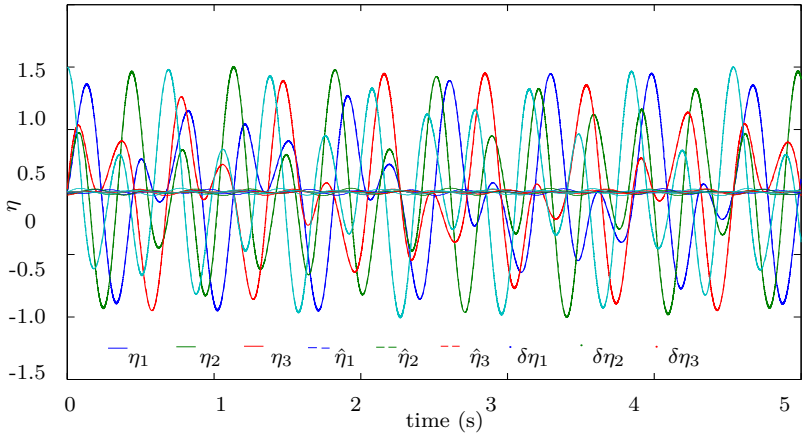

Fig. 6.14 Measured attitude of the brick through isotropic SBA strapdown

6.5 Summary

In this chapter, novel architectures of SBA strapdowns were proposed and employed for rigid-body pose and twist estimation. A set of SBAs is attached to the faces of a geometrically isotropic polyhedron to construct an isotropic strapdown. By virtue of the geometric isotropy of the polyhedron and the structurally planar isotropy of the SBA, the

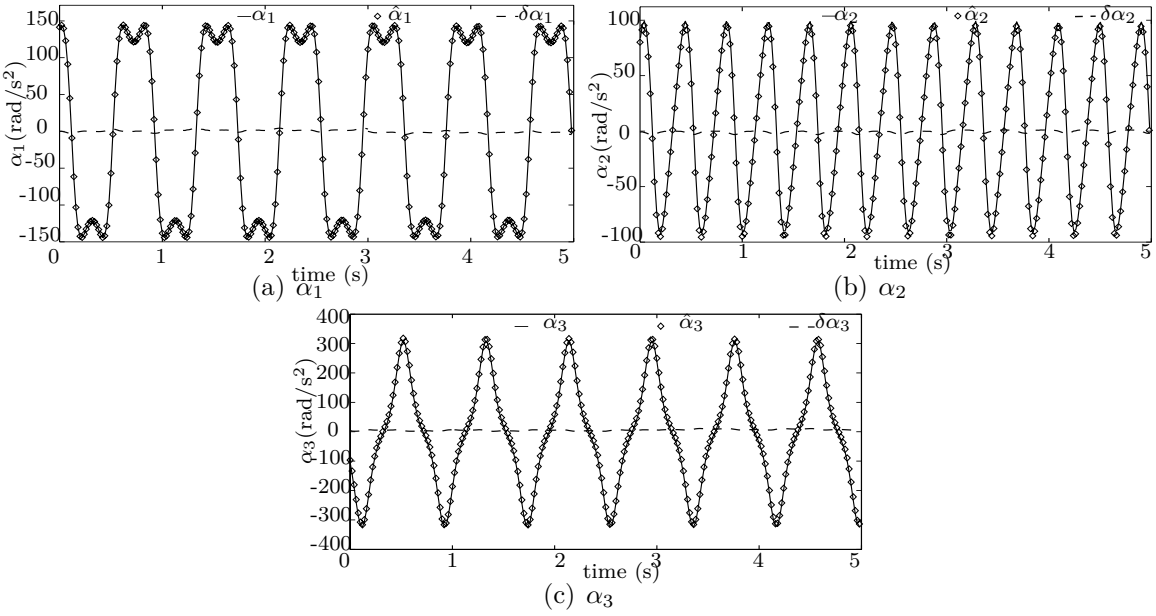

Fig. 6.15 Measured acceleration of the brick through a brick SBA strapdown

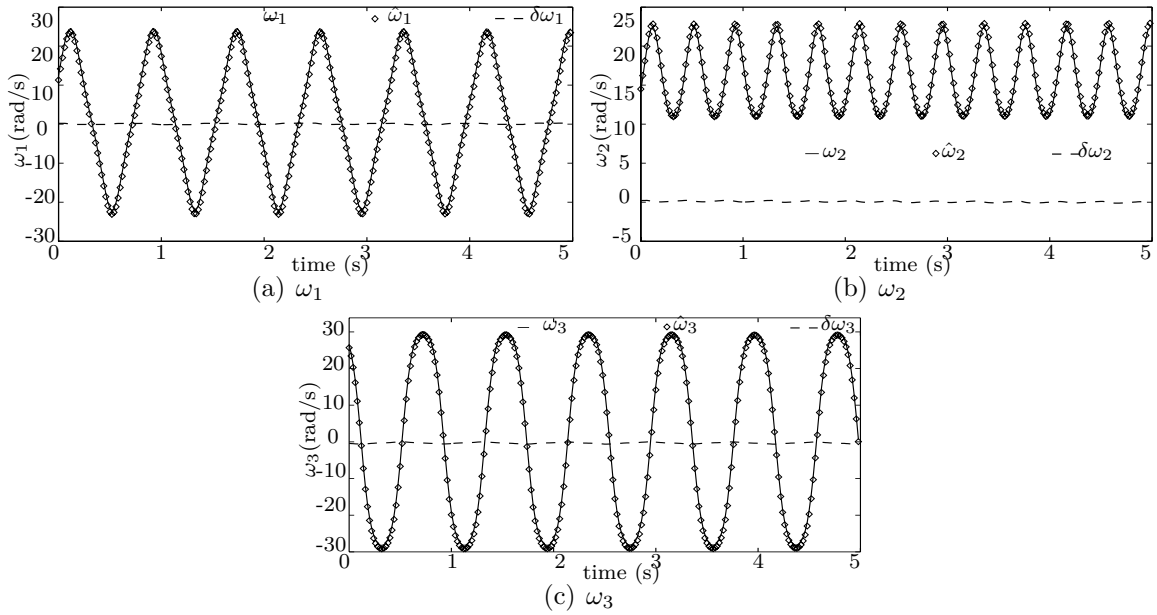

Fig. 6.16 Measured angular velocity of the brick through a brick SBA strapdown

isotropic SBA strapdown is predominant over other types of strapdowns for its capability in decoupling the acceleration field. As a consequence, the centripetal component of the

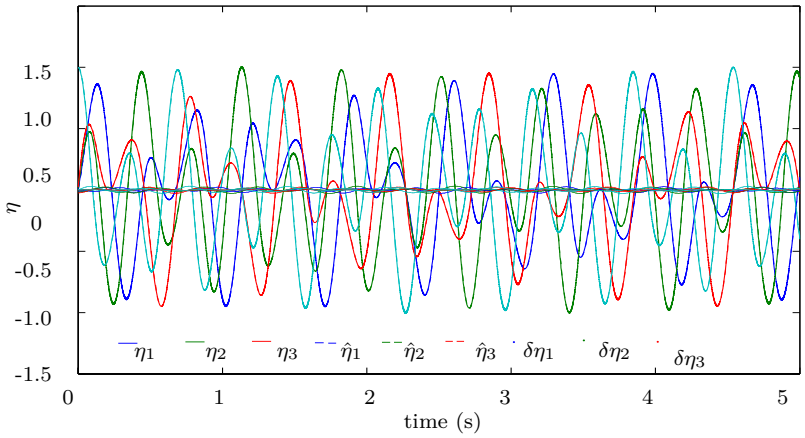

Fig. 6.17 Measured attitude of the brick through a brick SBA strapdown

relative point accelerations is filtered out, thereby leaving only the tangential component as the strapdown readout. By doing so, the point acceleration of a rigid body is decoupled from the angular acceleration, the estimation of the latter becoming straightforward. Two representative numerical examples were proposed, to investigate the performance of the SBA strapdown in estimating rigid body pose and twist. With the purpose of showcasing the precision of the isotropic strapdown, a more general strapdown is also employed. The simulation results demonstrate that the attitude and angular motions obtained by means of the proposed isotropic strapdown are consistently in close agreement with their exact counterparts. These results are significantly superior when compared with those of a general-type SBA strapdown.

Chapter 7

Conclusions and Recommendations

The increased demand for precise pose-and-twist estimation from industry drove us to conduct research in the area of accelerometer design, along with their strapdowns and estimation algorithms. In this dissertation, we have addressed two challenges: the difficulties of biaxial accelerometer design, as these are required to be sensitive in estimating acceleration in its plane; the intense demands for a more stable and precise estimation algorithm based on a novel accelerometer strapdown. The general outcome of this work is the innovative design of an isotropic biaxial accelerometer strapdown, based on our proposed Simplicial Biaxial Accelerometer. This accomplishment is achieved by means of the contributions explained below.

7.1 Contributions

Due to their inherent structural nature of exhibiting compliance about one axis while high stiffness about all other axes of motion, flexure hinges were employed in our accelerometer design. Four types of flexure hinges were studied; among them, the Lamé-notched hinge was chosen because of its geometric smoothness, which makes it ideal to avoid stress concentration. Based on the Lamé-notched hinge, the SBA design was undertaken. A systematic study of the SBA has been made: CAD design; stiffness analysis; FEA; and MEMS fabrication. The novel SBA design is required to be sensitive to even trivial excitations of the proof-mass in its plane, and behave isotropically along arbitrary planar directions. At the same time, its out-of-plane stiffness should be much higher than its in-plane counterpart. Both modal analysis and forced response under loading were conducted on the FE

model of the SBA, to validate the design objectives. Simulation results illustrated that the SBA has equal sensitivity along any planar directions, the out-of-plane motion requiring much higher excitation frequencies to be excited. Afterwards, a piezoresistive electronic measurement circuit was designed to implement on the SBA. The output voltage was required to be sensitive in the motion of the proof-mass. Simulation results in terms of the ANSYS Coupled Field module demonstrated an excellent agreement, consistent with the response of the proof-mass under loading.

Being confident of the SBA design by numerical validation, we conducted its MEMS fabrication. The microfabrication was made on the 4" single-crystal silicon wafer by five masks, in which the measurement circuits employ three half-Wheatstone bridges to provide voltage signals. The fabrication is possible because of the SBA planar nature.

By resorting to geometrically isotropic solids, we broke new ground in carrying out a novel accelerometer strapdown design: the isotropic SBA strapdown. The distinguished advantages of this strapdown can be attributed to two aspects: the estimation drift throughout the overall estimation time history is minimized, the estimation accuracy thus being high; its inherent geometric isotropy helps decouple the acceleration tangential component from its centripetal counterpart, thus making the acceleration estimation straightforward and accurate. By means of simulation over two representative numerical examples, the tetrahedral strapdown was found accurate in estimating angular acceleration and angular velocity for 3D rigid bodies. Experimental tests of the strapdown are important and mandatory.

7.2 Future Research Directions

Beyond the issues and the scope of this dissertation, several open challenges and extensions exist that will benefit from further research efforts in this realm. A list of recommendations for future work is summarized below:

7.2.1 Research Extensions

Throughout the systematic study of SBA strapdowns, experimental testing is an important and unavoidable step, before industrial applications. The testing is composed of two parts: the assembly of the SBA MEMS models to construct a tetrahedral strapdown; the pose-and-twist estimation of the objective rigid-body, using the strapdown and testing

devices. The Dual-Arm Testbed in the *Robotic Mechanical Systems Laboratory*, McGill University, will be employed as the testing platform. Due to the extensive time-consuming process of assembling, as well as debugging the testbed, the experimental testing is beyond the scope of this dissertation, testing recommendations being provided in this section.

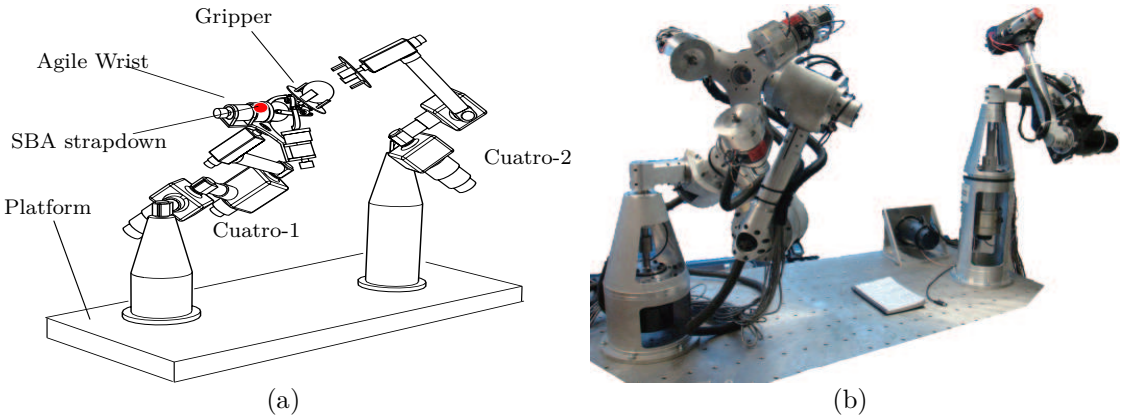

Fig. 7.1 Dual-Arm Testbed: (a) CAD illustration; (b) experiment device

Figure 7.1 illustrates the Dual-Arm Testbed, which was designed to investigate the collision of mechanical systems. The Cuatro-2 arm moves an object in space; the Cuatro-1, supplied with a 3 DOF spherical parallel manipulator, the Agile Wrist, functions to grasp the object held by Cuatro-2. The SBA strapdown will be attached to the gripper of Cuatro-1 to render its pose-and-twist.

The recommendations for the test are listed below:

- Three main issues should be attended, regarding the strapdown assembly: all the SBAs are required to be attached rigidly to the tetrahedral base frame; contact between the SBA proof-mass and the strapdown surface is not allowed; all the SBAs share a common origin.

- Afterwards, the strapdown is attached rigidly to the Dual-Arm Testbed. The strapdown is intended to estimate, in real-time, the pose and twist of the object. Diverse types of movements will be performed by the testbed, such as translation, sudden acceleration, impact, collision, etc.; the strapdown is expected to yield an output signal to provide information on the pose and twist of the rigid-body. Accuracy of the estimated pose and twist should be investigated; improvements should be made as needed.

Another extension is a deeper investigation of the tetrahedral strapdown. In order to meet increased requirements from industry for a low cost accelerometer strapdown with good accuracy in estimating rigid-body pose and twist, investigations on some design parameters, such as the edge length of the tetrahedron frame as well as its material and weight, will be made. Pose and twist estimation under the effect of these parameters is worth studying.

For the SBA design, the out-of-plane natural frequency f_z is around 2.5 times higher than the in-plane natural frequencies, f_x and f_y. In other words, the frequency ratio of the SBA is almost 2.5. At high frequency excitations, unavoidable, even though not obvious, out-of-plane motions of the proof-mass are observed. From this point of view, it will be valuable to continue studying possible approaches to increase the frequency ratio. This will be the third stage of this project.

7.2.2 Methodology

Though drift throughout the time-history of pose-and-twist estimation is minimized, refinements to the numerical methods to increase calculation precision is still appealing. The study on enhancing computational efficiency will be another future methodology work. Improvement of the current estimation algorithms to obtain a more time-efficient method should lead to decreasing the high computational cost.

7.2.3 Industrial Applications

The novel SBA strapdowns proposed in this dissertation may lend themselves to applications in the aero- and astronautics realm. As Canadians, we are proud of the Canadarm in the International Space Station, which integrates inspiration, novelty and diligent work of astronautical scientists and engineers. As illustrated in Fig 7.1, the SBA strapdown will be tested on the Dual-Arm testbed. The Dual-Arm testbed is able to emulate rendez-vous operations. Therefore, the SBA strapdown can be extended to applications in improving precision and smoothness in certain operations of the International Space Station.

Besides its wide usage in the astro- and aeronautical realm, the application in robotic surgery is highlighted. Through years of stressing works in the field of MEMS accelerometer, we expect that the commercial implementation of the strapdown design will help improve the precision of surgical operations. The accelerometer strapdown may reduce the

procedures of curing the sick and saving medical resources, while providing more precise and smooth surgical operation services. Within several years of biomedical applications, the strapdown may help improve the service quality and efficiency of Canadian hospitals, thereby helping address problems of the notorious long waiting lists for patients requiring medical services in Canada.

References

[1] J. Angeles, Fundamentals of robotic mechanical systems: theory, methods, and algorithms, 3rd ed., Springer, New York, 2007.

[2] R. Hanson, Using multiple MEMS IMUs to form a distributed inertial measurement unit, Master of science thesis, Air Force Institute of Technology, Wright-Patterson Air Force Base Ohio, USA (2005).

[3] Z. Qin, L. Baron, L. Birglen, Robust design of inertial measurement units based on accelerometers, ASME Journal of Dynamics System, Measurement and Control 131 (3).

[4] H. D. E. Alvarez, Geometric configuration of redundant IMUs, Master of science thesis, The University of Texas at Austin, Austin, Texas, USA (2010).

[5] P. Cardou, Design of multiaxial accelerometers with simplicial architectures for rigid-body pose and twist estimation, Ph.D. thesis, McGill University, Montreal, Canada (2008).

[6] J. Angeles, T. Zou, Isotropic accelerometer strapdowns and algorithms for rigid-body pose and twist estimation, Provisional Patent Application, led at USPTO under EFS ID: 13268626, Application 61672366, (2012).

[7] P. L. Walter, History of the accelerometer, Journal for Sound and Vibration 31 (1996) 16–22.

[8] H. J. Mertz, Kinematics and kinetics of whiplash, Ph.D. thesis, Wayne State University, Detroit, USA (1967).

[9] K. K. W. Padgaonkar, A. J., A. I. King, Measurement of angular acceleration of a rigid body using linear accelerometers, ASME Journal of Applied Mechanics (1975) 552–556.

[10] N. K. Mital, A. I. King, Computation of rigid-body rotation in three-dimensional space from body-fixed linear acceleration measurements, ASME Journal of Applied Mechanics 46 (1979) 925–930.

[11] L. M. Roylance, Miniature integrated circuit accelerometer for biomedical applications, Ph.D. thesis, Standford University, Stanford, CA, USA. (1978).

[12] N. Maluf, An introduction to microelectromechanical systems engineering, Artech House Publishers, Boston, 2000.

[13] S. P. Won, N. Parnian, M. F. Golnaraghi, W. W. Melek, A quaternion-based tilt angle correction method for a hand-held device using an inertial measurement unit, Proceedings of IEEE International Conference on Industial Electronics, Orlando, FL, 2008, pp. 2971–2975.

[14] P. Cardou, J. Angeles, Simplectic architectures for true multi-axial accelerometers: a novel application of parallel robots, IEEE International Conference on Robotics and Automation, Rome, Italy, 2007, pp. 181–186.

[15] E. Kreyszig, Advanced engineering mathematics, John Wiley & Sons, New York, 1997.

[16] F. Majou, The design of parallel-kinematic machine tools using kinetostatic performance criteria, The 3rd International Conference on Metal Cutting, France, June, 2001.

[17] J. Angeles, The qualitative synthesis of parallel manipulators, ASME Journal of Mechanical Design 126 (2004) 617–624.

[18] N. Lobontiu, Compliant mechanisms: design of flexure hinges, CRC Press: Boca Raton, FL, USA, 2003.

[19] R. S. Hartenberg, J. Denavit, Kinematic Synthesis of Linkages, McGraw-Hill, New York, 1964.

[20] R. V. Jones, Parallel and rectilinear spring movements, J. Sci. Instrum. 28 (2) (1951) 38–41.

[21] J. Paros, L. Weisbord, How to design flexure hinges, J. Machine Design (1965) 151–156.

[22] S. T. Smith, V. G. Badami, J. S. Dale, Y. Xu, Elliptical flexure hinges, Review of Scientific Instruments 68 (1997) 1474–1483.

[23] L. Howell, Compliant Mechanisms, Wiley, New York, 2001.

[24] H.-J. Su, A pseudorigid-body 3R model for determining large deflection of cantilever beams subject to tip loads, ASME Journal of Mechanisms and Robotics 1 (2009) 1–9.

[25] S. Smith, Flexure Elements of Elastic Mechanisms, Gordon and Breach Science Publishers, The Netherlands, 2000.

[26] F. De Bona, M. G. Munteanu, Optimized flexural hinges for compliant micromechanisms, Springer Science 44 (2005) 163–174.

[27] P. Bernardoni, P. Bidaud, C. Bidard, A new compliant mechanism design methodology based on flexible building blocks, Proceedings of SPIE, San Diego, CA, USA, 2004.

[28] R. R. Ma, A modular, open-source 3d printed underactuated hand, 2013 IEEE International Conference on Robotics and Automation (ICRA), Karlsruhe, Germany, May 6-10, 2013, pp. 2722–2728.

[29] T. Mineta, S. Kobayashi, Y. Watanabe, et al., Three-axis capacitive accelerometer with uniform axial sensitivities, Journal of Micromechanics and Microengineering 6 (1996) 431–435.

[30] R. Puers, S. Reyntjens, Design and processing experiments of a new miniaturized capacitive triaxial accelerometer, Sensors and Actuators 68 (1998) 324–328.

[31] A. Devices, ADXL320 Datasheet, One Technology Way, P.O. Box 9106, Norwood, MA, USA., 2004.
URL `www.analog.com`

[32] J. J. Allen, Micro Electro Mechanical System Design, Taylor & Francis Group, 2005.

[33] J. Ryu, D. Gewon, K. Moon, Optimal design of a flexure hinge based $xy\theta$ wafer stage, Journal of Precision Engineering 21 (1997) 18–28.

[34] H. Pham, I. Chen, Stiffness modeling of flexure parallel mechanism, Journal of Precision Engineering 29 (2005) 467–478.

[35] Y. Li, Q. Xu, Design and analysis of a totally decoupled flexure-based xy parallel micromanipulator, IEEE Trans. Robot 25 (2008) 645–657.

[36] S. Zhang, E. Fasse, A finite-element-based method to determine the spatial stiffness properties of a notch hinge, ASME Journal of Mechanical Design 123 (2001) 335–345.

[37] B. Yi, Design and experiment of a 3dof parallel micro-mechanism utilizing flexure hinges, IEEE Transactions on Robotics 19 (2003) 786–792.

[38] L. Hale, A. Slocum, Optimal design techniques for kinematic couplings, Journal of Precision Engineering 25 (2001) 114–127.

[39] N. Simaan, M. Shoham, Stiffness synthesis of a variable geometry six-degrees-of-freedom double planar parallel robot, Int J Robotic Res 22 (2003) 757–775.

[40] Y. Yu, L. Howell, C. Lusk, Dynamic modeling of compliant mechanisms based on the pseudo-rigid-body model, ASME Journal of Mechanical Design 127 (2005) 760–765.

[41] D. Handley, T. Lu, Y. Yong, W. Zhang, A simple and efficient dynamic modeling method for compliant micropositioning mechanisms using flexure hinges, Vol. 5276, Proceedings of the SPIE on Device and Process Technologies for MEMS, Mircoelectronics, and Photonics III, 2003, pp. 67–76.

[42] C. Gosselin, D. Zhang, Stiffness analysis of parallel mechanisms using a lumped model, International Journal of Robotics and Automation 17 (1) (2002) 17–27.

[43] F. M. Melodie, A. F. S. Nur, M. O. Oliver, On cartesian stiffness matrices in rigid body dynamics: an energetic perspective, Multibody Syst. Dyn. 24 (2010) 441–472.

[44] T. Zou, J. Angeles, P. Zsombor-Murry, A comparative study of architectures for uniaxial accelerometers, Proceedings of the Canadian Society for Mechanical Engineering, Victoria, British Columbia, Canada, 2010.

[45] J. Kövecses, J. Angeles, The stiffness matrix in elastically articulated rigid-body systems, Multibody Syst. Dyn. 18 (2007) 169–184.

[46] C. Gosselin, Stiffness mappling for parallel manipulators, IEEE Trans Robot Autom 6 (1990) 377–382.

[47] T. Zou, J. Angeles, Decoupling of the cartesian stiffness matrix: a case study on accelerometer design, Proc. ASME 2011 International Design Engineering Technical Conferences & Computers and Information in Engineering Conference IDETC/CIE 2011, Washington, DC, August 28-31, Paper DETC2011-47914, 2011.

[48] X. Ding, J. M. Selig, On the compliance of coiled springs, International Journal of Mechanical Sciences 46 (2004) 703–727.

[49] J. M. Selig, X. Ding, Structure of the spatial stiffness matrix, International Journal of Robotics and Automation 17 (1) (2002) 1–16.

[50] J. Angeles, On the nature of the cartesian stiffness matrix, Ingeniería Mecánica 3 (2010) 163–170. See accompanying *Corrigenda*, both items available at `http://revista--somim.net/`.

[51] J. B. Hopkins, M. L. Culpepper, A screw theory basis for quantitative and graphical design tools that define layout of actuators to minimize parasitic errors in parallel flexure systems, Precision Engineering 34 (2010) 767–776.

[52] D. Zhu, Y. Feng, A spatial 3-dof translational compliant parallel manipulator, Applied Mechanics and Materials 34-35 (2010) 143–147.

[53] K. H. Hunt, Kinematic Geometry of Mechanisms, Oxford Univeristy Press, New York, 1978.

[54] J. Phillips, Freedom in Machinery, Cambridege University Press, 1984.

[55] H. Lipkin, T. Patterson, Geometric properties of modelled robot elasticity: part ii - decomposition, DE 45 (1992) 179–185.

[56] R. S. Ball, Theory of Screws, Cambridege University Press, 1998.

[57] C. J. Kim, Functional characterization of compliant building blocks utilizing eigentwists and eigenwrenches, ASME IDETC/CIE, New York, USA, 2008.

[58] N. Yazdi, F. Ayazi, K. Najafi, Micromachined inertial sensors, Proceedings of the IEEE 86 (8) (1998) 1640–1659.

[59] S. P. Kau, Integrated guidance system and method for providing guidance to a projectile on a trajectory, Patent Number EP636862-A, US5442560-A (1995).

[60] R. Li, J. Liu, J. Lai, Z. Xiong, Y. Sun, W. Zhao, Q. Zeng, B. Wen, Attitude determination method of mini-aircraft inertial integrated navigation system, Patent Number CN101033973-A, CN101033973-B (2007).

[61] G. Zhou, Y. Ben, B. Xu, S. Chen, Q. Yu, H. Gao, L. Wu, J. Cheng, X. Zhang, Closed-loop ccalibration method of micro-mechanical gyroscope inertial measuring component, Patent Number CN101246023-A (2008).

[62] W. Gao, G. Zhou, T. Cao, B. Xu, D. Hu, Y. Ben, F. Sun, L. Tang, Z. Li, W. Wang, Alignment method of strapdown inertial navigation system, Patent Number CN101915579-A (2010).

[63] Y. Ben, Y. Chai, J. Fu, W. Gao, J. Gong, Z. Li, W. Wang, B. Xu, X. Zhang, Y. Zhang, Optical fiber gyro strapdown inertial navigation system damping method, Patent Number CN101696883-A (2010).

[64] W. Chou, L. Ding, W. Ding, Strapdown inertial navigation device for aerospace application, Patent Number CN102235862-A (2011).

[65] N. Barbour, G. Schmidt, Inertial sensor technology trends, IEEE Sensors 1 (4) (2001) 332–339.

[66] L. D. Dinapoli, The measurement of angular velocities without the use of gyros, Master of science thesis, The Moore School of Electrical Engineering, University of Pennsylvania, Philadelphia, USA (1965).

[67] J. Collin, G. Lachapelle, MEMS-IMU for personal positioning in a vehicle—a gyro-free approach, GPS 2002 conference (session c3a), Portland, OR, USA, 2002.

[68] Y. K. Peng, M. F. Golnaraghi, A vector-based gyro-free inertial navigation system by integrating existing accelerometer network in a passenger vehicle, The Proceedings IEEE Position Location and Navigation Symposium, Monterey, CA, USA, 2004, pp. 234–242.

[69] P. Cappa, F. Patanè, S. Rossi, Two calibration procedures for a gyroscope-free inertial measurement system based on a double-pendulum apparatus, Meas. Sci. Technol. 19 (2008) 32–38.

[70] D. Dubé, P. Cardou, The calibration of an array of accelerometers, Transactions of the Canadian Society for Mechanical Engineering 35 (2) (2011) 251–267.

[71] C. M. Fang, A research of robotic surgery technique by the use of mems accelerometer, 24th Annual Conference and the Annual Fall Meeting of the Biomedical Engineering Society EMBS/BMES Conference, Houston, Texas, USA, 2002.

[72] Y. Lim, Symmetry groups of platonic solids, Technical report, Stanford, 2008.

[73] W. Wu, The Platonic Solids, Technical report, UC Berkeley, 2005.
URL `http://www.ocf.berkeley.edu/~wwu/papers/platonicsolids.pdf`

[74] P. J. Morandi, Computing the symmetry groups of the Platonic solids with the help of Maple, Vol. 9, Springer India, in co-publication with Indian Academy of Sciences, 2004.

[75] C. W. Tan, S. Park, Design of accelerometer-based inertial navigation systems, IEEE Trans. Instrum. Meas. 54 (6) (2005) 2520–2530.

[76] J. H. Chen, S. C. Lee, D. B. DeBra, Gyroscope free strapdown inertial measurement unit by six linear accelerometers, J. Guid. Control. Dynam. 17 (2) (1994) 286–290.

[77] C. W. Tan, S. Park, K. Mostov, P. Varaiya, Design of gyroscope-free navigation systems, 2001 IEEE Transportation Systems Conference Proceedings, Oakland, CA, USA, 2001, pp. 286–291.

[78] Q. Wang, M. L. Ding, P. Zhao, A new scheme of non-gyro inertial measurement unit for estimating angular velocity, The 29th annual conference of the IEEE Industry Electronics Society (IECON'2003), Virginia, USA, 2003, pp. 1564–1567.

[79] A. J. Padgaonkar, K. W. Krieger, A. I. King, Measurement of angular acceleration of a rigid body using linear accelerometers, ASME J. Appl. Mech. 42 (1975) 552–556.

[80] P. C. Lin, C. W. Ho, Design and implementation of a 9-axis inertial measurement unit, 2009 IEEE International Conference on Robotics and Automation, Kobe, Japan, 2009.

[81] B. Zappa, A. J. Legnana, G.and van der Bogert, R. Adamini, On the number and placement of accelerometers for angular velocity and acceleration determination, ASME J. Dyn. Syst. Meas. Contr. 123 (3) (2001) 552–554.

[82] W. T. Latt, U.-X. Tan, C. N. Riviere, W. T. Ang, Placement of accelerometers for high sensing resolution in micromanipulation, Sensors and Actuators A: Physical 167 (2011) 304–316.

[83] L. Masia, P. Cappa, F. Patane, System for assessing a law of motion and related method, Patent Number EP1837626-A2, IT1360091-B, EP1837626-A3 (2008).

[84] P. Cardou, J. Angeles, Angular velocity estimation from the angular acceleration matrix, Journal of Applied Mechanics 75 (2) (2008) 021003–1–8.

[85] P. Cardou, J. Angeles, Angular-velocity estimation from the centripetal component of the rigid-body acceleration field, In Advances in Robot Kinematics (2008) 353–360.

[86] N. Lobontiu, J. S. N. Paine, E. Garcia, M. Goldfarb, Corner-filleted flexure hinges, ASME Journal of Mechanical Design 123 (2001) 346–352.

[87] J. J. Risler, Mathematical methods for CAD, Cambridge University Press, 1992.

[88] H. Neuber, Theory of notch stresses: principles for exact calculation of strength with reference to structural form and material, United States Atomic Energy Commission, Office of Technical Information, Translation Series, 1961.

[89] J. D. Hoffman, Numerical methods for engineers and scientists, Marcel Dekker, New York, 2001.

[90] W. C. Young, Roark's formulas for stress and strain, McGraw-Hill, New York, 1989.

[91] M. Bao, H. Yang, Squeeze film air damping in mems, Sensors and Actuators A: Physical 136 (2007) 3–27.

[92] T. Veijola, Chapter fourteen–gas damping in vibrating mems structure, Handbook of Silicon Based MEMS Materials and Technologies (2010) 259–279.

[93] Y. H. Cho, B. M. Kwak, A. P. Pisano, R. T. Howe, Slide film damping in laterally driven microstructures, Sensors and Actuators A: Physical 40 (1994) 31–39.

[94] P. Pokkunuria, P. Nissensonb, D. Dabdubb, Impact of the knudsen number and mass-transfer expression on multi-phase kinetic modeling, Atmospheric Environment 44 (2) (2009) 153–163.

[95] G. E. Carlson, Signal and Linear System Analysis, Allied Publishers Ltd., 1992.

[96] J. Richter, O. Hansen, A. N. Larsen, J. L. Hansen, G. F. Eriksen, E. V. Thomsen, Piezoresistance of silicon and strained $Si_{0.9}Ge_{0.1}$, Sensors and Actuators A 123-124 (2005) 388–396.

[97] S. Sze, Semiconductor Sensors, John Wiley & Sons, New York, 1994.

[98] Y. Kanda, A graphic representation of the piezoresistance coefficients in silicon, IEEE Transactions on Electron Devices ED-29 (1) (1982) 64–70.

[99] W. P. Mason, R. N. Thurston, Use of piezoresistive materials in the measurement of displacement, force and torque, J. Acous. Soc. of Am. 29 (1957) 1096–1101.

[100] S. D. Senturia, Microsystem Design, Kluwer Academic Publishers, Norwell, MA, 2001.

[101] T. D. Tan, Simulation and design of a 3-dof piezoresisitive accelerometer with uniform resolution, International Journal for Information and Electronics Engineering 3 (2013) 353–356.

[102] A. A. Barlian, W. Park, R. M. J. Joseph, A. J. Rastegar, B. L. Pruitt, Review: Semiconductor piezoresistance for microsystems, Proc IEEE Inst Electr Electron Engineering 97 (2009) 513–552.

[103] T. Cornelius, MEMS/NEMS Handbook Techniques and Applications, MEMS/NEMS Handbook Techniques and Applications, 2006.

[104] B. Lent, Pratical considerations of accelerometer noise, technical report, Endevco Inc., San Juan Capistrano, Canada (2007).

[105] K. Tuck, How many bits are enough? the trade-off between high resolution and low power using oversampling modes, technical report, Freescale Semiconductor Inc., Tempe, Arizona (2010).

[106] E. J. Eklund, A. M. Shkel, Single-mask fabrication of high-g piezoresistive accelerometers with extended temperature range, Journal of Micromechanics and Microengineering 17 (2007) 730–736.

[107] H. B. Robert, Mechatronic Systems, Sensors, and Actuators: Fundamentals and Modeling, CRC Press Inc, 2007.

[108] J. K. Davidason, K. H. Hunt, Robots and Screw Theory: applications of kinematics and statics to robotics, Oxford University Press, 2004.

[109] D. K. Smith, Constraint anslysis of assembles using screw theory and tolerance sensitivities, Master of science thesis, Department of Mechanical Engineering, Brigham Young Univeristy, UT, USA (2001).

[110] J. Selig, Geometric Fundamentals of Robotics, Springer, London, 2005.

[111] A. Saxena, G. K. Ananthasuresh, Topology synthesis of compliant mechanisms for nonlinear force-deflection and curved path specifications, ASME J. Mech. Des. 123 (1) (2004) 33–42.

[112] M. Reiner, S. Cora, Theoretical Mechanics, Springer, 2010.

[113] A. D'Souza, V. Garg, Advanced Dynamics: Modeling & Analysis, Prentice Hall, 1983.

[114] L. Sciavicco, B. Siciliano, Modeling and Control fo Robot Manipulators, New York: The McGraw-Hill Companies. Inc., 1996.

[115] W. Khalil, E. Dombre, Modeling, Identification and Control of Robots, Butterworth-Heinemann, 2004.

[116] K. Al-Widyan, J. Angeles, S. Ostrovskaya, A robust simulation algorithm for conservative linear mechanical systems, International Journal for Multiscale Computational Engineering 1 (2003) 289–309.

[117] A. K. Pradeep, P. J. Yoder, R. Mukundan, On the use of dual-matrix exponentials in robotic kinematrics, The International Journal of Robotics Research 8 (5) (1989) 57–66.

[118] R. G. Roberts, On the normal form of a spatial stiffness matrix, Proc. of the 2002 IEEE International Conference on Robotics & Automation, Washington, DC, May 11-15, 2002, pp. 556–561.

[119] G. Strang, Linear Algebra and its Applications 3rd ed, Harcourt, Brace, Jovanovich, San Diego, 1988.

[120] J. L. Erickson, Tensor fields, in: S. Flügge (Ed.), Encyclopedia of Physics/Handbuch der Physik, Vol. III/1, Springer-Verlag, Berlin-Göttingen-Heidelberg, 1960.

[121] A. A. Barlian, S. J. Park, V. Mukundan, B. L. Pruitt, Design and characterization of microfabricated piezoresistive floating element-based shear stress sensors, Sensors and Actuators 134 (2007) 77–87.

[122] A. Patridge, K. Reynolds, W. Chui, A high-performance planar piezoresistive accelerometer, Journal of Microelectromechanical Systems 9 (2000) 58–66.

[123] B. K. Nguyen, K. Hoshino, K. Matsumoto, I. Shimoyama, Insertion force sensor by sidewall-doping with rapid thermal diffusion, MEMS 2006, Istanbul, Turkey, 2006, pp. 22–26.

[124] N. P. Mahalik, Micromanufacturing and Nanotechnology, Springer, 2005.

[125] R. H. Cannon, Dynamics of Physical Systems, McGraw-Hill, 1967.

[126] A. J. White, J. B. Young, Time-marching method for the prediction of two-dimensional, unsteady flows of condensing steam, Journal of Propulsion and Power 9 (1993) 579–587.

[127] J. Jer-Nan, Q. Minh, Identification and Control of Mechanical Systems, Cambridge University Press, 2004.

[128] L. Baron, J. Angeles, The direct kinematics of parallel manipulators under joint-sensor redundancy, IEEE Transactions on Robotics and Automation 16 (1) (2000) 12–19.

[129] C. Hagleitner, K. U. Kirstein, "circuit and system integration", cmos-mems, advanced micro & nanosystems, edited by baltes, h., brand, o., fedder, g., hierold, c., korvink, j., and tabata, o., Ph.D. thesis, WILEY-VCH, Weinheim, Germany (2005).

Appendix A

Rotation Matrices for Tetrahedron and General-Type SBA Strapdowns

A.1 Case of a Tetrahedral Strapdown

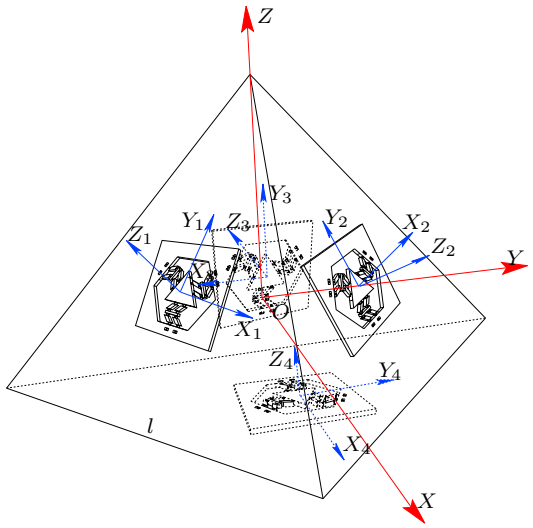

Fig. A.1 Illustration of the tetrahedral strapdown with its local and global coordinate frame

Figure A.1 illustrates the tetrahedral strapdown with its local and global coordinate frames. It is noteworthy that the coordinate frame located at the origin of the strapdown frame coincides with the global coordinate frame attached at the rigid-body centroid. The rotation matrix $\mathbf{R}_i$ for the i^{th} SBA is obtained below.

- For SBA 1, the coordinate frame is rotated about X_1 with $\mathbf{R}_{X_1}$ through an angle θ_{X_1}, then about Z_1 with $\mathbf{R}_{Z_1}$ through θ_{Z_1}, the rotation matrices being given by

$$\mathbf{R}_{X_1} = \begin{bmatrix} 1 & 0 & 0 \\ 0 & \cos\theta_{X_1} & -\sin\theta_{X_1} \\ 0 & \sin\theta_{X_1} & \cos\theta_{X_1} \end{bmatrix}, \quad \mathbf{R}_{Z_1} = \begin{bmatrix} \cos\theta_{Z_1} & -\sin\theta_{Z_1} & 0 \\ \sin\theta_{Z_1} & \cos\theta_{Z_1} & 0 \\ 0 & 0 & 1 \end{bmatrix} \tag{A.1}$$

  where $\theta_{X_1} = -\pi/3$ is the angle between any two faces of the strapdown, $\theta_{Z_1} = -\pi/6$. The overall transformation matrix $\mathbf{R}_1$ can be expressed as:

$$\mathbf{R}_1 = \mathbf{R}_{Z_1}\mathbf{R}_{X_1} \tag{A.2}$$

- For SBA 2, the coordinate frame is rotated about X_2 by θ_{X_2}, then it is rotated about Z_2 by θ_{Z_2}, with the rotation matrices as:

$$\mathbf{R}_{X_2} = \begin{bmatrix} 1 & 0 & 0 \\ 0 & \cos\theta_{X_2} & -\sin\theta_{X_2} \\ 0 & \sin\theta_{X_2} & \cos\theta_{X_2} \end{bmatrix}, \quad \mathbf{R}_{Z_2} = \begin{bmatrix} \cos\theta_{Z_2} & -\sin\theta_{Z_2} & 0 \\ \sin\theta_{Z_2} & \cos\theta_{Z_2} & 0 \\ 0 & 0 & 1 \end{bmatrix} \tag{A.3}$$

  in which $\theta_{X_2} = -\pi/3$, $\theta_{Z_2} = -2\pi/3$. Likewise, the overall transformation matrix $\mathbf{R}_2$ is expressed as:

$$\mathbf{R}_2 = \mathbf{R}_{Z_2}\mathbf{R}_{X_2} \tag{A.4}$$

- The rotation for SBA 3 is obtained likewise: rotation about X_3 first, then rotations about Z_3, with $\theta_{X_3} = -\pi/3$, $\theta_{Z_3} = \pi/2$.

- The local coordinate frame of SBA 4 coincides with $OXYZ$; hence, the rotation involved is the 3×3 identity matrix.

A.2 Case of a General Strapdown

Similar to the case of a tetrahedral strapdown, as illustrated in Fig. A.2, the position vector of each SBA centroid in $OXYZ$ is obtained under a rotation of $O_iX_iY_iZ_i$. The transformation is investigated below:

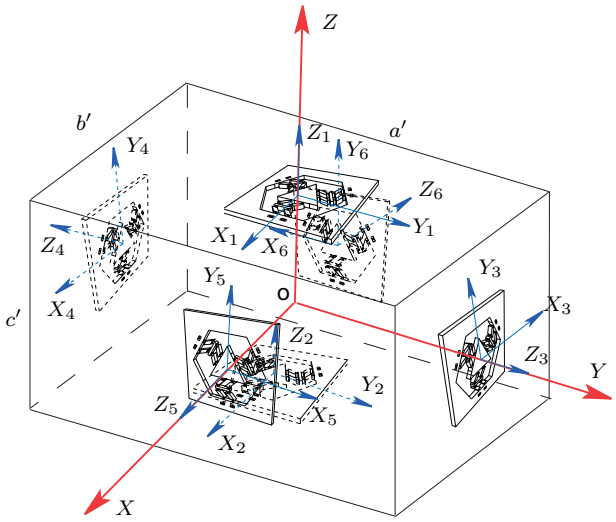

Fig. A.2 Illustration of the brick strapdown with local and global coordinate frames

- For SBA 1 and SBA 2, the rotation matrix is also the identity, as the coordinate directions are the same as those of $OXYZ$.

- For SBA 3 and SBA 4, the local coordinate frame is rotated about the Y_3 and Y_4 axes respectively, followed by a rotation about X_3 and X_4, respectively, with the rotation matrices:

$$\mathbf{R}_{Y_3} = \mathbf{R}_{Y_4} = \begin{bmatrix} \cos\theta_1 & 0 & \sin\theta_1 \\ 0 & 1 & 0 \\ -\sin\theta_1 & 0 & \cos\theta_1 \end{bmatrix}, \mathbf{R}_{X_3} = \mathbf{R}_{X_4} = \begin{bmatrix} 1 & 0 & 0 \\ 0 & \cos\theta_2 & -\sin\theta_2 \\ 0 & \sin\theta_2 & \cos\theta_2 \end{bmatrix} \tag{A.5}$$

  where $\theta_1 = -\pi$, $\theta_2 = -\pi/2$. The overall rotation matrices $\mathbf{R}_3$ and $\mathbf{R}_4$ are defined as:

$$\mathbf{R}_3 = \mathbf{R}_{Y_3}\mathbf{R}_{X_3}, \quad \mathbf{R}_4 = \mathbf{R}_{Y_4}\mathbf{R}_{X_4} \tag{A.6}$$

- The rotation matrices $\mathbf{R}_5$ and $\mathbf{R}_6$ of SBA 5 and SBA 6 are obtained through rotations about the Y_5, X_5 and Y_6, X_6 axes, respectively, of the same form as $\mathbf{R}_3$ and $\mathbf{R}_4$, with $\theta_1 = -\pi/2$, $\theta_2 = -\pi/2$.

Appendix B

Microfabrication Recipes

All microfabrication recipes cited in Chap. 4 are listed below:

Table B.1 Spinning a 1.4-μm layer of Shipley-1813 photoresist on a four-inch silicon wafer

tool: Site Services Coater/Developer (SSCD)	recipe: 4C14NEBR.LN
step	parameters
spin	200 rpm
dispense resist from edge to center	
accelerate	50000 rpm/s
spin	3950 rpm, during 30 s
spin	2000 rpm
decelerate	10000 rpm/s
softbake	115°C, during 1 min

Table B.2 Exposing a layer of photoresist on a four-inch silicon wafer using top-side alignment marks

tool: EVG 620 Aligner	recipe: TopSide-5inMask-4in.rcp
parameter	value
maskholder size	5 inches
substrate size	4 inches
separation	50 μm
mask thickness	2.28 mm
substrate thickness	300 μm
resist thickness	1.4-μm layer of Shipley-1813 10-μm layer of AZ9245
process	top side
process mode	transparent
exposure mode	constant energy
contact mode	hard contact
energy	65 mJ (1.4-μm layer of Shipley-1813) 250 mJ/cycle cycles (10-μm layer of AZ9245)

Table B.3 Developing a 1.4-μm layer of Shipley-1813 photoresist on a four-inch silicon wafer

tool:Site Services Coater/Developer (SSCD)	
recipe: D1813_45.LN	
step	parameters
accelerate	10000 rpm/s
spin	400 rpm, during 2.5 s
	after 1 s, dispense developer from edge to center
decelerate	10000 rpm/s
spin	50 rpm, during 2.5 s
decelerate	10000 rpm/s
	stand still for 41 s
	dispense DI water in the center for 20 s
spin	500 rpm, during 20 s
spin	3000 rpm, during 10 s
decelerate	10000 rpm/s
spin	100 rpm, during 5 s
decelerate	500 rpm/s
hardbake	90°C, during 90 s

Table B.4 Regular solvent clean process on solvent bench

tool: solvent bench	
step	parameter
acetone dip	15 min at room temperature
isopropyl alcohol dip	15 min at room temperature
distilled water	10 min at room temperature
wafer drying using nitrogen gun	

Table B.5 Deep reactive ion etching of silicon

tool: Tegal SDE110 DRIE						recipe: SPC BOSH 2UM S1813	
depth: 4 μm						duration: 1 min 30 s	
step							
		main etch					
THERM 0C 200MM	TEMP 30 SEC 200 MM	gas	time (s)	flow (sccm)	pressure (mbar)	RF power source (w)	LF power frequency(Hz)
		SF_6	2.0	300	4.5^{-2}	2000	285
		C_4F_8	4.5	150	2.5^{-2}	2000	280

Table B.6 Growing a 5000-Å layer of silicon dioxide on silicon

tool: Tylan Oxidation and LPCVD Furnace Stack	
parameter	value
gas	$O_2 + H_2$ (wet environment)
temperature	1100°C
duration	38 min 49 s

Table B.7 Reactive ion etching of silicon dioxide

tool: Applied Materials P5000 RIE		recipe: NANOTOOL OX ETCH	
depth: 0.55 μm			
step	stabilization	main etch	rampdown
time (s)	15	120	30
pressure (mTorr)	100	100	open
power (w)	0	720	100
B-field (Gauss)	0	70	0
CHF_3 (sccm)	45	45	0
Ar (sccm)	70	70	100
CF_4-1 (sccm)	7	7	0

Table B.8 Lift-off process

tool: Solvent Wetbench	
step	time
—c—soak the wafer into Remover PG at 70°C with the ultrasonic bath	40 min
rinse the wafer by means of DI water	10 min

Table B.9 Deep reactive ion etching of silicon

tool: Tegal SDE110 DRIE				recipe: McGill TSV 820HM			
depth: 300 μm				duration: 18 min			
step							
THERM -5C 150MM	TEMP 30 SEC 150 MM	TSV (main etch)					
		gas	time (s)	flow (sccm)	pressure (mbar)	RF power source (w)	LF power frequency(Hz)
		SF_6	2	500	7.0^{-2}	2800	285
		C_4F_8	1	300	7.0^{-2}	2800	285
		O_2	8	200	1.8^{-1}	2800	273